In compliance with the
Canadian Privacy Legislation
some supporting forms
may have been removed from
this dissertation.

While these forms may be included
in the document page count,
their removal does not represent
any loss of content from the dissertation.

Dark Matter Detection and Structure Formation

by

David Stiff

A thesis submitted to the Department of Physics
in conformity with the requirements
for the degree of Doctor of Philosophy

Queen's University
Kingston, Ontario, Canada
September, 2003

Copyright © David Stiff, 2003

National Library
of Canada

Acquisitions and
Bibliographic Services

395 Wellington Street
Ottawa ON K1A 0N4
Canada

Bibliothèque nationale
du Canada

Acquisisitons et
services bibliographiques

395, rue Wellington
Ottawa ON K1A 0N4
Canada

Your file Votre référence
ISBN: 0-612-86244-5
Our file Notre référence
ISBN: 0-612-86244-5

The author has granted a non-exclusive licence allowing the National Library of Canada to reproduce, loan, distribute or sell copies of this thesis in microform, paper or electronic formats.

The author retains ownership of the copyright in this thesis. Neither the thesis nor substantial extracts from it may be printed or otherwise reproduced without the author's permission.

L'auteur a accordé une licence non exclusive permettant à la Bibliothèque nationale du Canada de reproduire, prêter, distribuer ou vendre des copies de cette thèse sous la forme de microfiche/film, de reproduction sur papier ou sur format électronique.

L'auteur conserve la propriété du droit d'auteur qui protège cette thèse. Ni la thèse ni des extraits substantiels de celle-ci ne doivent être imprimés ou aturement reproduits sans son autorisation.

Canada

ABSTRACT

According to current cosmological models, the majority of the matter in the universe is not visible. Only a small fraction of the total matter consists of visible baryonic material, the remainder is *dark matter*. A promising candidate for dark matter is an exotic particle left over from the early Universe. While there are numerous theoretical models supporting this view, there has never been a definitive detection of any such particle. Nonetheless, there are currently over 20 terrestrial-based detection experiments in operation or under construction around the world searching for dark matter of this type. The majority of these experiments are designed, and their analysis is based, upon the simple assumption that dark matter will be smoothly distributed throughout the Milky Way, and in particular, in the solar neighbourhood. However, this assumption has not been rigorously tested, and if incorrect, could lead to inefficient detector design, and even improper analysis of the data.

Two techniques are developed to investigate the distribution of dark matter in the solar neighbourhood. The first involves combining N-body simulations with analytic models to build a high-resolution picture of the dark matter distribution. The second technique takes advantage of the reversibility of collisionless systems to obtain a very high-resolution picture of the dark matter distribution in the vicinity of the Earth. This new "reverse-run" method improves the velocity resolution at a particular point in the simulation by many orders of magnitude. In both the semi-analytic models, and the reverse-run technique, it is found that the dark matter distribution is not smooth. Applying the reverse-run technique to a simulation of the formation of the Milky Way and M31 indicates that the velocity-space distribution of dark matter close to the solar neighbourhood has a wealth of substructure.

The effects of this substructure on dark matter detection experiments is significant. In particular, it can shift the energy and direction of the highest detection rates from what would be expected due to a smooth halo. It is also shown that the seasonal variation of the detection spectra can introduce characteristic signatures of velocity-space substructure.

The traditional smooth halo assumption does not withstand careful analysis. The dark matter distribution is found to have a considerable amount of structure which would have a significant impact on terrestrial dark matter detection experiment. This substructure must be taken into account when designing and analysing dark matter detection experiments.

STATEMENT OF CO-AUTHORSHIP

This study was performed under the supervision of Dr. L. Widrow at Queen's University. Chapter 4 is based upon a paper written in conjunction with L. Widrow and J. Frieman (Stiff et al., 2001). Chapter 5 is an extension of a paper with L. Widrow (Stiff and Widrow, 2003). Chapters 6 and 7 are the basis for a paper with L. Widrow (in preparation).

All of the work described herein was done by the author (D. Stiff) except where explicitly stated otherwise.

ACKNOWLEDGEMENTS

I first must thank my supervisor, L. Widrow, for his advice and support throughout the long process of completing this thesis. Without his guidance, none of this would have been possible.

Thanks also must go out to all the astronomy graduate students (past and present), and others in the Physics Department, who made my time here so enjoyable. A special thanks to those who let me ramble on about my research problems and successes.

I also must acknowledge NSERC (1998, 1999, 2001, 2002), the Ontario Government through OGS (2000), Queen's University and the Department of Physics for funding this research.

Finally, I would like to thank my family for supporting me throughout my time at Queen's.

CONTENTS

LIST OF FIGURES

LIST OF TABLES

1. INTRODUCTION

1.1 Dark Matter

Over the last several decades a growing body of evidence has indicated that we understand the properties of only a small fraction of the total matter in the universe. The first piece of the puzzle was found by Zwicky (1933) when he noticed that the velocity dispersion in the Coma cluster of galaxies was much higher than could be explained by the visible mass present. He concluded that a significant portion of the mass in the cluster must be in some form which is not visible to observers. Over the years, many more observations have confirmed the result that a large fraction of the matter in the universe is non-luminous (see for example, Bergstroem (2000)). A classic indicator of the presence of dark matter is the rotation curve of spiral galaxies. If all the matter is luminous, one would expect the rotational velocities of gas and stars to fall like $r^{-1/2}$ outside the visible regions. However, the observed rotation speed (symbols in Figure 1.1) is roughly constant out as far as observations can be obtained. Estimates from the velocity dispersion of clusters and rotation curves indicate that as much as 90% of the total matter in the galaxies and clusters must be "dark".

Observations of the Cosmic Microwave Background (CMB) provide an independent means to determine the dark matter component of the universe. These measurements are based on the calculation of the growth of perturbations in the early epoch of the universe. For a review, see White et al. (1994). The most recent results indicate that the universe consists of approximately 5% normal (baryonic) matter ($\Omega_b \sim 0.05$), and 25% dark matter ($\Omega_{dm} \sim 0.25$). The remaining 70% of the

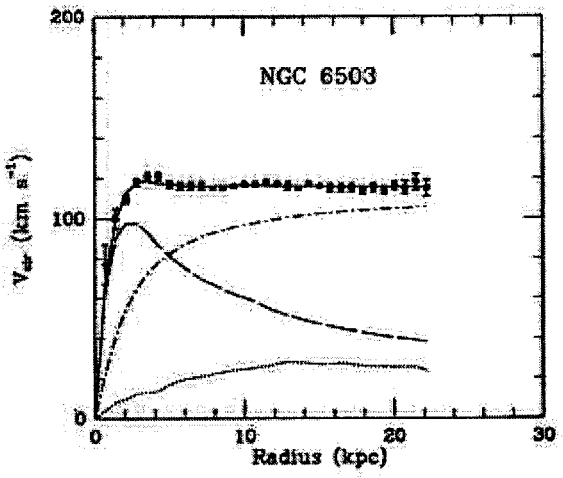

Figure 1.1: Rotation curve of NGC 6503 from Begeman et al. (1991). The dashed and dotted lines are the rotation due to the mass of the visible stars and gas respectively. The dash-dot curve is the contribution that must be due to dark matter to agree with the observed rotation (symbols).

mass is even more mysterious than the dark matter and is thought to be in the form of a cosmological constant or dark energy ($\Omega_\Lambda \sim 0.70$)(Spergel et al., 2003; Lange et al., 2001; Stompor et al., 2001). (A review the parameters and definitions used when discussing cosmology and cosmological models can be found in Appendix A.)

While there are numerous theoretical candidates for dark matter, none has yet been definitively detected. Nonetheless, there are currently over 20 detectors around the world that are in operation or under development, all on a quest to identify the nature of the dark matter component of the universe. While progress in detector design and sensitivity has improved greatly over the past several years, detailed predictions have yet to be made regarding what these detectors expect to see. The vast majority of all theoretical predictions have made the simple assumption that the Milky Way's dark-matter halo has a smooth, almost featureless distribution. The validity of this assumption has never been rigorously tested. In order for these detectors to be designed optimally and to correctly interpret any results, it is nec-

essary to develop an accurate model of the distribution of dark matter in the solar neighbourhood. Such predictions require a detailed understanding of the mechanisms involved in the formation of structure in the universe as well as knowledge of the nature of dark matter and detection techniques.

The remainder of this Chapter introduces the basic dark matter candidates, detection techniques and the effects of dark matter on structure formation. Chapter 2 covers the numerical techniques that will be used in the subsequent chapters to investigate the dark matter distribution in the solar neighbourhood. The integrity and stability of phase-space structures in numerical simulations, of crucial importance for terrestrial detection experiments, will be investigated in Chapter 3. Chapter 4 introduces semi-analytic techniques that can be used to study the dark matter distribution around the Earth, and draws some preliminary conclusions about the nature of the distribution. To further probe the phase-space distribution of dark matter, a novel "reverse-run" method is introduced and tested in Chapter 5, and is applied to a realistic simulation of the Milky Way in Chapter 6. The results from Chapters 4, 5, and 6 are applied to a detailed study of detection experiments in Chapter 7. Finally, a summary of the work completed and the primary conclusions are presented in Chapter 8. Appendices A and B provide some technical background and derivations for cosmological models and linear theory of structure formation respectively.

1.2 Structure Formation in the Universe

While it is believed that the universe is homogeneous and isotropic on large scales, observations show that this in not the case on small scales. Galaxies appear to be preferentially collected into groups and clusters. On larger scales, these groups and clusters then appear to be associated into supergroups and superclusters. It is currently unknown how far this hierarchy extends.

The formation of this hierarchy is seeded by small density fluctuations in the

early universe which arise due to random quantum perturbations. However, the spectrum of the density perturbations itself is not sufficient to predict how structure in the universe forms. The nature of the dark matter itself also directly affects how the cosmological hierarchy forms. If, in the early universe, the dark matter particles are relativistic, structure forms from the "top down". Large objects form first and then fragment into smaller pieces (Primack and Gross, 2001). For example, a cluster-size object would fragment and form individual galaxies. This top-down formation occurs because the relativistic dark matter can easily escape from any small gravitational potential well which then reduces the depth of the well. This prevents any small overdense region from collapsing. Only overdensities that are large compared to the mean free path of the dark matter particles can undergo gravitational collapse. Since these particles are dynamically hot in the early universe, this type of dark matter is called *hot dark matter* (HDM).

In contrast, if the dark matter is non-relativistic, structure will form from the "bottom up" (Peebles, 1982). Galaxies form before clusters, with smaller objects merging into larger entities. In the early universe, these particles have small velocities and can be gravitationally captured in small density perturbations causing these regions to collapse on relatively short time-scales. The mass in these small regions becomes gravitationally bound and later merges into larger clumps. Dark matter particles which are non-relativistic in the early universe are called *cold dark matter* (CDM).

1.3 Dark Matter Candidates

In order to study the signal that would be observed in Earth-based detectors, it is necessary to investigate what the dark matter could be. While the dynamical and CMB evidence indicates that dark matter exists and plays an important role in the universe, it can tell us very little about the exact nature of the dark matter. Since its initial introduction there have been many proposed dark-matter candidates. These

range from the rather mundane such as cold gas (Pfenniger et al., 1994) to the more exotic such as microscopic black holes (Ivanov et al., 1994). However, the leading candidates are particles which arise from extensions to the Standard Model of particle physics.

1.3.1 Massive Neutrinos

One early dark matter candidate was a massive neutrino. The original neutrino was proposed by Pauli in 1931, and was first detected by Reines and Cowan (1953). While the neutrino was originally thought to be massless, there is a growing body of evidence that indicates that it does have a mass (Groom et al., 2000). In particular, the difference between the measured flux of solar neutrinos and the flux predicted from solar models requires that the neutrino has a non-zero mass (Groom et al., 2000). Recent measurements from the Sudbury Neutrino Observatory, taken in conjunction with Super-Kamiokande results (Toshito and The Super-Kamiokande Collaboration, 2001), and tritium beta decay experiments (Bonn et al., 2001) indicate that the total mass of all three neutrino flavours (electron neutrinos, muon neutrinos, and tau neutrinos) is constrained to 0.05 eV $< \sum_i m_{\nu_i} <$ 8.4 eV (Ahmad and et al., 2001).

Two problems arise when the attempt is made to solve the dark-matter problem with neutrinos. First, recent constraints on the upper mass limit of the neutrino coupled with production rate estimates in the early universe place an upper bound on the total mass in the form of neutrinos. This contribution is significantly below the mass required to account for all of the dark matter. With the mass restrictions from above, the cosmological neutrino density is restricted to $0.0001 < \Omega_\nu < 0.18$ (Ahmad and et al., 2001), with the lower end of the range being favoured.

The second problem is that since neutrinos are so light, they would be a form of hot dark matter. A comparison of numerical simulations of HDM models with observation indicates that top-down formation does not yield structures similar to

those that are observed in the universe today (Primack and Gross, 2001). This distribution of sizes and ages of galaxies formed in HDM models differ significantly from observations. Any dark matter candidates must be dynamically cold in the early universe.

1.3.2 Weakly Interacting Massive Particles

A broad class of dark matter particles is a Weakly Interacting Massive Particle (WIMP). Since WIMPs are (by definition) massive, they would be non-relativistic in the early universe and a form of CDM. Therefore, WIMPs could provide consistency between numerical simulations and observations.

The most likely WIMP candidates arise from supersymmetric extensions to the Standard Model (Groom et al., 2000). Supersymmetric models introduce an additional property, R parity, which can have values of only ± 1, to particles in the Standard Model. This symmetry adds a partner for every particle in the Standard Model which has equal charge but differs in spin by 1/2. This spin difference in supersymmetric models unites the fermionic and bosonic components of the Standard Model.

The additional R parity is important with regard to the stability of supersymmetric particles. The traditional Standard Model particles have $R = +1$ while their supersymmetric partners have $R = -1$. For example, an electron has $R = 1$ and its supersymmetric partner, a selectron, would have $R = -1$. R parity is multiplicative and must be conserved when a particle decays. A Standard Model particle could then decay into any number of other Standard Model particles, but must decay into an even number of (or zero) supersymmetric particles. On the other hand, if a supersymmetric particle decays, there must be at least one supersymmetric particle left to maintain $R = -1$. Therefore, supersymmetric particles cannot completely decay away into traditional Standard Model particles. Instead there could be an accumulation of the lightest supersymmetric particle (LSP) which could no longer

decay. Such a particle has not been definitively observed in either particle accelerator experiments, or in cosmological searches, so the mass of the LSP must be much larger than the mass of currently known particles. While these masses are above the production capabilities of current particle accelerators, they would have been produced in abundance in the early universe.

The lightest supersymmetric particle in many models is the neutralino, χ. This neutral massive particle would interact only very weakly with normal matter. Current experimental limits require that $m_\chi \gtrsim 35$ GeV (Groom et al., 2000). While supersymmetric models can explain some of the weaknesses of the Standard Model, there is currently no compelling evidence to support them.

1.3.3 Axions

One of the problems with the Standard Model is the lack of charge-parity (CP) violation in strong interactions (Groom et al., 2000). The strong force Lagrangian contains a free dimensionless parameter, θ, which determines if CP violation occurs or not. If $\theta \neq 0$, the Lagrangian violates CP conservation. If $\theta = 0$, it does not.

While the Standard Model provides no reason to expect that $\theta = 0$, experimental measurements of the neutron electric dipole moment indicate that $\theta \leq 2 \times 10^{-9}$. The question of why θ is so small is known as the *Strong CP Problem.*

In order to avoid the fine-tuning of θ, Peccei and Quinn (1977) proposed an additional symmetry (PQ symmetry) to the Standard Model. When this new symmetry is broken it forces $\theta = 0$. Unfortunately, the introduction of such as symmetry also introduces a new particle – the axion. The axion couples most strongly with photons yielding two possible interactions. The first is when axions spontaneously decay into two photons,

$$a \rightarrow \gamma + \gamma \tag{1.1}$$

The second process is the conversion of axions to photons through Primakoff processes (Sikivie, 1983) where an axion couples with a strong magnetic field and is

converted into a photon. There is also an equal chance that a photon could be converted to an axion.

$$a \leftrightarrow \gamma \tag{1.2}$$

The likelihood of these processes occurring is proportional to both the strength of the electric and magnetic fields and their relative alignment in the region of interest.

Current axion models do not provide any stringent constraints on the mass of the particles. However, some constraints can be obtained for the mass of the axion from some unexpected sources. An upper limit can be derived from stellar models (Groom et al., 2000). Current models of stellar evolution successfully describe the evolution of stars over almost their entire life. These models do not include any Primakoff production of axions in the stellar cores. Therefore, if axions exist, they must have a sufficiently small effect as to not significantly alter the evolution of stars. If axions are too massive they would carry a large amount of energy out of the stellar interior and thus alter the star's evolution. Such considerations place an upper limit on the mass of the axion of

$$m_a < 10^{-2}\,\mathrm{eV} \tag{1.3}$$

A lower limit on the axion mass can be obtained from cosmological considerations. If the energy scale of PQ symmetry breaking is less than 10^8 GeV, axions would have a sufficiently short lifetime that their decay should be observable. Such decays would manifest themselves as monochromatic lines in the spectra of distant galaxies. This has not been observed (Bershady et al., 1991). Therefore, it is likely that the PQ energy scale is greater than 10^8 GeV. At such energies, the mechanisms for axion formation would produce *non-thermal* axions — the axions would be dynamically cold. In this situation, the cosmological axion density, Ω_a, is inversely proportional to the axion mass (Turner, 1986, for example):

$$\Omega_a \propto m_a^{-1.175} \tag{1.4}$$

where the proportionality constant is dependent upon the details of the cosmological model. Consideration of the total mass density of dark matter in the universe limits the axion mass to be

$$m_a > 10^{-6}\text{eV} \tag{1.5}$$

1.3.4 Massive Compact Halo Objects

A different type of dark matter candidate is a Massive Compact Halo Object (MACHO). Unlike WIMPs or axions, MACHOs consist of standard baryonic matter, but are simply too small or dark to be easily observed from the Earth. MACHOs include a wide variety of small, but possibly very massive, objects including brown dwarf stars (stars which are not massive enough to support fusion within their core) and small black holes. There are several observational searches for MACHO signatures (Afonso et al., 2003; Alves et al., 2002; Wozniak, 2000; Alcock et al., 2000) and all indicate that MACHOs cannot account for a significant portion of the dark matter.

1.4 Detecting Dark Matter

While observations of the dynamical behaviour of galaxies and clusters indicate that dark matter must exist, they cannot distinguish between the various CDM candidates. In order to determine what the dark matter is, it must be detected directly on Earth. This could be done through high-energy accelerator experiments which aim to detect signs of dark matter candidates, or through efforts to detect any dark matter still present from the early universe. The efforts to detect WIMPs have primarily focused on bolometric and scintillation detectors. However, since the mass of axions is much smaller than WIMPs, different techniques, such as detectors based upon Primakoff conversion, must be used.

1.4.1 Bolometric Detectors

Bolometric detectors attempt to measure the energy deposited when a WIMP interacts with a nucleus in the detector. If a WIMP of mass m_χ scatters elastically with a nucleus of mass m_N, the nucleus recoils with an energy of

$$Q = \left(\frac{m_r^2 v^2}{m_N}\right)(1 - \cos\theta^*) \tag{1.6}$$

where $m_r \equiv m_N m_\chi / (m_N + m_\chi)$ is the reduced mass, v is the speed of the WIMP relative to the nucleon, and θ^* is the scattering angle in the centre-of-mass frame (Jungman et al., 1996). Note here and throughout, the speed of light, c, is set to 1. Only a fraction, q, of this recoil energy is observed in the detector. However, since the value of q is a function of detector design, it is more convenient to discuss detection rates in terms of the recoil energy rather than the quenched values. The differential detection rate per unit detector mass can then be written

$$\frac{dR}{dQ} = \frac{\sigma_0 \rho_L}{2 m_r^2 m_\chi} F^2(Q) \int_{v_{\min}}^{\infty} f_1(v) \frac{dv}{v} \tag{1.7}$$

where σ_0 is the scattering cross-section, ρ_L is the local WIMP density, $F(Q)$ is a form factor for the WIMP-nucleon interaction, and $v_{\min} = (Q m_N / 2 m_r^2)^{1/2}$ (e.g., Jungman et al. (1996)). Here $f_1(v)$ is the normalized distribution of WIMP speeds in the rest frame of the detector, obtained by integrating the three-dimensional velocity distribution $f(\mathbf{v})$ over all angles. In general, $F(Q)$ depends upon the coupling between the WIMP and nucleus but for simplicity $F(Q) = 1$ will be assumed here.

Many detectors, such as the Cold Dark Matter Search (CDMS) (Gaitskell, 2001) use germanium targets. Therefore, unless otherwise stated, calculations involving bolometric detectors will assume that the detector is germanium with a nucleon mass of $m_N = 68.5$ GeV.

1.4.2 Directional Sensitive Detectors

One disadvantage of bolometric detectors is that they cannot determine any information about the direction of the incoming WIMP. Directional sensitivity would

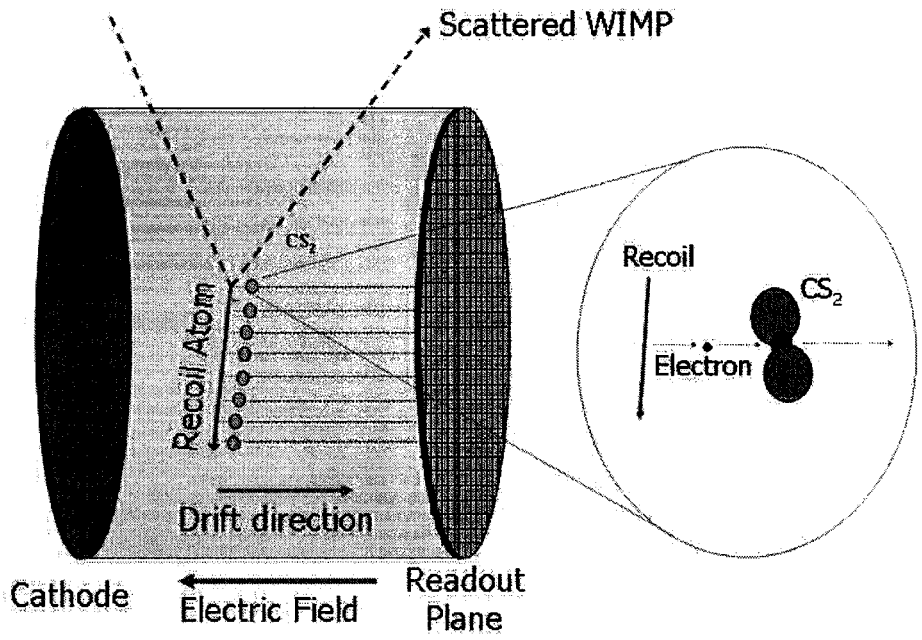

Figure 1.2: Schematic of the DRIFT detector. (From the DRIFT website at http://www.shef.ac.uk/uni/academic/N-Q/phys/research/pa/DRIFT.html)

greatly improve the usefulness of dark matter detectors. Directional correlations could be used to reduce background signals and yield information about the full three-dimensional velocity distribution of dark matter rather than simply the speeds.

The basic idea behind directional WIMP detectors is to track the recoil path of a nucleus after a scattering event. Generally, this involves following the ionization path of the scattered nucleus. For example, in the Directional Recoil Identification From Tracks (DRIFT) experiment (Martoff et al., 1999), a low pressure carbon disulphide gas chamber is used to determine the trajectory of the recoil. Figure 1.2 shows a schematic of the operation of the DRIFT detector. As the recoiled nucleus travels through the gas, it ionizes surrounding material. The free electrons are captured by the carbon disulphide (since it is electronegative) creating negatively charged ions. These ions drift under the influence of an electric field to the detection array at one end of the chamber. From the observed recoil path, the direction of

the incoming WIMP can be constrained, but not uniquely determined due to the random scattering angle. In addition, as the ions drift towards the detection array, they will diffuse, resulting in an imperfect measure of the recoil path. However, one major advantage of the DRIFT experiment is that the size and shape of the detected paths can be also used to discriminate true WIMP recoils from background events. This results in a very high signal to noise ratio. Robust conclusions can be drawn from only hundreds of WIMP detections. Currently DRIFT is in its first stages of operation in the Boulby Mine in the U.K.

1.4.3 Axion Detectors

The techniques for detecting axions are very different from those for WIMPs. Since the energy of an individual axion is very small, bolometric techniques would be inappropriate. Instead, the primary technique for axion detectors is to use Primakoff conversion to transform axions into detectable photons. The energy of the detected photons corresponds to the total energy (rest mass plus kinetic) of the axions.

Several such detectors are in operation or under development including the MIT-Livermore axion search (Daw, 2001) and PVLAS (Cantatore et al., 2001). Several other detectors are also looking for axions produced in the core of the Sun. These axions would be highly collimated as they pass though Earth-based detectors and provide an excellent target for study though it should be noted that they would be significantly more energetic than cosmological axions. Detectors looking for solar axions include the SOLAX Collaboration (Avignone et al., 1999) and CAST (Zioutas et al., 1999).

1.5 Dark Matter Detection Spectra

The experimental spectrum of energies that any dark matter experiment may detect will naturally depend upon the true distribution of energies. However, in order to design efficient and useful detectors, one must make assumptions about this true

distribution. Additionally, the interpretation of any experimental signatures will depend upon any assumptions made of the true dark matter distribution.

1.5.1 Smooth Dark Matter Distributions

While the observable universe is homogeneous on very large scales ($\gtrsim$ 100 Mpc), it is very clumpy on galactic scales. However, if the Milky Way has evolved very quiescently in its recent history, it is possible that the dark matter distribution has been thoroughly virialized and is quite smooth. It is then convenient to assume that the dark matter has a Maxwellian velocity distribution (Jungman et al., 1996, and references therein):

$$f(\mathbf{v}_{DG})d^3v_{DG} = \frac{1}{\pi^{3/2}v_o^3}e^{-v_{DG}^2/v_o^2}d^3v_{DG} \tag{1.8}$$

where $\mathbf{v}_{DG}$ is the dark matter velocity relative to the Galaxy, and $v_o \sim 220$ km s^{-1} is the two-dimensional halo velocity dispersion. (Some authors (Jungman et al., 1996, for example) apply a cut-off at the local escape speed; however, it has a negligible effect (Freese et al., 1988).) The Sun is orbiting the centre of the Galaxy at roughly 230 km s^{-1} and the velocity of interest is that of the Earth-based detector relative to the dark matter distribution. A transformation to the frame of the Earth is simply $\mathbf{v}_{DE} = \mathbf{v}_{DG} + \mathbf{v}_{GE}$ where the subscripts denote the dark matter (D), the Galaxy (G), and the Earth (E). Therefore, the correct velocity distribution to consider is

$$f(\mathbf{v}_{DE})d^3v_{DE} = \frac{1}{\pi^{3/2}v_o^3}e^{-|\mathbf{v}_{DE}+\mathbf{v}_{EG}|^2/v_o^2}d^3v_{DE} \tag{1.9}$$

where $\mathbf{v}_{EG}$ is the velocity of the Earth relative to the Galaxy. Integrating over all directions yields the speed distribution (Freese et al., 1988):

$$f_1(v_{DE}) = \frac{v_{DE}}{v_{EG}v_o\sqrt{\pi}}\left(\exp\left[-\frac{(v_{DE}-v_{EG})^2}{v_o^2}\right] - \exp\left[-\frac{(v_{DE}+v_{EG})^2}{v_o^2}\right]\right) \tag{1.10}$$

Under such assumptions it is straightforward to analytically calculate the expected detection spectra for the various dark matter candidates.

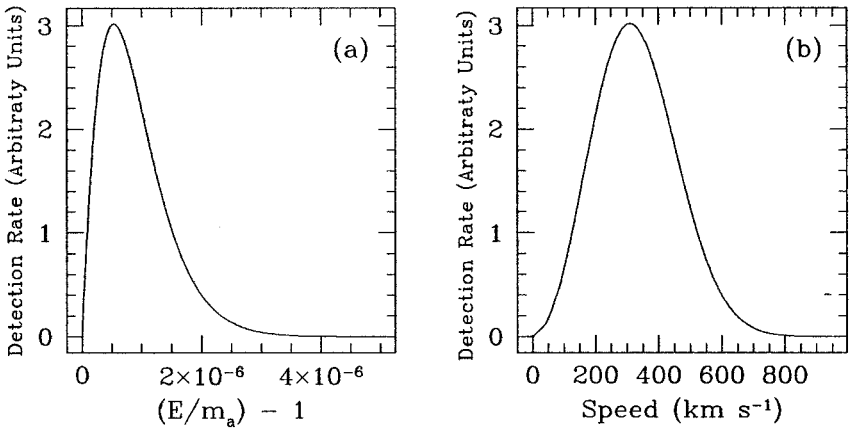

Figure 1.3: Axion detection rate for a Maxwellian velocity distribution in terms of a) energy, where m_a is the rest mass of the axion, and b) speed.

For axions, detectors are sensitive to the photons that correspond to the total energy of the axion. The total energy is simply the rest mass of the axion, m_a, plus its kinetic energy. Therefore, the energy spectra detected for axions are directly related to the speed distribution with a lower cutoff at the axion mass. For example, Figure 1.3 shows an ideal axion spectrum in terms of its energy and speed. Notice the very narrow energy range over which axions would be detected $E/m_a - 1 < 4 \times 10^{-6}$. This requires that axion detectors have very high energy resolution.

The modelling of WIMP detection events is considerably more involved than for axions. In particular, in bolometric detectors the amount of energy deposited depends upon a random scattering angle. If a certain amount of energy is detected it could have come from a WIMP with only slightly more energy and almost total energy transfer ($\theta^* \sim \pi$) or it could have come from a WIMP with considerably more energy where only a small amount of the energy is transferred ($\theta^* \sim 0$). Therefore, the expected detection rates involve an integral over all scattering angles. Figure 1.4 shows an ideal WIMP detection rate spectrum in terms of the energy detected. Note how the peaked speed distribution is observed as a monotonically decreasing spectrum in the energy detection rates. A WIMP mass of 50 GeV and detector

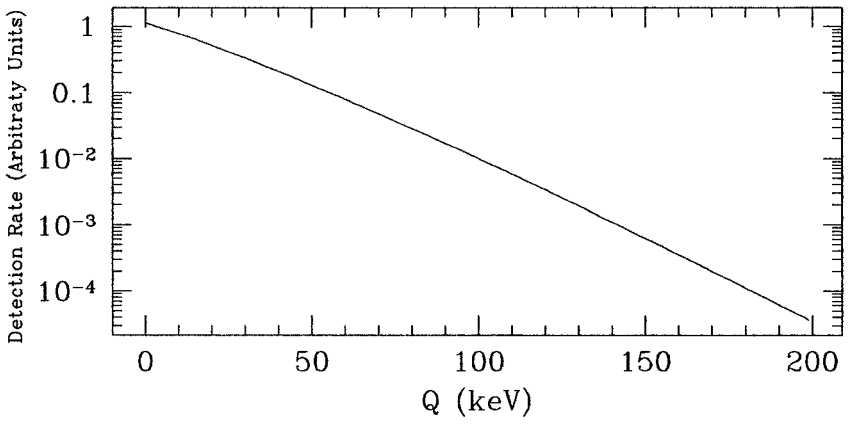

Figure 1.4: WIMP detection rate for a Maxwellian velocity distribution in terms of the recoil energy. A WIMP mass of 50 GeV and a detector nucleon mass of 68.5 GeV are assumed.

nucleon mass of 68.5 GeV are assumed.

1.5.2 Non-Uniform Dark Matter Distributions

The Sagittarius dwarf galaxy provides compelling evidence that the Milky Way is still undergoing merger and accretion events (Ibata et al., 1995). Therefore, it is unlikely that the dark-matter halo is completely virialized and hence smooth. Furthermore, recent high resolution numerical simulations tend to indicate an ever-increasing amount of substructure at progressively smaller scales (see for example Moore et al., 2001). The assumption of a smooth dark matter halo for modelling dark matter detection events must now be questioned.

To see the effects of non-uniform dark matter distributions on detection experiments, consider the admittedly contrived situation where the local dark matter consists of n streams each with a density of ρ_L/n, where ρ_L is the mean density of dark matter in the solar (local) neighbourhood. The average density would be the same as for a smooth halo but the velocity distribution would be significantly different. This complex velocity distribution could give rise to very different detec-

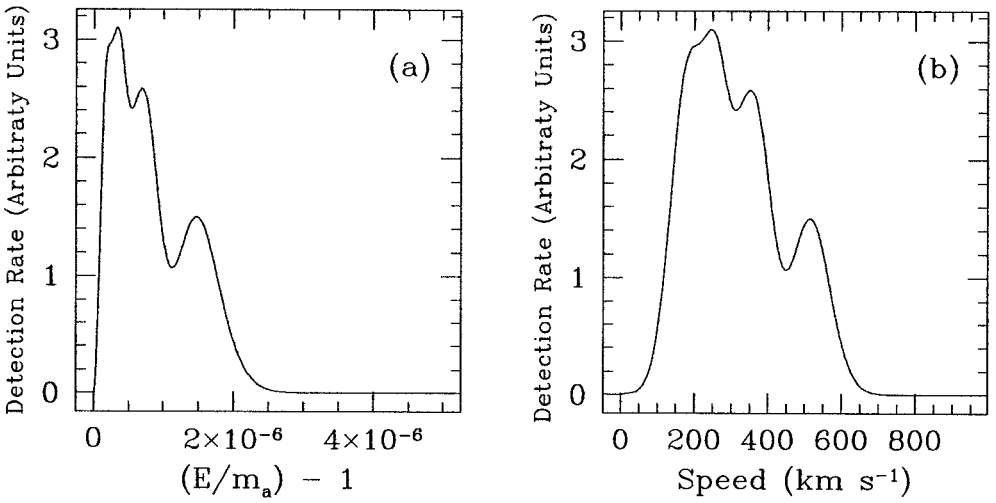

Figure 1.5: Axion detection rate for a velocity distribution consisting of 10 randomly oriented streams of dark matter in terms of a) energy where m_a is the rest mass of the axion, and b) speed. Note the significant features in the spectra due to the non-uniformity of the dark matter distribution.

tion spectra. Figures 1.5 and 1.6 show the ideal axion and WIMP spectra if the local dark matter distribution consisted of $n = 10$ identical streams with random orientations. The spectra are significantly different than those from a Maxwellian distribution. Note that this distribution is simply designed to be illustrative and does not necessarily have any physical motivation. However, this difference between the uniform and non-uniform dark matter distributions presents an enormous challenge for dark matter detector design and analysis. In order to correctly interpret results and optimize detector design and operation, an accurate picture of the dark matter distribution in the solar neighbourhood is required.

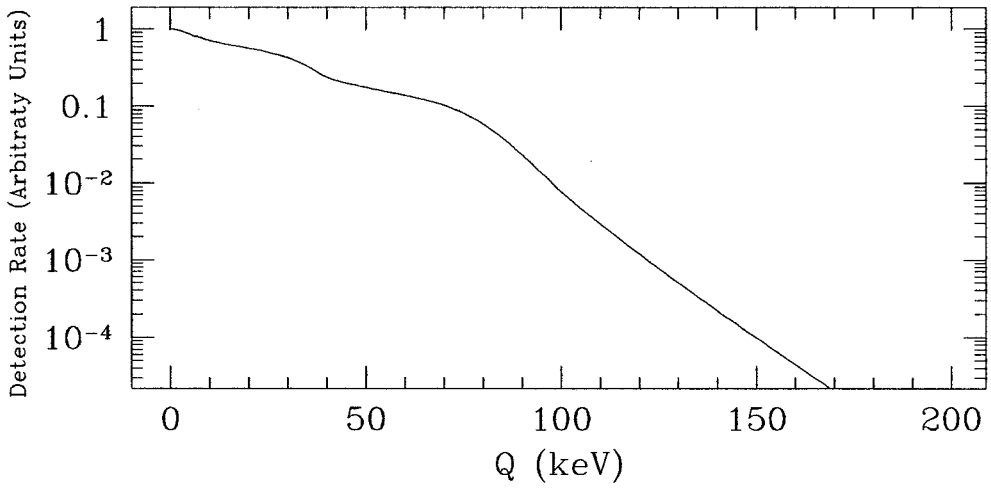

Figure 1.6: WIMP detection rate for a 10-stream velocity distribution in terms of the recoil energy, Q. Though still quite smooth overall, the non-uniform WIMP distribution significantly alters the slope of the spectrum in both the low and high energy regimes. A WIMP mass of 50 GeV and a detector nucleon mass of 68.5 GeV are assumed.

1.6 Determining the Local Phase-Space Distribution of Dark Matter

With so many dark matter detection experiments in progress or development, it is necessary to test the assumption upon which many are based: that the dark matter in the solar neighbourhood is smoothly distributed. As illustrated in the previous section, a non-Maxwellian distribution can significantly alter the observed spectra. In order to make accurate predictions, one needs to have an accurate knowledge of the local phase-space distribution of dark matter.

The most straightforward approach is to simply use a numerical simulation which resembles the formation of the Milky Way and environs and look at the distribution of particles in the solar neighbourhood. Unfortunately, the resolution required to obtain accurate statistics is well beyond the computational limits imposed by today's technology. For example, consider a simulation with N particles in a cube with sides of length L. If one is interested in the velocity-space structure at a point which has a density of δ times the mean density, the number of particles in a cube with sides αL is approximately $n = \alpha^3 \delta N$. Using typical numbers of a large present-day simulation, $N = 10^9$, $L = 1$ Mpc, $\alpha L = 1$ kpc, and $\delta = 1000$, one obtains $n = 1000$. This number of particles is not sufficient to accurately map out the velocity space at that point, especially if there is significant structure in velocity space. A larger value of α could be chosen, but this could blur the velocity-space distribution by averaging over too large an area. To obtain the equivalent resolution in phase-space (or *local* velocity-space) to that of configuration-space requires an increase in N of many orders of magnitude. Such a simulation is well beyond the bounds of current simulations simply due to the excessive computational resources that would be required. Therefore, alternative techniques must be applied to investigate the phase-space distribution of dark matter in the solar neighbourhood.

2. NUMERICAL TECHNIQUES

In order to determine the expected density of dark matter in the solar neighbourhood, it is necessary to use numerical techniques. Analytic models describing the evolution of dark matter can only deal with broad, general characteristics of the distribution. For example, in cosmological spherical collapse models the average density, ρ, inside a sphere at maximum expansion compared to the average background density of the universe, ρ_{bg}, can easily be determined (Peebles, 1982). Consider a spherical density perturbation that has a mass M, and radius r. It would evolve according to

$$\ddot{r} = -\frac{GM}{r^2} \tag{2.1}$$

The solution for $r(t)$ can be expressed parametrically:

$$r = A(1 - \cos\theta) \tag{2.2}$$

$$t = B(\theta - \sin\theta) \tag{2.3}$$

with the constraint that $A^3 = GMB^2$. At maximum expansion, $\theta = \pi$, $r = 2A$ and $t = \pi B$. The mean density of the perturbation is then

$$\rho = \frac{3}{32\pi GB^2} \tag{2.4}$$

The mean density of the surrounding universe evolves as

$$\rho_{\rm bg} = \frac{1}{6\pi Gt^2} \tag{2.5}$$

Therefore, when $t = \pi B$,

$$\rho = \frac{9\pi^2}{16}\rho_{\rm bg} \tag{2.6}$$

However, while such general properties can be analytically derived, the density at a specific point and time is not easily determined. If the spherical symmetry is even slightly broken, analytic techniques lose their effectiveness. In order to accurately investigate such situations in sufficient detail, numerical simulations must be used. These simulations use particles to trace the evolution of the inital distribution function as systems evolve. A variety of numerical techniques have been developed in order to improve the efficiency of simulations. This chapter presents the numerical tools and methods that will be used throughout the remaining chapters to investigate the local distribution of dark matter. First, the problem of cosmological simulations is reduced from a full general relativistic problem to a much simpler Newtonian model. Three different N-body algorithms are then presented – mesh codes, treecodes, and multipole codes – with advantages and disadvantages of each discussed.

2.1 Newtonian Approximation

Dark matter is of fundamental importance on cosmological scales. It is inseparably linked to the eventual fate of the universe — whether the universe eventually collapses or continues to expand forever. However, in most situations, the evolution of dark matter can be modelled in a strictly Newtonian framework. In regions of space where the densities are relatively low and velocities small, the full equations of General Relativity can be approximated to yield (Peebles, 1982)

$$\nabla^2\Phi = 4\pi G\left(\rho + \frac{p}{c^2}\right) - \Lambda \tag{2.7}$$

where Φ is the gravitational potential, G is the gravitational constant, ρ is the density, p is the pressure and Λ is the cosmological constant. In cases where pressure is negligible, such as with collisionless dark matter, $p = 0$. Additionally, when matter is present, generally $4\pi G\rho \gg \Lambda$. For example, in a virialized system the matter density is roughly 200 times the cosmological background density and $4\pi G\rho \sim 300H_0^2$.

This dominates the cosmological constant term, $\Lambda \sim H_0^2$, which can therefore be neglected. We are then left with Newton's classical formulation of gravity:

$$\nabla^2\Phi = 4\pi G\rho \tag{2.8}$$

It is only in situations where the weak-field approximation breaks down that one must consider general relativistic effects. These situations, such as dynamics very close to a black hole, are generally the study of much more detailed simulations (see for example Yo et al., 2002; Shibata and Uryū, 2002). On scales of galaxy and cluster formation, these effects are ignored, or approximated when modelled in larger systems (e.g. considering black holes as simple point masses).

2.2 N-Body Simulations

Numerical simulations play a crucial role in our understanding of structure formation. While analytic techniques can yield general information about the overall evolution of a system, they lack the ability to make detailed and specific predictions of complex systems. In contrast, numerical simulations provide a detailed realization of the system in question with an accuracy limited only by the available computational resources. However, in order to make the most efficient use of the computers, it is necessary to develop optimized algorithms for the calculation of gravitational forces. In the simplest N-body code implementation, forces of the N particles are simply calculated pair-wise between all particles. The computational requirements of this method are of order $O(N^2)$. For small particle numbers such as $N \approx 1000$, this technique is acceptable. However, the time taken to compute the forces for larger values of N rapidly becomes prohibitive. Therefore, several specialized algorithms, which will be discussed in the following sections, for computing the forces between particles have been developed which scale as $O(N \log N)$ or better.

However, once the forces are known, the positions and velocities of the particles can be updated. Frequently a "leap-frog" integration scheme is used where the

updating of the phase-space coordinates of a particle is split into three stages. For a given particle, the position, $\vec{x}$, and velocity, $\vec{v}$, are updated using:

$$\vec{v}_{n+1/2} = \vec{v}_n + \vec{a}_n \Delta t/2 \tag{2.9}$$

$$\vec{x}_{n+1} = \vec{x}_n + \vec{v}_{n+1/2} \Delta t \tag{2.10}$$

$$\vec{v}_{n+1} = \vec{v}_{n+1/2} + \vec{a}_{n+1} \Delta t/2 \tag{2.11}$$

where the subscripts indicate the timestep (ie. at $t = n\Delta t$), Δt is the time step of the simulation, and $\vec{a}$ is the acceleration of the particle. While this integration algorithm is quite simple it has the fortunate property of being sympletic which gives it better numerical stability than many higher-order, more complex integration schemes (Hut et al., 1995). However, in any N-body simulation, the most difficult task is the calculation of the accelerations.

2.3 Mesh Based Codes

One approach to speed up the force calculation is to calculate the potential at a set of points throughout the simulation and extrapolate the forces from the potential (Hockney and Eastwood, 1988). Poisson's equation must be solved to determine the potential:

$$\nabla^2 \Phi(\vec{x}) = 4\pi G \rho(\vec{x}) \tag{2.12}$$

An efficient method to solve this equation is through Fourier transforms. Taking the transform of Poisson's equation yields

$$\hat{\Phi}(\vec{k}) = -\frac{4\pi G}{k^2} \hat{\rho}(\vec{k}) \tag{2.13}$$

Therefore, if the Fourier transform of the mass distribution, $\hat{\rho}(\vec{k})$, can be calculated, $\hat{\Phi}(\vec{x})$ can readily be determined from the inverse transform of equation (2.13). However, in N-body simulations, the mass distribution is represented by a set of discrete points, rather than a continuous field $\rho(\vec{x})$. Therefore, the discrete Fourier transform must be used. It can be applied most efficiently when the sampled points are

uniformly distributed. Unfortunately, the particles in gravitational simulations are not uniformly distributed and each particle must be assigned to a grid point. The simplest method, in which one assigns all the mass of a given particle to the nearest grid point, is quick and simple but the resulting forces lack sufficent accuracy. An alternative technique involves distributing the mass to all eight corners of the grid cell according to the particle's location in the cell. Higher order weighting schemes are also frequently used.

The potential at the location of the j^{th} mesh point in a $N_g \times N_g \times N_g$ mesh is given by

$$\Phi(\vec{x_j}) = \sum_{i=1, i\neq j}^{N_g^3} \frac{G}{|\vec{x}_j - \vec{x}_i|}\rho(x_i) \tag{2.14}$$

This is simply a convolution of two functions

$$\Phi = X * Y \tag{2.15}$$

where $X = Gx^{-1}$ and $Y = \rho(\vec{x})$. Application of the convolution theorem yields

$$\hat{\Phi} = \hat{X}\hat{Y} \tag{2.16}$$

Once the potential is calculated at the grid points, the acceleration of the particles can be interpolated. $\hat{X}$ can be calculated once at the beginning of the simulation and efficient algorithms exist for performing the Fourier transforms. As a result, forces from this technique can be calculated in $O(N_g \log_2 N_g)$ time. However, the use of Fourier transforms implicitly applies periodic boundary conditions to the simulation. It is possible to adapt this method to work with isolated conditions though its performance is degraded and memory requirements are significantly increased. In addition, the simulation resolution is determined by N_g, not just the number of particles used.

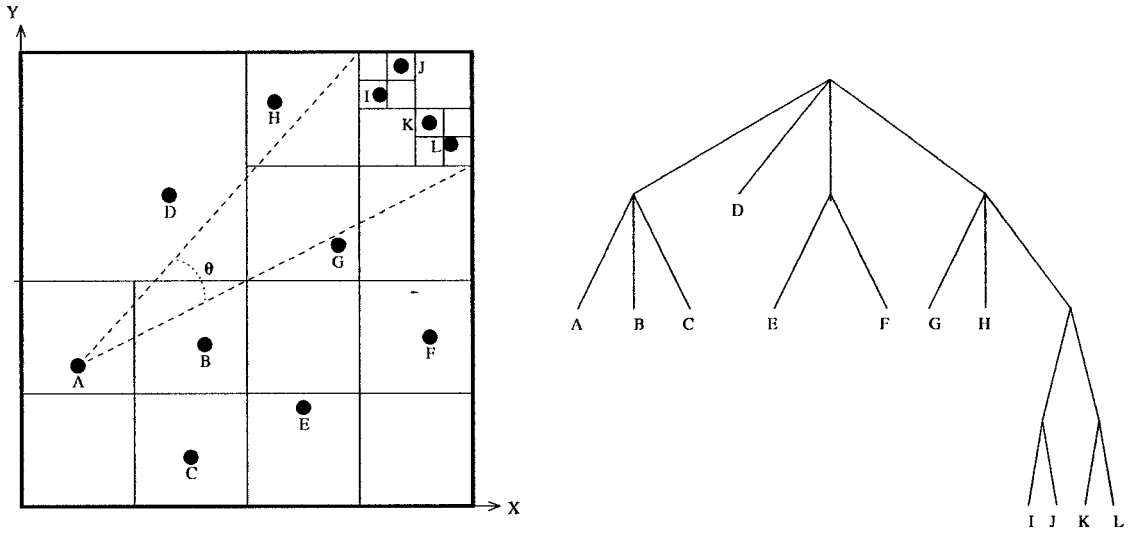

Figure 2.1: The initial particle distribution on the left can be geometrically divided recursively until each particle resides in its own cell. This division can be represented as the tree structure show on the right.

2.4 Treecodes

For isolated systems, treecodes are generally better suited. Unlike mesh codes, treecodes calculate forces directly rather than interpolating from the potential. The basic idea of a treecode, introduced by Barnes and Hut (1986), is that groups of other particles sufficiently distant from the particle of interest can be combined together and only the centre of mass (and possibly the higher moments) of that group need to be considered. For example, consider the 2-dimensional particle distribution illustrated in the left of Figure 2.1. The geometric extent of the particle distribution is divided into 4 equal areas. Each of these new regions is looked at in turn and if it has more than 1 particle in it, it is subdivided again. This process repeats until each particle resides in its own cell. This subdivision of particles can be represented by a tree structure as illustrated in Figure 2.1. In three dimensions, since each "parent" cell would have up to 8 "children" cells, the tree structure is commonly called an

"oct-tree".

To calculate the force on particle A, one starts at the top of the tree and computes the angle θ subtended by the current cell. In the case that the particle is inside the cell, it could be considered to subtend 360°. If the angle is greater than a pre-defined value, θ_0, then that cell is near enough that it must be looked at in more detail. If θ is less than θ_0, the cell is sufficiently distant that, in the simplest algorithm, it can be considered a point particle with the total mass of the cell situated at the cell's center of mass. Higher order moments of the cell are frequently included in more advanced versions of the algorithm for increased force accuracy. This process is then repeated for each of the child cells that must be examined more closely. This technique effectively reduces the $O(N^2)$ force calculation to $O(N \log N)$. For simulation of $N = 10^6$ particles, a relatively small simulation by today's standard, this represents a speed up of roughly 10^5 compared to the direct summation method. Note that the coefficients for the scalings are of the same order of magnitude but will be slightly larger for $O(N \log N)$ algorithms due to additional time required to construct the tree. Therefore, for a very small number of particles, direct summation may still be faster. By varying the value of θ_0, one can trade between speed and accuracy. A small value of θ_0 yields more accurate forces, but takes considerably longer than a larger value of θ_0. The prototypical implementation of this algorithm is provided by J. Barnes (http://www.ifa.hawaii.edu/~barnes/treecode/treeguide.html) and was the base code for the simulations described in Chapter 4. A simple improvement to the basic algorithm can be obtained by allowing more than one particle in the smallest cells of the tree. Forces between particles in the same cell are computed pairwise, but since grouping the particles reduces the number of cells in the tree, a net increase in efficiency can be obtained.

2.5 Multipole Expansion

While treecodes provide a very significant improvement over direct summations, they do not take advantage of the inherent symmetry of N-body interactions. The acceleration of each particle is calculated individually by traversing the entire tree structure, and depending upon its structure, the forces between pairs of particles are not guaranteed to be equal but opposite in direction. This imbalance leads to the well-known lack of momentum conservation inherent to treecodes. Dehnen (2000) has developed a new technique based upon the Cartesian Taylor expansion of gravitational forces which conserves momentum and is $O(N)$ instead of $O(N \log N)$. The basic idea is similar to that of a treecode, but instead of only considering the separation between a given particle and a distant region, this algorithm considers the separation between two *regions.* If two regions (or nodes, in the language of the algorithm) are sufficiently separated, the force of each node on each other can be approximated from the Taylor expansion of the gravitational force.

This algorithm is based on an oct-tree as discussed in Section 2.4. The primary difference between this algorithm and a standard treecode is the manner in which the tree is traversed. Instead of simply considering particle-particle and particle-cell interactions as in the standard treecode, cell-cell interactions are also considered. Consider the interaction between two cells (possibly the same cells) in the tree. There are three possible cases:

1. *Self-Interaction* The interactions between all of the children cells are calculated. This yields up to 36 new interaction pairs.

2. *Well-separated* The approximate forces between the two cells can be calculated.

3. *Not well-separated* The interactions between the smaller cell and the children of the larger cell are examined. This yields up to 8 new interaction pairs.

The tree traversal starts by looking at the self-interaction with the top-most cell.

Dehnen provides a version of this algorithm for public use. Unfortunately, the method of implementation he chose is not suitable for the tasks required for the studies in Chapter 3 and 5. In particular, it does not allow massless test particles, and is not guaranteed to be reversible. As will be discussed, these two requirements are essential for the techniques to be presented later. Additionally, the implementation by Dehnen only handled isolated systems. It could not deal with periodic boundary conditions. Therefore, a new implementation of this algorithm, which allows for both isolated and periodic systems, was implemented. In order to develop such a code, a detailed understanding of the technique is required.

2.5.1 Well-Separated Regions

To calculate the interaction between well-separated regions, consider two regions, $\mathcal{A}$, and $\mathcal{B}$ with centres of mass at $\vec{z}_\mathcal{A}$ and $\vec{z}_\mathcal{B}$ respectively. If $\vec{x}$ is the location of a particle in $\mathcal{A}$, and $\vec{y}$ is the location of a particle in $\mathcal{B}$, the potential between these two particles, $g(\vec{x}-\vec{y})$, can be expanded in a Taylor series about $\vec{R} = \vec{z}_\mathcal{A} - \vec{z}_\mathcal{B}$:

$$g(\vec{x}-\vec{y}) = \sum_{n=0}^{p} \frac{1}{n!}(\vec{x}-\vec{y}-\vec{R})^{(n)} \odot \nabla^{(n)} g(\vec{R}) + \mathcal{R}_p \tag{2.17}$$

where p is the order of the expansion and $\mathcal{R}_p$ is the remainder term. The notation used is that of Dehnen (2002) and references therein. $\vec{x}^{(n)}$ indicates the n^{th} outer product, while $\odot$ is the inner product.

The potential at position $\vec{x}$ in region $\mathcal{A}$ due to all particles in region $\mathcal{B}$ is given by (Dehnen, 2002):

$$\Phi_{\mathcal{B}\to\mathcal{A}}(\vec{x}) \approx -\sum_{m=0}^{p} \frac{1}{m!}(\vec{x}-\vec{z}_\mathcal{A})^{(m)} \odot \mathbf{C}^{m,p}_{\mathcal{B}\to\mathcal{A}} \tag{2.18}$$

$$\mathbf{C}^{m,p}_{\mathcal{B}\to\mathcal{A}} = \sum_{n=0}^{p-m} \frac{(-1)^n}{n!} \nabla^{(n+m)} g(\vec{R}) \odot \mathbf{M}^n_\mathcal{B} \tag{2.19}$$

$$\mathbf{M}^n_\mathcal{B} = \sum_{\vec{y}_i \in \mathcal{B}} m_i (\vec{y}_i - \vec{z}_\mathcal{B})^{(n)} \tag{2.20}$$

Since the expansion is based about the centres of mass, the dipole moment $\mathbf{M}^1$ vanishes. Typically a third-order expansion is used. For higher accuracy, it is

generally more efficient to introduce more stringent separation criteria rather than increase the order of the expansion, though there are exceptions to this (Dehnen, 2002). In the $p = 3$ case, the coefficients for the expansion are:

$$C^{0,3} = M_{\mathcal{B}} g(R) + \frac{1}{2} D_{ij} M_{\mathcal{B}}^{ij} - \frac{1}{6} D_{ijk} M_{\mathcal{B}}^{ijk} \tag{2.21}$$

$$C_i^{1,3} = M_{\mathcal{B}} D_i + \frac{1}{2} D_{ijk} M_{\mathcal{B}}^{jk} \tag{2.22}$$

$$C_{ij}^{2,3} = M_{\mathcal{B}} D_{ij} \tag{2.23}$$

$$C_{ijk}^{3,3} = M_{\mathcal{B}} D_{ijk} \tag{2.24}$$

where the fact that $\mathbf{M}^1 = 0$ was used and

$$D_i = \left. \frac{\partial g(\vec{r})}{\partial x_i} \right|_{\vec{r}=\vec{R}} \tag{2.25}$$

$$D_{ij} = \left. \frac{\partial^2 g(\vec{r})}{\partial x_i \partial x_j} \right|_{\vec{r}=\vec{R}} \tag{2.26}$$

$$D_{ijk} = \left. \frac{\partial^3 g(\vec{r})}{\partial x_i \partial x_j \partial x_k} \right|_{\vec{r}=\vec{R}} \tag{2.27}$$

(Note that a switch from tensor product operators to the summation convention was used.) Combining to give the potential at $\vec{x}$ due to the well-separated region $\mathcal{B}$ yields

$$\begin{aligned} \Phi(\vec{x}) = & -M_{\mathcal{B}} \left[g(\vec{R}) + \tfrac{1}{2} D_{ij} \tilde{M}_{\mathcal{B}}^{ij} - \tfrac{1}{6} D_{ijk} \tilde{M}_{\mathcal{B}}^{ijk} + d^i \left(D_i + \tfrac{1}{2} D_{ijk} \tilde{M}_{\mathcal{B}}^{jk} \right) \right. \\ & \left. + \tfrac{1}{2} d^i d^j D_{ik} + \tfrac{1}{6} d^i d^j d^k D_{ijk} \right] \end{aligned} \tag{2.28}$$

where $\vec{d} = \vec{x} - \vec{z}_{\mathcal{A}}$ and $\tilde{M}^{ij} = M^{ij}/M$, and $\tilde{M}^{ijk} = M^{ijk}/M$. The acceleration of particles in region $\mathcal{A}$ due to the mass distribution in region $\mathcal{B}$ is then

$$a_i(\vec{x}) = M_{\mathcal{B}} \left[\left(D_i + \frac{1}{2} D_{ijk} \tilde{M}_{\mathcal{B}}^{jk} \right) + d^j D_{ij} + \frac{1}{2} d^j d^k D_{ijk} \right] \tag{2.29}$$

Once the derivative tensors are calculated, the acceleration of each particle in region $\mathcal{A}$ can be updated. Note that $\mathbf{M}^3$ does not enter into the acceleration, only the potential. Therefore, if one is only interested in the acceleration, the $\mathbf{M}^3$ term can be neglected for improved speed and reduced memory requirements.

The real advantage of this technique becomes apparent when considering the acceleration of particles in region $\mathcal{B}$ due to particles in region $\mathcal{A}$. This effectively changes $\vec{R}$ to $-\vec{R}$. From the symmetry properties of the Green's function, $g(\vec{R}) = g(-\vec{R})$. Similar properties exist for the derivatives:

$$D_i(\vec{R}) = -D_i(-\vec{R}) \tag{2.30}$$

$$D_{ij}(\vec{R}) = D_{ij}(-\vec{R}) \tag{2.31}$$

$$D_{ijk}(\vec{R}) = -D_{ijk}(-\vec{R}) \tag{2.32}$$

Therefore, the majority of the computationally intensive terms for calculating the accelerations of particles in region $\mathcal{B}$ due to region $\mathcal{A}$ are already computed allowing for very fast reciprocal force calculations. It is this ability that increases the efficiency of multipole expansions over that of standard treecodes by reducing the number of interations by approximately a factor of 2. This also has the appealing feature that momentum conservation is guaranteed to be conserved since reciprocal forces are calculated correctly.

2.5.2 *Calculation of Forces*

In the algorithm described above, the acceleration of particles in well-separated nodes were updated immediately. This could result in a single particle having its acceleration calculated many times. While it is a straightforward application of the multipole expansion technique, it can be further improved by noting that the centres of Taylor expansion can be moved from a parent node, $\mathcal{P}$, to a child node, $\mathcal{C}$.

$$\vec{d} = \vec{x} - \vec{z'} + (\vec{z'} - \vec{z}) \tag{2.33}$$

$$= \vec{d'} + \Delta\vec{Z} \tag{2.34}$$

where $\vec{x}$ is a particle's position, $\vec{d}$ is its position relative to node's centre of mass, $\vec{z}$. The $'$ indicates the value is for the child node. Substituting into (2.28) and (2.29)

yields

$$\begin{aligned}\Phi(x) &= -M_{\mathcal{B}}\left[g(\vec{R}) + \frac{1}{2}D_{ij}\tilde{M}_{\mathcal{B}}^{ij} - \frac{1}{6}D_{ijk}\tilde{M}_{\mathcal{B}}^{ijk} + \Delta Z_i\left(D_i + \frac{1}{2}D_{ijk}\tilde{M}_{\mathcal{B}}^{jk}\right)\right. \\ &\quad \left. + \frac{1}{2}\Delta Z_i\Delta Z_j D_{ij} + \frac{1}{6}\Delta Z_i\Delta Z_j\Delta Z_k D_{ijk}\right] - a_i(x)d'_i \qquad (2.35) \\ a_i(\vec{x}) &= M_{\mathcal{B}}\left[\left(D_i + \frac{1}{2}D_{ijk}\tilde{M}_{\mathcal{B}}^{jk}\right) + (d'_j + \Delta Z_j)D_{ij} + \frac{1}{2}(d'_j + \Delta Z_j)(d'_k + \Delta Z_k)D_{ijk}\right] \\ &= M_{\mathcal{B}}\left[\left(D_i + \frac{1}{2}D_{ijk}\tilde{M}_{\mathcal{B}}^{jk} + \Delta Z_j D_{ij} + \frac{1}{2}\Delta Z_j\Delta Z_k D_{ijk}\right)\right. \\ &\quad \left. + d'_j\left(D_{ij} + \Delta Z_k D_{ijk}\right) + \frac{1}{2}d'_j d'_k D_{ijk}\right] \qquad (2.36)\end{aligned}$$

Therefore, the values of the Taylor coefficients from parent nodes can be propagated down into child nodes. This can be applied starting from the top of the tree down each branch until the particles are reached. Though this requires more memory to store all of the Taylor coefficients, it is significantly faster than applying the coefficients to each particle in a node every time it is involved in an interaction.

2.5.3 *Test Particles*

In the implementation of this multipole algorithm by Dehnen (2002), massless test particles were not supported. As will be discussed in Chapter 5, test particles will play an important role in the new techniques used to improve velocity space resolution. Test particles can be handled in almost the same way as massive particles, except they are ignored during the tree-building phase and then placed in the appropriate cell after the tree is constructed. In the limiting case where all test particles are in the same, bottom-most node of the tree, the computation could approach $O(N_{\text{test}}^2)$. For large N_{test} this is unacceptable. This can be avoided by the careful ordering of the particles in the tree-building stage by listing all massive particles before any test particles. If the forces are calculated starting at the top of the list, all test-test interactions will be at the end of the interaction list. Therefore, once the first test-test interaction is encountered, the remainder of the interactions can be skipped.

2.5.4 Non-periodic Potential

So far, no mention of the exact nature of the Green's function has been discused. While it will result in standard Newtonian gravity, the Green's function for periodic and non-periodic systems are different. For a non-periodic system, the Green's function is simply

$$g(\vec{r}) = \frac{1}{|\vec{r}|} \tag{2.37}$$

The derivative tensors are

$$\begin{aligned} g(R) &= |\vec{R}|^{-1} && (2.38)\\ D_i &= -R_i|\vec{R}|^{-3} && (2.39)\\ D_{ij} &= \left(3R_iR_j - \delta_{ij}|\vec{R}|^2\right)|\vec{R}|^{-5} && (2.40)\\ D_{ijk} &= -3\left(5R_iR_jR_k - (\delta_{ij}R_k + \delta_{ik}R_j + \delta_{jk}R_i)|\vec{R}|^2\right)|\vec{R}|^{-7} && (2.41) \end{aligned}$$

2.5.5 Periodic Potential

The Green's function for gravity subject to periodic boundary conditions is much more complicated than for the non-periodic case. A straightforward Fourier solution to Poisson's equation for a single point mass yields the Green's function for a periodic cube:

$$g(\vec{x}) = \sum_{k\neq 0} \frac{1}{k^2}\cos(\vec{k}\cdot\vec{x}) \tag{2.42}$$

Its derivatives are

$$\begin{aligned} D_i &= \sum_{k\neq 0} -\frac{k_i}{k^2}\sin(\vec{k}\cdot\vec{x}) && (2.43)\\ D_{ij} &= \sum_{k\neq 0} -\frac{k_ik_j}{k^2}\cos(\vec{k}\cdot\vec{x}) && (2.44)\\ D_{ijm} &= \sum_{k\neq 0} \frac{k_ik_jk_m}{k^2}\sin(\vec{k}\cdot\vec{x}) && (2.45) \end{aligned}$$

While the expressions have a compact elegance to them, the convergence properties are so poor that they are not useful. Figure 2.2 shows D_{xyz} for $|\vec{k}| < 100$. The

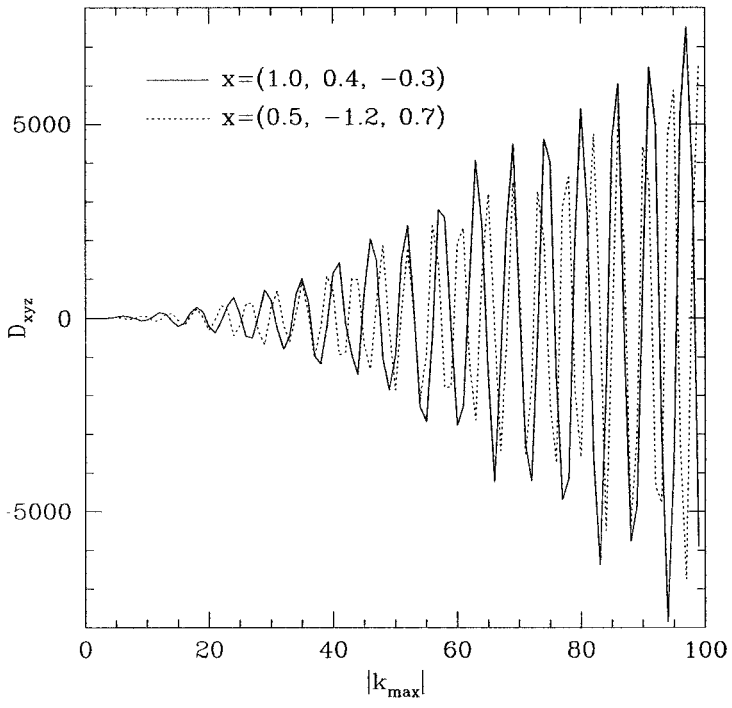

Figure 2.2: The poor convergence properties of equation (2.45) at two randomly chosen points in a cube with sides $L = 2\pi$.

sum widely oscillates between large positive and negative values. An alternative technique is to use Ewald summation (Hernquist et al., 1991). The basic idea is to consider the potential due to an infinite set of repeating cubic volumes. If one attempts to directly sum the contribution from all cubes, the sum will still converge very slowly. However, Ewald summation involves breaking this sum into two parts; one part which converges quickly in real space, the other part which converges quickly in Fourier space. This yields a new form which converges quite rapidly. (Note that Hernquist et al. (1991) has several typographical errors in their equation (2.14b) though their previous equation (2.11) is correct.) The Green's function for periodic gravity in Ewald form is

$$g(\vec{x}) = \frac{\pi}{\alpha^2 L^3} - \sum_{\vec{n}} \frac{\mathrm{erfc}(\alpha|\vec{x}-\vec{n}L|)}{|\vec{x}-\vec{n}L|} - \frac{1}{L}\sum_{\vec{h}\neq 0} \frac{1}{\pi|\vec{h}|^2} \exp\left(-\frac{\pi^2|\vec{h}|^2}{\alpha^2 L^2}\right) \cos\left(\frac{2\pi}{L}\vec{h}\cdot\vec{x}\right) \tag{2.46}$$

where L is the size of the periodic cube, and α is a convergence parameter effectively determing where the inital sum is split. Typical values which yield good accuracy are $\alpha = 2/L$, $|\vec{x}-\vec{n}L| < 2.6L$ and $|h|^2 < 8$ (Hernquist et al., 1991). The required derivative tensors are

$$\begin{aligned} D_i &= \sum_{\vec{n}} \frac{x_i - n_i L}{|\vec{x}-\vec{n}L|^3}\left[\frac{2\alpha|\vec{x}-\vec{n}L|}{\sqrt{\pi}}\exp\left(-\alpha^2|\vec{x}-\vec{n}L|^2\right) + \mathrm{erfc}\left(\alpha|\vec{x}-\vec{n}L|\right)\right] \\ &\quad + \frac{1}{L}\sum_{\vec{h}\neq 0}\frac{1}{\pi|\vec{h}|^2}\exp\left(-\frac{\pi^2|\vec{h}|^2}{\alpha^2 L^2}\right)\sin\left(\frac{2\pi}{L}\vec{h}\cdot\vec{x}\right)\left(\frac{2\pi}{L}\right)h_i \end{aligned} \tag{2.47}$$

$$\begin{aligned} D_{ij} &= -\sum_{\vec{n}}\frac{2\alpha}{\sqrt{\pi}}\frac{1}{|\vec{z}|^4}\exp\left(-\alpha^2|\vec{z}|^2\right)\left[z_i z_j(3+2\alpha^2|\vec{z}|^2) - \delta_{ij}|\vec{z}|^2\right] \\ &\quad + \frac{1}{|\vec{z}|^5}\mathrm{erfc}(\alpha|\vec{z}|)(3z_i z_j - \delta_{ij}|\vec{z}|^2) \\ &\quad + \frac{1}{L}\sum_{\vec{h}\neq 0}\frac{1}{\pi|\vec{h}|^2}\exp\left(-\frac{\pi^2|\vec{h}|^2}{\alpha^2 L^2}\right)\cos\left(\frac{2\pi}{L}\vec{h}\cdot\vec{x}\right)\left(\frac{2\pi}{L}\right)^2 h_i h_j \end{aligned} \tag{2.48}$$

$$\begin{aligned} D_{ijk} &= -\sum_{\vec{n}}\frac{2\alpha}{\sqrt{\pi}|\vec{z}|^4}\exp\left(-\alpha^2|\vec{z}|^2\right)\times \\ &\quad \left[(\delta_{ij}z_k + \delta_{ik}z_j + \delta_{jk}z_i)(3+2\alpha^2|\vec{z}|^2) - z_i z_j z_k\left(\frac{15}{|\vec{z}|^2} + 10\alpha^2 + 4\alpha^4|\vec{z}|^2\right)\right] \end{aligned}$$

$$+\frac{3}{|\vec{z}|^5}\mathrm{erfc}(\alpha|\vec{z}|)\left[\delta_{ij}z_k+\delta_{ik}z_j+\delta_{jk}z_i-\frac{5z_iz_jz_k}{|\vec{z}|^2}\right]$$
$$-\frac{1}{L}\sum_{\vec{h}\neq 0}\frac{1}{\pi|\vec{h}|^2}\exp\left(-\frac{\pi^2|\vec{h}|^2}{\alpha^2L^2}\right)\sin\left(\frac{2\pi}{L}\vec{h}\cdot\vec{x}\right)\left(\frac{2\pi}{L}\right)^3 h_ih_jh_k \tag{2.49}$$

where $\vec{z}=\vec{x}-\vec{n}L$.

Though these terms converge much more quickly than equation (2.42), the computational time required to calculate these terms is still prohibitive. The solution is to tabulate the values and use interpolation to quickly calculate the require terms. However, it is difficult to interpolate in regions near $|\vec{x}|=0$ due to the rapid divergence near the singularity. The solution is to multiply out the divergences and tabulate these values instead.

$$T_i = r^3D_i \tag{2.50}$$
$$T_{ij} = r^5D_{ij} \tag{2.51}$$
$$T_{ijk} = r^7D_{ijk} \tag{2.52}$$

These functions vary smoothly and slowly over their entire domain.

Symmetry can be used to reduce the number of terms which must be stored.

$$D_i = \frac{x_i}{|x_i|}D_i^+ \tag{2.53}$$
$$D_{ij} = \frac{x_i}{|x_i|}\frac{x_j}{|x_j|}D_{ij}^+ \tag{2.54}$$
$$D_{ijk} = \frac{x_i}{|x_i|}\frac{x_j}{|x_j|}\frac{x_k}{|x_k|}D_{ijk}^+ \tag{2.55}$$

where the superscript + indicates that the term is calculated at $(|x|,|y|,|z|)$. Therefore, only one octant needs to be tabulated.

2.5.6 Comoving Coordinates

In cosmological simulations, it is useful to perform simulations in comoving coordinates. In this manner, the simulation can be performed in a periodic box of fixed size, rather than having to expand the simulation volume as the universe evolves.

Comoving coordinates, $\vec{x}$, and physical coordinates, $\vec{r}$, are related through the expansion factor, $a(t)$, found in the Robertson-Walker cosmology (see Appendix A for details).

$$\vec{x} = \frac{\vec{r}}{a(t)} \tag{2.56}$$

Substituting this into the equation of motion

$$\ddot{\vec{r}} = -\vec{\nabla}\phi \tag{2.57}$$

yields

$$\ddot{\vec{x}} + 2H(t)\dot{\vec{x}} = -\frac{1}{a}\vec{\nabla}\phi - \frac{\ddot{a}}{a}\vec{x} \tag{2.58}$$

This can be simplified by noting that $\vec{\nabla} = a^{-1}\vec{\nabla}_x$ and that $\vec{x} = 1/2a^{-2}\vec{\nabla}_x r^2$. Therefore, the righthand side of equation (2.58) can be written as a potential in comoving coordinates

$$\ddot{\vec{x}} + 2H(t)\dot{\vec{x}} = -\frac{1}{a^3}\vec{\nabla}_x\varphi \tag{2.59}$$

where

$$\varphi = a\phi + \frac{\ddot{a}}{2}r^2 \tag{2.60}$$

Poisson's equation in comoving coordinates using this potential yields

$$\nabla_x^2\varphi = a^3\nabla^2\phi + 3\ddot{a}a^2 \tag{2.61}$$

The Friedmann equations (A.13) can be used to eliminate $\ddot{a}$, while Poisson's equation in physical coordinates can be used to remove ϕ.

$$\nabla_x^2\varphi = a^3 4\pi G\left(\rho(\vec{r},t) - \bar{\rho}(t)\right) + a^3\Lambda \tag{2.62}$$

Finally, if one uses comoving densities, the equations of motion in comoving coordinates become

$$\vec{u} = \dot{\vec{x}} \tag{2.63}$$

$$\dot{\vec{u}} + 2H(t)\vec{u} = -\frac{1}{a^3}\vec{\nabla}_x\varphi \tag{2.64}$$

$$\nabla_x^2\varphi = 4\pi G\left(\rho(\vec{x},t) - \bar{\rho}_0\right) + a^3\Lambda \tag{2.65}$$

where u is the peculiar velocity, and ρ_0 is the mean density when $a = 1$.

2.5.7 Energy Conservation

In periodic, co-moving cordinates, energy is no longer conserved. Layzer (1963) and Irvine (1961) showed that the energy equation in co-moving coordinates is

$$\frac{d}{dt}\left(a^4 T\right) + a\frac{dW}{dt} = 0 \tag{2.66}$$

where

$$T = \frac{1}{2}\sum_i m_i v_i^2 \tag{2.67}$$

$$W = \sum_i m_i \phi(\vec{x}_i) \tag{2.68}$$

This expression provides no conveniently conserved quantity. However equation (2.66) can be integrated to yield

$$a_n^4 T_n + a_n W_n - \int \dot{a} W dt = C \tag{2.69}$$

where the subscript n indicates at time t_n and $C = a_0^4 T_0 + a_0 W_0$. As suggested by Hockney and Eastwood (1988), a good measure of the consistency of a simulation is given by

$$R = (\Delta C)/(\Delta a W) \tag{2.70}$$

In all periodic simulations performed, it is verified that $R < 1 - 2\%$. If R is too large, either smaller timesteps or greater softening (discussed in the next section) must be used.

2.6 Softening

In numerical simulations, particles are point objects. Since the gravitational force is proportional to inverse square of the separation, if two particles pass very close to each other the code will calculate an exceptionally high force. However, the particles in the simulation are only tracers of the smooth underlying distribution and as such should not scatter off of each other. In order to overcome this numerical

issue, "softening" is generally applied. Effectively, softening changes the particles into extended distributions rather than point-like objects. There are numerous arguments about the physical validity of softening (Dehnen, 2001; Theis, 1998). However, when it is noted that the goal is not to try to simulate the evolution of exactly N point-like objects but instead follow a Monte-Carlo representation of the underlying true mass distribution, the arguments against softening generally fall apart.

2.6.1 Non-periodic Softening

One approach to softening is to consider each particle as an extended distribution. The nature of this distribution can be described by a unitless kernel, $\eta(x)$, such that

$$\int_0^1 4\pi x^2 \eta(x) dx = 1. \tag{2.71}$$

The kernel is finite in that $\eta(1) = 0$ and for $x > 1$, $\eta(x) = 0$. If a particle has a maximum extent of ϵ with a kernel $\eta(x)$, then the potential of such an object of mass M can be determined from Poisson's equation:

$$\nabla^2 \Phi(r) = 4\pi M \eta\left(\frac{r}{\epsilon}\right) \tag{2.72}$$

Therefore, the Green's function is

$$g(r) = \frac{1}{\epsilon} \begin{cases} \int_0^R \frac{M(x)}{x^2} dx & \text{if R} < 1 \\ R^{-1} & \text{if R} \geq 1 \end{cases} \tag{2.73}$$

where $R \equiv r/\epsilon$ and $M(r) = \int_0^r 4\pi x^2 \eta(x) dx$.

There are several criteria that must be considered when choosing the form of η. The first is the behaviour of test particles. In order for test particles to behave as expected — that a test particle with the exact phase-space coordinates of a real particle should follow the same trajectory as the real particle — the softening kernel must be chosen so that the force between particles goes to zero as their separation

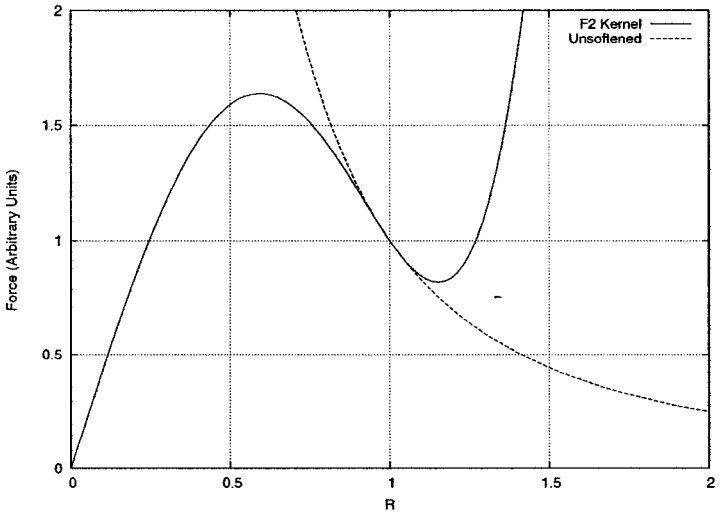

Figure 2.3: The F_2 softening kernel from Dehnen (2001) (solid curve) and unsoftened forces (dashed curve). Note that $R = r/\epsilon$ where ϵ is the softening parameter.

goes to zero. Dehnen (2001) proposes several such kernels which also reduce force errors relative to standard Plummer softening which is defined by

$$g(r) = \frac{1}{sqrtr^2 + \epsilon^2} \tag{2.74}$$

An additional criterion is that the potential and its derivatives should be smooth and continuous at $r = \epsilon$, at least to the order required by the expansion. The kernel implemented for isolated systems in the work presented later is the F_2 kernel.

$$\eta(x) = \frac{105}{32\pi}(1 - x^2)^2\Theta(1 - x^2) \tag{2.75}$$

where $\Theta(x)$ is the Heaviside function. From equation (2.73) the Green's function for this kernel is

$$g(r) = \frac{1}{16\epsilon}\left(35 - 35R^2 + 21R^4 - 5R^6\right) \tag{2.76}$$

where $R = r/\epsilon$. The behaviour of this softening kernel is shown in Figure 2.3. The derivative tensors required by equation (2.29) are

$$D_i = \frac{r_i}{\epsilon^3}\left(-\frac{35}{8} + \frac{21}{4}R^2 - \frac{15}{8}R^4\right) \tag{2.77}$$

$$D_{ij} = \frac{r_i r_j}{\epsilon^5}\left(\frac{21}{2} - \frac{15}{2}R^2\right) + \frac{\delta_{ij}}{\epsilon^3}\left(-\frac{35}{8} + \frac{21}{4}R^2 - \frac{15}{8}R^4\right) \quad (2.78)$$

$$D_{ijk} = -15\frac{r_i r_j r_k}{\epsilon^7} + \frac{\delta_{ij}r_k + \delta_{ik}r_j + \delta_{jk}r_i}{\epsilon^5}\left(\frac{21}{2} - \frac{15}{2}R^2\right) \quad (2.79)$$

2.6.2 Periodic Softening

When using a periodic potential, a spherically symmetric kernel function cannot simply be matched onto an unsoftened potential since the periodic potential in not spherically symmetric. Therefore, a simpler Plummer-like softening method was introduced. The softened derivative tensors were calculated from the tabulated values by replacing r with $\sqrt{r^2+\epsilon^2}$. Therefore, the softened derivatives are

$$D_i^s = T_i(r^2+\epsilon^2)^{-3/2} \quad (2.80)$$

$$D_{ij}^s = T_{ij}(r^2+\epsilon^2)^{-5/2} \quad (2.81)$$

$$D_{ijk}^s = T_{ijk}(r^2+\epsilon^2)^{-7/2} \quad (2.82)$$

$$(2.83)$$

2.6.3 Verification of Force Calculations

A version of the multipole expansion algorithm was implemented based upon the above derivations. It allowed test particles, optimal reversibility, and the choice of isolated or periodic boundary conditions.

All versions of the code were compared against **direct**; a standard $O(N^2)$ force calculation code developed at the University of Washington's N-Body Shop[1]. **direct** provides direct calculation of accelerations and energies for periodic and non-periodic forces.

[1] Website at http://www-hpcc.astro.washington.edu/

3. INTEGRITY OF NUMERICAL PHASE-SPACE STRUCTURES

3.1 Introduction

The phase-space distribution and evolution of matter in a system can be described by its distribution function, $f(\vec{x}, \vec{v}, t)$. Depending upon the situation under study, the distribution function (DF) can be interpreted either as the probability, the density, or the fraction of particles that are found in the phase-space volume $d^3x d^3v$. The evolution of the distribution function in gravitational, collisionless systems is governed by the collisionless Boltzmann equation (CBE) (see for example Binney and Tremaine, 1987, Chapter 4)

$$\frac{\partial f}{\partial t} + \sum_{i=0}^{6} \frac{\partial w_i}{\partial t} \frac{\partial f}{\partial w_i} = 0 \tag{3.1}$$

where $\vec{w} = (\vec{x}, \vec{v})$, and by Poisson's equation

$$\nabla^2 \Phi = 4\pi G M \int f(\vec{x}, \vec{v}) d^3v \tag{3.2}$$

where M is the total mass of the system and $\int f(\vec{x}, \vec{v}) d^3x d^3v = 1$.

In large numerical N-body simulations, particles are interpreted as tracers of the evolution of the underlying DF rather than individual point particles. Since the CBE is a special case of Liouville's theorem which states that the phase-space density about a comoving position in the system is constant (Binney and Tremaine, 1987, Chapter 4), under the CBE the topological dimension of the DF remains constant. Therefore, if the initial DF of the system does not extend into the full 6-dimensional

phase-space, all particles in the simulation should remain constrained to a subspace with the initial dimensionality. In particular, in Cold Dark Matter simulations, the DF of the initial conditions can be described as a three-dimensional "sheet" in six-dimensional phase-space which fills configuration space but with single-valued velocities at every position. As the DF evolves in time, the sheet will curl and fold but retain its three-dimensional nature though at a given position, there may now be multiple velocities.

In an ideal computer system with infinite numerical resolution it would be simple to accurately follow the evolution of this phase-space sheet. Unfortunately, numerical simulations must be run on non-ideal computers where in every calculation there exists the possibility of roundoff errors due to the finite number of digits stored. Roundoff errors are most significant when adding numbers which differ significantly in magnitude. For example, in a computer which can store 8 digits, adding $\delta = 1 \times 10^{-8}$ to 1 would yield 1 rather than 1.00000001. If this small number had to be added numerous times, this would result in a significant cumulative error. For example, if one tried to add δ to 1 one million times, it would still yield 1 rather than 1.01. Fortunately, this particular situation does not arise frequently and can be avoided by simply multiplying δ by 10^6 before adding in order to arrive at the correct answer.

Nonetheless, as a simulation evolves, roundoff errors do accumulate slowly, resulting in a divergence between the numerically integrated orbits and the "correct" trajectories. As the system becomes chaotic, these small roundoff errors are amplified exponentially. (However, Hut and Heggie (2001) indicate that in some cases, at later times in a simulation, the exponential divergence can change to a much slower power-law divergence.) As a result, the numerical simulations are no longer tracking the true DF. If roundoff errors are not kept carefully under control, particles begin to effectively sample random points near the true DF. In such a case, if one were to examine the nature of the DF found in the numerical simulation, a rather random

and smooth looking distribution may be obtained rather than the correct highly structured DF.

If the roundoff errors are sufficiently large and orbits diverge quickly, the integrity of the phase-space structure may be completely broken. The particles in the simulation may no longer even be near the correct DF. For example, the three-dimensional sheet mentioned above may fracture and expand to fill a six-dimensional volume. In simulations where an accurate model of the DF is required, such as the case of terrestrial dark-matter detection simulations, the breaking of the phase-space manifold must be avoided, or at least minimized.

3.2 Testing the Integrity

The primary source of roundoff errors in an N-body simulation occurs when two particles are close together and experience a very large mutual acceleration, a. If $a\Delta t$ (where Δt is the time step in the simulation) is large compared to the velocity of the particle, a significant roundoff error could occur when the velocity is updated. One solution is to soften the forces to reduce the maximum accelerations which a particle will feel. However, even with softening, one needs a means to verify that the phase-space sheet maintains its integrity. One simple method would be to fill the initial DF with a large number of test particles and evolve the system forward. With a sufficient number of test particles it would be straightforward to verify their topology. However, the number of test particles required would be computationally prohibitive. A more efficient alternative is to lay a single line of test particles in the DF. As the system evolves forward, the evolution of the line of test particles can be examined. If the phase-space distribution is maintained, this line of test particles should maintain its one-dimensional nature. Since the line of test particles in constrained to reside in the DF, if the test particles retain their line-like nature, so must the sheet-like nature of the full DF of massive particles be maintained. In contrast, if the line "breaks" and begins to fill a higher dimensional space, the initial

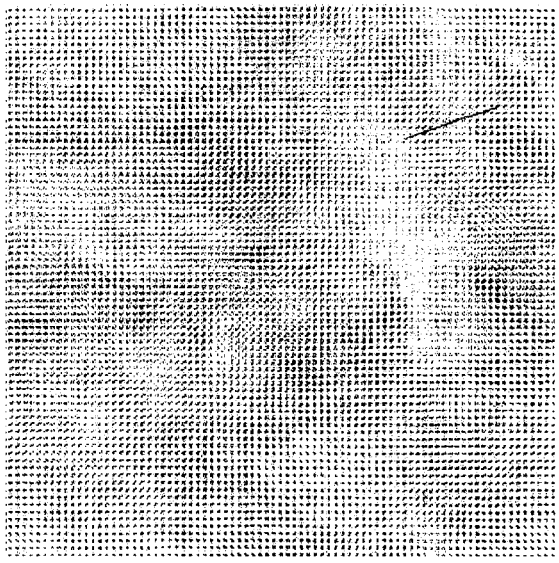

Figure 3.1: The initial conditions at $z = 15$ of the massive DF tracers and the line of test particles (green line). The line of test particles was chosen to pass through a region of higher density in the final state of the system. The comoving size of the cube is 20 Mpc on a side in present-day units.

three-dimensional phase-space sheet must also be broken.

3.3 N-body Example

To quantitatively examine this behaviour, it is useful to examine a simple CDM cosmological simulation. The initial conditions for an $N = 80^3$ N-body realization of the formation of a structure with approximately the mass of the Local Supercluster are shown in Figure 3.1. (The details of how such initial conditions are generated will be discussed in Chapter 6.) The massive particles which trace the evolution of the DF fill the configuration space of the simulation volume with a unique velocity at each point. The initial distribution function is a three-dimensional "sheet" in six-dimensional phase-space. Figure 3.1 also shows the line of 256000 test particles which lie in the initial DF and pass through a region of higher density in the final

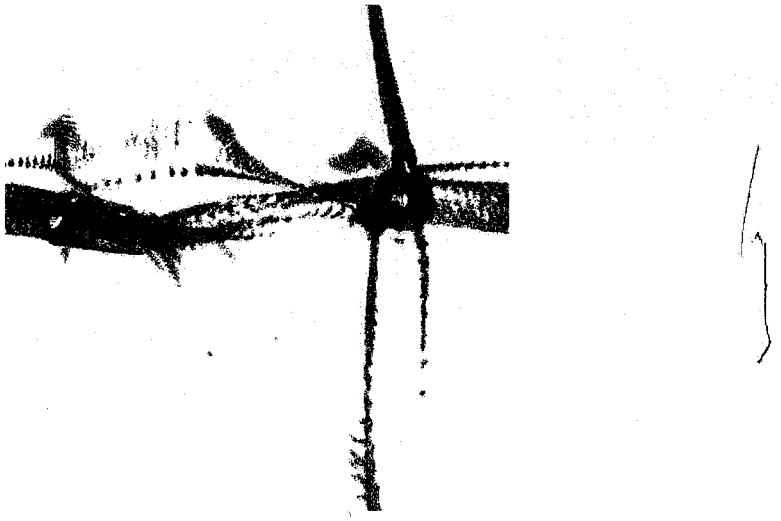

Figure 3.2: Simulation results for $\epsilon/\delta = 2$. Left: Final state of the simulation. Blue indicates regions of low density, while yellow regions are higher density areas. The width of the region shown is 20 Mpc. The green test particles can been seen in the cluster in the right side of the figure. Right: Close-up of the line of test particles. The line of test particles is coloured from red at one end to blue at the other. The excessive softening has greatly limited the dynamic evolution of the system. The width of this panel is 2 Mpc.

state of the system.

The left hand panel of Figures 3.2, 3.3, and 3.4 show the final state of the simulation at the present day, $z = 0$, for three different comoving softening lengths, expressed as the function of the initial grid spacing of the particles, δ, with $\epsilon/\delta = 2, 0.5, 0.0625$ respectively. The amount of substructure obviously increases with decreasing softening length; however, the fundamental question is how well the structure of the phase-space manifold is maintained. The right-hand panels of Figures 3.2, 3.3, and 3.4 show a close up of the line of test particles at the final stage of the simulation. For $\epsilon/\delta = 2$, the excessive softening damps the dynamic evolution of the system so that the line of test particles evolves only very slightly. The line-like nature of the test particles is still clearly evident. It is important to

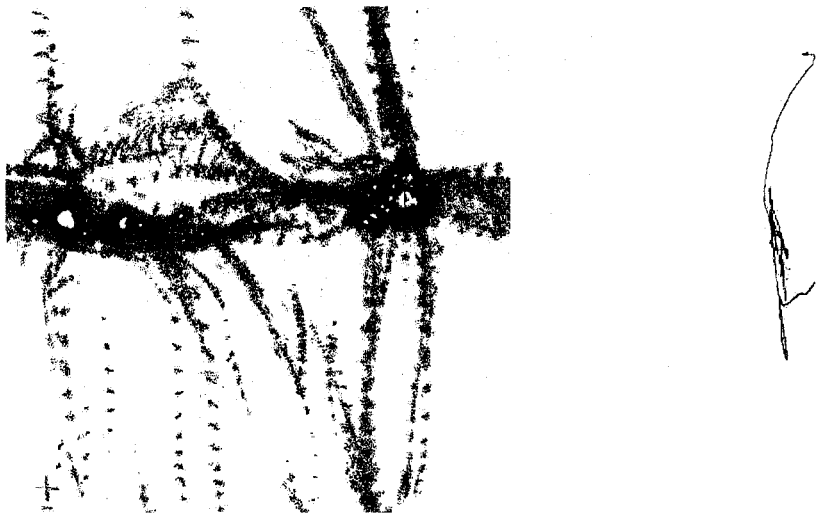

Figure 3.3: Simulation results for $\epsilon/\delta = 0.25$. Left: Final state of the simulation. Right: Close-up of the line of test particles. The system evolved into a complex final state but the line of test-particles still looks somewhat line-like in configuration space. The colouring and dimensions are the same as for Figure 3.2.

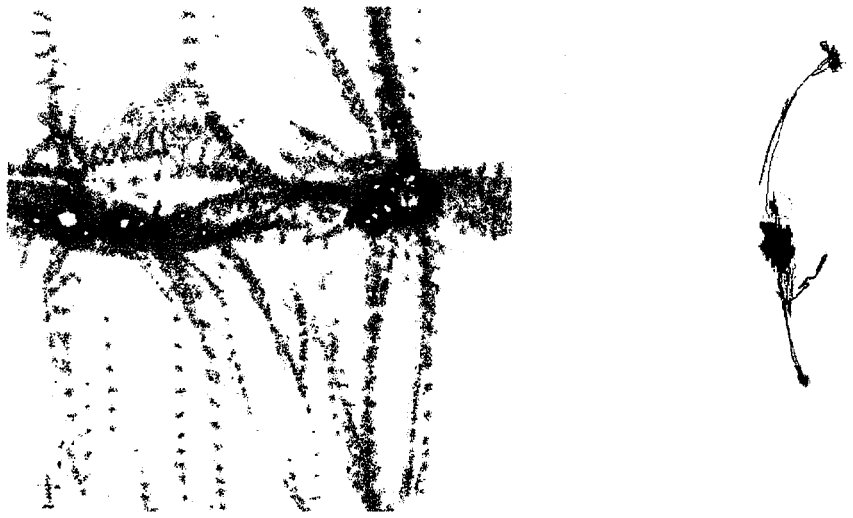

Figure 3.4: Simulation results for $\epsilon/\delta = 0.0625$. Left: Final state of the simulation. Right: Close-up of the line of test particles. The system evolved into a complex final state but the line-like nature of the distribution of test particles is destroyed. The colouring and dimensions are the same as for Figure 3.2.

remember that it must line-like in the full six-dimensional phase-space, not just the projected configuration-space shown in the figures. In Figure 3.3 the line evolves into a very complicated form but is appears to be quite line-like. However, in 3.4 with $\epsilon/\delta = 0.0625$, it is difficult to follow the complete line of test particles. In the central region it appears to be more cloud-like than line-like. In all simulations, the variation in the Layzer-Irvine energy equation (2.66) was verified to be less than 2.5%.

3.3.1 Dimensionality of the Test Particles

While the figures in the previous section indicated that for $\epsilon/\delta = 2$, the test particle distribution is probably still line-like, and for $\delta/\epsilon = 0.0625$, it probably is not, it is difficult to tell for the intermediate situation. A quantitative measure of the nature of the test particles is required to determine the point at which the test particles stop being line-like and the phase-space sheet is broken.

One technique to measure the dimension of a line of particles is to calculate the fractal Hausdorff-Besicovitch dimension, D_H (Mandelbrot, 1977). This involves dividing the line up into N segments each of equal length r so that the total measured length of the line is $L = Nr$. The fractal dimension is then given by

$$D_H = -\lim_{r \to 0} \frac{\log N}{\log r} \tag{3.3}$$

However, this definition only applies when the object under examination is known to be linear in nature. This definition can be generalized to d-dimensions by fitting N d-dimensional hyperspheres of radius r around the particle distribution and taking the limit. However, this is very difficult to implement in dimensions greater than two (Greenside et al., 1982).

An alternative definition of the Hausdorff-Besicovitch fractal dimension is the correlation dimension. First proposed by Grassberger and Procaccia (1983), it is easier to calculate than Haussdorff dimensions and no assumptions need to be made

about the underlying dimensionality of the system. It is based on the correlation function

$$C(r) = \frac{1}{N^2} \sum_{i}^{N} \sum_{j}^{N} \Theta(r - |\vec{x}_i - \vec{x}_j|) \tag{3.4}$$

where $\Theta(r)$ is the Heaviside function. $C(r)$ is simply the average fraction of the population which is separated by a distance less than r. The correlation dimension, D_c, arises if one assumes that $C(r)$ scales as a power of r for small r

$$C(r) \propto r^{D_c} \tag{3.5}$$

The value of D_c can be determined by calculating $C(r)$ for a variety of small r and looking at the logarithmic slope:

$$D_c = \lim_{r \to 0} \frac{d \log C(r)}{d \log r} \tag{3.6}$$

It can be shown that $D_c \leq D_H$ (Grassberger and Procaccia, 1983). Therefore, the correlation dimension will place a lower limit on the traditional Haussdorff dimension.

As long as the correlation dimension of the line of particles remains close to 1, the line will retain its one-dimensional nature. If the correlation dimension exceeds 2, the test particles will no longer be line-like. Since the line of test particles is constrained to reside in the sheet, if the line of test particles evolves properly, the sheet-like nature of the CDM DF must also be maintained. In contrast, if the line "breaks" and begins to fill a higher dimensional space ($D_c >= 2$), the initial three-dimensional phase-space sheet must be broken.

In order to calculate the separation of particles in phase-space, it is necessary to convert the velocities into distances by multiplying them by a characteristic time, t_c, for the system. One natural timescale arises from the mean density of the system, $\bar{\rho}$.

$$t_c = \frac{1}{\sqrt{G\bar{\rho}}} \tag{3.7}$$

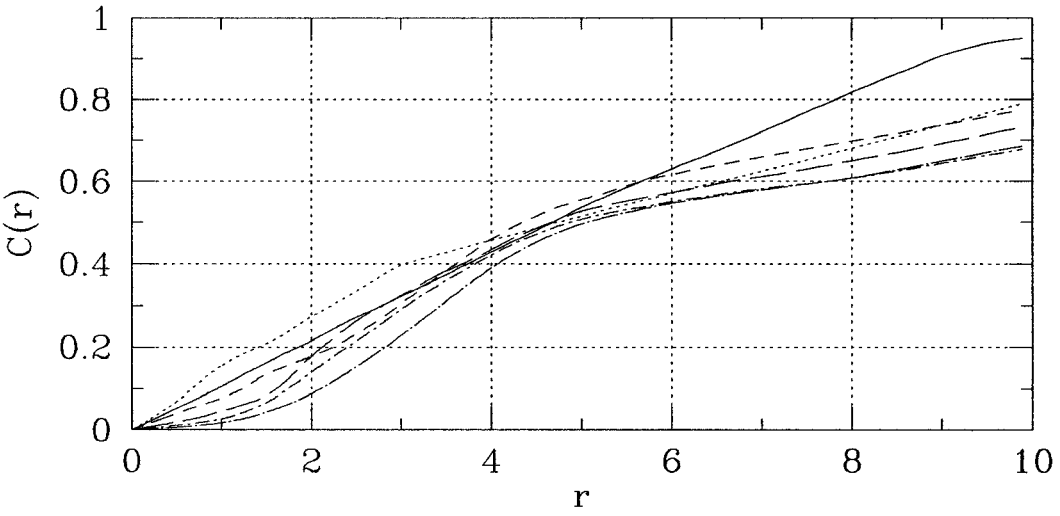

Figure 3.5: The correlation function for $\epsilon/\delta = 2$ (solid), 1 (dotted), 0.5 (short-dash), 0.25 (long-dash), 0.125 (short-dash-dot), and 0.0625 (long-dash-dot).

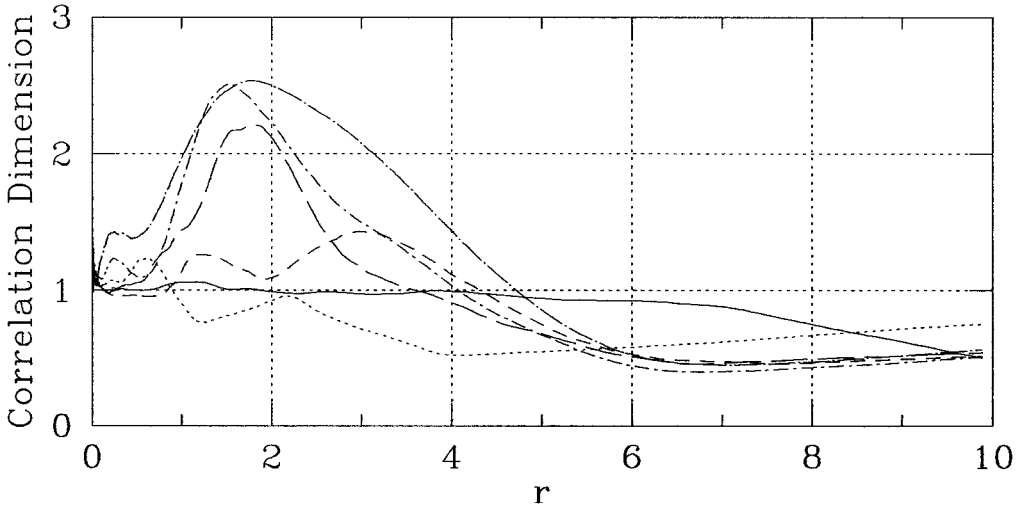

Figure 3.6: The correlation dimension for the same simulations (with the same line types) as in Figure 3.5. Note for $\epsilon/\delta < 0.25$ the correlation dimension exceeds 2 indicating that the phase-space sheet is broken.

Using this characteristic time, the numerical values of the scaled velocities span a range similar to the numerical range of positions in the region of interest.

Figures 3.5 and 3.6 show the correlation function and the correlation dimension for each of the simulations from the previous section and several intermediate values. Note that for large ϵ/δ, the correlation dimension is close to 1 for small r, while for smaller ϵ/δ the correlation dimension increases. For $\epsilon/\delta < 0.25$, D_c exceeds 2 indicating that the test particles are no longer linear in nature and the phase-space sheet must be broken. Note that the decrease in the correlation dimension past its peak in Figure 3.6 as $r \rightarrow 0$ arises due to the finite number of particles used. The most accurate description of the dimension of the line would be the maximum value.

3.4 Phase-Space Integrity and Reversibility

The evolution of phase-space structures can occur through two different processes:

- phase mixing (Binney and Tremaine, 1987) and,
- violent relaxation (Lynden-Bell, 1967) or chaotic mixing (Merritt and Valluri, 1996).

Phase mixing is the gradual change in the distribution of particles which maintain constant energy. For example, a group of particles on circular orbits at the same angular position, but slightly different radii, will slowly evolve into a spiral structure as the particles at smaller radius travel slightly faster than those particles farther out. Given sufficient time, this process can result in a smooth coarse-grained distribution function, though the underlying fine-grained DF is not smooth.

Unlike phase mixing, violent relaxation and chaotic mixing result when particles change energy due to a time-varying potential. This can result in fine-grained mixing of the DF and could remove the dependence of the final state of the system upon the initial DF. However, Henriksen and Widrow (1997) find that in self-similar

spherical collapse models, violent relaxation is not sufficient to completely remove this dependence though it does introduce instabilities in their models.

Independent of the mechanism with which the phase-space structure evolved, the simulation should be reversible. It may be more difficult if chaotic mixing dominates evolution of phase-space structures due to the increased degree of mixing. In particular, the phase-space structure of numerical simulations which have a small softening length can be broken due to the exponential growth of roundoff errors in the chaotic system. Since each individual roundoff error is effectively random, and each error is amplified exponentially, the trajectories rapidly change from a coherent phase-space structure to a random sample of orbits which are restricted by the dynamics of the system. For example, deep inside a potential well, the orbits may no longer follow the initial phase-space sheet, but particles will still be trapped in the well. This numerical effect, which could be incorrectly interpreted as physical chaotic mixing, may lead one to erroneously conclude that the particle distribution has much more randomness, and appears smooth in nature since the particles are simply constrained by the mean potential of the region. However, the true nature of the distribution could be very different, such as a series of discrete velocities.

This randomization of the orbits of particles is closely related to the reversibility of the N-body system. Once the phase-space structure has been destroyed, it is not possible to properly integrate the trajectories of particles back to their initial time. After a particle has moved onto a random orbit, it cannot return to its correct orbit by simple time reversal. Figure 3.7 illustrates how the reversibility on the simulations from the previous section depends upon the softening length used. As expected, simulations with larger softening lengths reverse better than simulations with smaller softening lengths. Simulations with $\epsilon/\delta < 0.1$ completely fail to reverse. However, the phase-space sheet may be slightly broken at values above this. In order to quantitatively determine the point at which phase-space structures are no longer followed accurately, one can look at the correlation between the reversibility of the

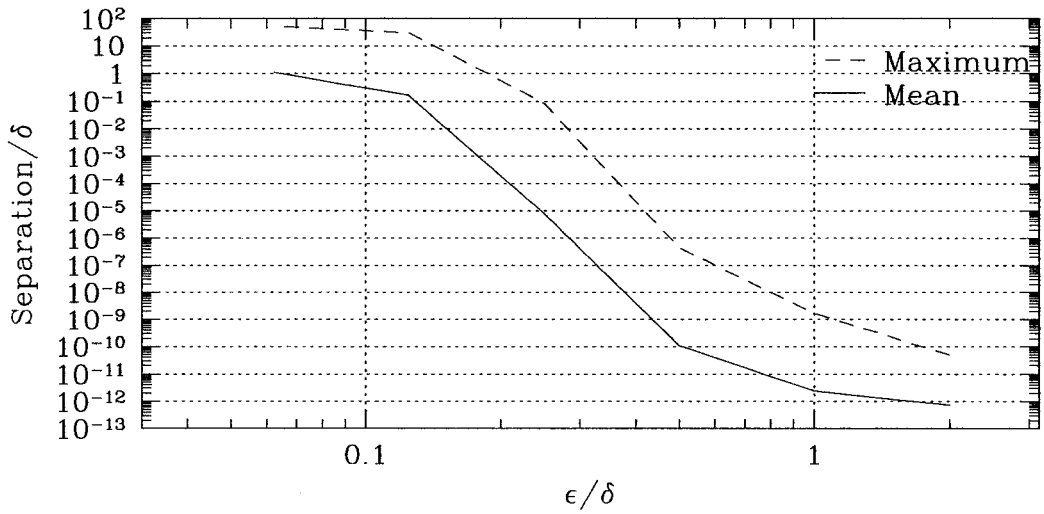

Figure 3.7: The average (solid line) and maximum (dashed line) distance (in units of the grid spacing) between the initial and reverse positions of particles for simulations with various softening lengths. For small ϵ/δ, the system fails to reverse properly.

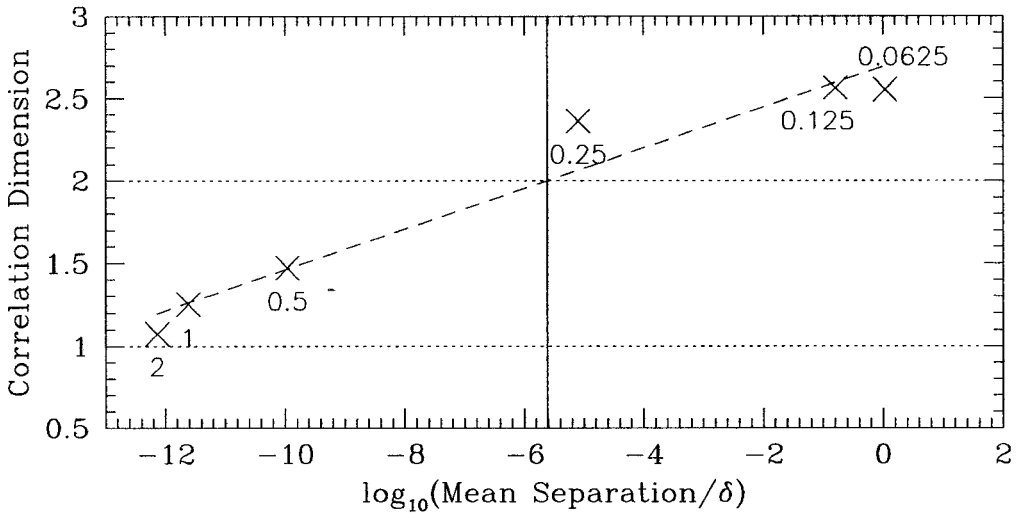

Figure 3.8: Correlation dimension of the line of test particles versus the accuracy with which a simulation can be reversed. The value of ϵ/δ is given by each data point. The dashed line is a least-squares fit to the points. The solid vertical line indicates where the least squares fit crosses $D_c = 2$.

system and the dimensionality of the test particle distribution. Figure 3.8 illustrates this relationship. The dashed line is the least-squares fit to the data points. At a mean reversibility separation of about $4 \times 10^{-6}\delta$, the correlation dimension exceeds 2, indicating that the integrity of the phase-space structure has been lost. From Figure 3.7, this corresponds to $\epsilon/\delta \sim 0.28$. Therefore, in order to maintain the proper phase-space structure of the system, the softening length should not be less than approximately one-quarter the size of the initial grid spacing. Note that this limit is determined for the multipole code and softening techniques described in Chapter 2. For other numerical codes, this limit will depend slightly upon the details of the algorithm such as type of softening implemented and the integration techniques used. In additional, if the system is evolved for more dynamical times, the optimal value of ϵ/δ may vary as well.

Nonetheless, the size of softening required to maintain phase-space integrity is significantly larger than the value used in traditional simulations. For example, in Ghigna et al. (2000), a softening length of 2 kpc is used in a halo with a radius of $R = 2000$ kpc and 4 million particles. A value of the initial grid spacing is not given, but if these particles were uniformly distributed, it would yield a grid spacing of approximately 20 kpc with $\epsilon/\delta = 0.1$. This value is an upper limit since the halo is roughly 200 times denser than the background which significantly reduces the estimated grid spacing. Therefore, while these simulations may reasonably follow configuration-space features, it is unlikely that the full phase-space structure is correctly maintained. Measurements of the local velocity distribution at specific points within the simulation would yield random velocities simply constrained by the depth of the potential, rather than the correct features of the phase-space distribution. Estimates of the terrestrial dark matter distribution obtained from these traditional simulations are therefore suspect. In order to obtain accurate models of the dark matter distribution in the solar neighbourhood, one must turn to methods other than direct simulation.

4. SEMI-ANALYTIC TECHNIQUE

In an ideal situation, computational resources would be sufficient that a straightforward, but very large, N-body simulation of the formation of the Milky Way or Local Group could yield detailed information about the phase-space structure of dark matter in the solar neighbourhood. Unfortunately, even using the efficient algorithms described in Chapter 2, current simulations are still several orders of magnitude too small to accurately resolve local velocity space information. Recent high-resolution numerical results (Helmi et al., 2003; Moore et al., 2001) indicate that the dark matter distribution in regions resembling the solar neighbourhood is quite smooth. However, even in these large simulations, there are only a few hundred particles per kpc^3 available to map out the velocity-space distribution. An important point to recall is that in early N-body simulations which were underresolved, it was concluded that the mass distribution was also smooth. However, when the resolution was increased, a wealth of substructure was revealed (Ghigna et al., 2000). It is possible that the same may occur as the velocity resolution increases.

Furthermore, even if a full N-body simulation did have sufficient resolution, in the bottom-up hierarchical formation scenario the history of the Milky Way is full of unpredictable mergers, encounters, and accretion events. A single simulation is not sufficient to investigate the full range of possible outcomes. Instead, even if the computational resources were available for a single simulation, a large set of simulations must be examined using a variety of initial conditions to generate a statistical model of the local dark matter phase-space distribution. Therefore, in order to investigate the dark matter distribution around the Earth one must turn to alternative methods. One such approach is to take advantage of analytic models

to reduce the computational complexity. In particular, if one could analytically model the formation history of the Milky Way, the laborious task of using N-body simulations to detect merger events would be reduced and instead the focus could be placed on analyzing the merger events themselves and the resulting dark matter distribution in the solar neighbourhood.

4.1 Probability Distribution of Halo Substructure

The aim is to estimate the probability that the local complement of dark matter particles includes a measurable contribution from a gravitationally bound clump or tidal stream. This clump or stream could significantly skew the local velocity-space distribution of dark matter away from the traditionally assumed smooth models. We focus on clumps that have made up to four orbits through the Galaxy by the present day — i.e., clumps that started to fall into the Milky Way at a redshift $z \lesssim 1$. The local distribution of dark matter particles is therefore divided into two components – a smooth background composed of particles that were accreted at early times (the substructure of which has since been erased by dynamical processes) and inhomogeneous material from recent accretion events. We assume that for $z \lesssim 1$, changes in the gravitational potential of the Galaxy are gradual and that clump-clump interactions can be ignored. Under these assumptions, recent accretion events can be studied numerically by evolving individual subclumps in a smooth, time-dependent model potential. Our assumptions are based on a variety of arguments which indicate that the recent accretion rate onto the inner parts of the Galaxy has been relatively low. The coldness and thinness of the Galactic disk, for example, limit the infall rate of satellites since they can transfer energy to stars in the disk (Toth and Ostriker, 1992). Measurements of the ages and metallicities of stars in the Milky Way's halo suggest that less than 10% of the halo stars come from recent merger events (Unavane et al., 1996). By contrast, numerical simulations and theoretical modeling imply that the mass of the extended dark halo has grown

by a factor of 2 or more since $z \simeq 1$. The conclusion is that most of the material accreted recently resides in the outer parts of the halo. Our analysis focuses on those few clumps that reach the inner regions of the Galaxy.

Our results are expressed in terms of a probability distribution function $dP/d\rho$, where dP is the probability that the density of dark matter particles in the solar neighbourhood associated with a single clump or stream is between ρ and $\rho + d\rho$. In general, we can write

$$\frac{dP}{d\rho} = \int \mathcal{N}(z_{\rm ta}, m, p_j)\, f(z_{\rm ta}, m, p_j; \rho)\, dz_{\rm ta} dp_j dm \tag{4.1}$$

where $\mathcal{N}(z_{\rm ta}, m, p_j)\, dz_{\rm ta} dp_j dm$ is the number of clumps accreted by the Galaxy with mass between m and $m + dm$, turnaround redshift between $z_{\rm ta}$ and $z_{\rm ta} + dz_{\rm ta}$ and orbital parameters (e.g., angular momentum) between p_j and $p_j + dp_j$. The turnaround redshift is defined as the epoch at which a clump breaks away from the expansion and begins to fall in toward the centre of the Galaxy. $\mathcal{N}$ is modelled using the extended Press-Schechter formalism (see Section 4.2.1). The dynamical evolution of accreted clumps within the Galactic halo is encoded in the function $f(z_{\rm ta}, m, p_j; \rho)d\rho$, which gives the probability that a clump characterized by the parameters m, $z_{\rm ta}$, and p_j contributes a density between ρ and $\rho + d\rho$ to the present-day density of dark matter in the solar neighbourhood.

Before proceeding to the elements of the model, we first reduce the calculation of f to a more tractable problem. Consider a volume V representative of the solar neighbourhood. For example, for an axisymmetric model consisting of a thin stellar disk and flattened dark matter halo, an appropriate choice for V is a thin circular tube in the disk plane with (large) radius $r_s = 8.5$ kpc, the distance between the Sun and the Galactic centre. Imagine that V is filled with hypothetical observers capable of making local measurements of the dark matter particles. For a given clump, we then have $f = V^{-1} dV/d\rho$, where dV/V is the fraction of observers who measure the dark matter density of the clump to be between ρ and $\rho + d\rho$. We will estimate f by

using N-body simulations to follow the orbital evolution and disruption of accreted clumps in the evolving Galactic halo.

We adopt a spherically symmetric model for the Galaxy, in which case the remaining parameters in equation (4.1) can be simplified considerably. Deviations from spherical symmetry alter the orbits of individual clumps but since we are interested in the properties of an ensemble of clumps the results assuming a spherical halo should provide an adequate approximation. For spherical models, there is a one-to-one relation between a clump's turnaround radius $r_{\rm ta}$ and $z_{\rm ta}$ (see Section 4.3.1). The sole remaining parameter required to fully specify the orbit of the clump is the specific angular momentum J at turnaround. For a spherically symmetric Galaxy model, the local volume V can be replaced by a thin spherical shell of surface area S and radius r_s. Equation (4.1) then takes the form

$$\frac{dP}{d\rho} = \frac{1}{4\pi r_s^2} \int \mathcal{N}\,(z_{\rm ta}, J, m)\, \frac{dS}{d\rho}\, dz_{\rm ta}\, dJ\, dm\ . \tag{4.2}$$

Despite the symmetry, evaluation of equation (4.2) appears daunting, since one must sample the space of initial conditions $(z_{\rm ta}, J)$ for all clump masses m and in each case determine $dS/d\rho$ from the output of a separate N-body simulation run to the present epoch $t = t_0$. This difficulty is alleviated by noting that the present state for the large space of orbital initial conditions can be sampled by considering a smaller set of orbits at various times. In Figure 4.1, for example, instead of following the different orbits a, b, c and evaluating them at $t = t_0$, it is possible to follow a single orbit and evaluate it at three different times such that the dynamical states at a', b', c' correspond closely to those above. Technically, it can be justified as follows: Let z_n and r_n denote the turnaround redshift and associated turnaround radius of a clump that reaches perigee today on its nth passage through the inner parts of the Galaxy. The simulations are performed with initial conditions selected from the set $(r_n,\ z_n)$, with the provision that $dS/d\rho$ is evaluated by performing an integral over time t taken from the time t_n of apogee before the nth passage through the inner

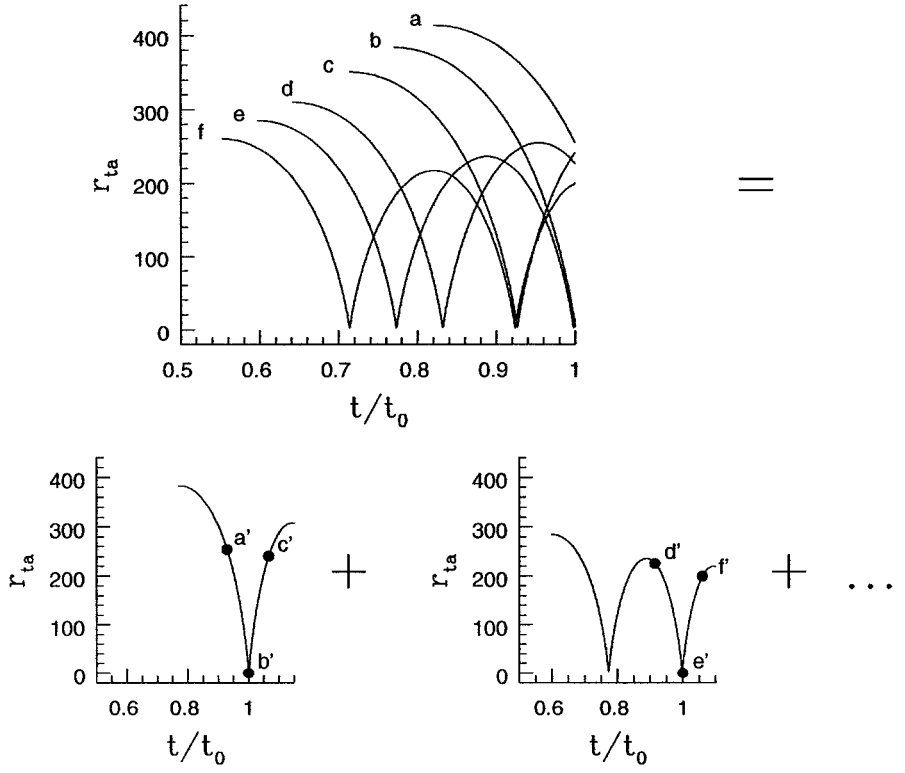

Figure 4.1: Schematic illustration of the change in variables from $z_{\rm ta}$ to t used in evaluating $dP/d\rho$. Top: six orbits that reach different radii at $t = t_0$. Bottom: two orbits used to approximate the contributions bracketed by orbits $a - c$ and $d - f$ of the top panel.

Galaxy ($t_n < t_0$) to the time t_{n+1} of apogee after the nth passage ($t_{n+1} > t_0$). As illustrated in Figure 4.1, this essentially corresponds to a change in equation (4.2) from an integration over $z_{\rm ta}$ to an integration over t with a sum over n.

In principle, z_n depends on the angular momentum J through the usual orbit equations. However, J must be relatively small, since $r_n \gg r_s$ for $1 < n < 4$, and therefore the dependence of z_n on J is negligible. Equation (4.2) can then be written

$$\frac{dP}{d\ln\rho} = \sum_{n=1}^{4}\left[\frac{1}{H_0}\frac{dz_{\rm ta}}{dt}\bigg|_{z_{\rm ta}=z_n} f_n(J,m) \times \int \mathcal{N}(z_n, J, m)\, dJ\, dm\right] \tag{4.3}$$

where

$$f_n(J,m) = \frac{H_0}{4\pi r_s^2}\int \frac{dS}{d\ln\rho}\, dt\ , \tag{4.4}$$

and where, for convenience, the probability distribution function is now defined with respect to $\ln\rho$ rather than ρ. The quantity f_n is dimensionless and will be used extensively in the discussion that follows. To evaluate equation (4.3), we select representative clumps characterized by m, J, and n, and follow their evolution via N-body simulations in a time-dependent model of the gravitational potential of the Galaxy. Hypothetical observers located on S measure the density as the different clumps pass by, allowing one to determine f_n numerically.

The response of a dark matter detector to particles in a clump or stream depends on their velocity distribution as well as their density. We can estimate the velocity dispersion in a stream using Liouville's theorem, which states that the density of particles in phase space is conserved. Consider an infalling, initially virialized clump of mass M with an initial characteristic density ρ_i and two-dimensional velocity dispersion $\sigma_i = (4\pi/3)^{1/6} G^{1/2} M^{1/3} \rho_i^{1/6}$. Here, ρ_i is the virial density, which we take to be 200 times the critical density of the universe at the formation time of the clump. (This definition agrees with the results from numerical simulations for an

$\Omega = 1, \Lambda = 0$ universe (Cole and Lacey, 1996) and is used by convention for other cosmologies as well.) Suppose that the density of the final disrupted clump at the detector is ρ_D. By Liouville's theorem, the corresponding velocity dispersion will be

$$\begin{aligned} \sigma_D &= \sigma_i \left(\frac{\rho_D}{\rho_i}\right)^{1/3} \\ &= 30\,\mathrm{km\,s^{-1}} \left(\frac{M}{10^{10} M_\odot} \frac{\rho_D}{0.03\,\rho_B}\right)^{1/3} \left(\frac{\rho_i}{0.03\,\rho_B}\right)^{-1/6}, \end{aligned} \tag{4.5}$$

where $\rho_B = 0.3\,\mathrm{GeV\,cm^{-3}} = 5.4 \times 10^{-25}\,\mathrm{g\,cm^{-3}}$ is the estimated value for the mean (background) density of dark matter particles in the solar neighbourhood. The fiducial value of $0.03\rho_B$ has been used, since the streams that are likely to have the biggest impact in a detection experiment have a present density $\rho_D \sim 0.03\,\rho_B$ (see Section 4.6). The last factor on the right-hand side of equation (4.5) depends on the formation time of the clump, but only weakly. The essential point is that the velocity dispersion of the disrupted clump is significantly less than the bulk velocity of the clump particles relative to the Earth, which is typically several hundred $\mathrm{km\,s^{-1}}$ for recently accreted clumps. The clump or stream therefore appears as a "cold", high-velocity distribution of particles.

4.2 The Merger History of Galaxies

To analytically model the merger history of the Milky Way, it is first necessary to examine the simpler case of the growth of a single, spherical perturbation. Consider a region of the early universe with a density, ρ, which is slightly greater than the mean density of the universe, $\bar{\rho}$. The deviation from smoothness can be quantified in terms of the overdensity or density contrast, δ:

$$\delta = \frac{\rho - \bar{\rho}}{\bar{\rho}} \tag{4.6}$$

Assuming that the remainder of the universe outside this region can be considered spherically symmetric, by Birkhoff's theorem this overdensity will evolve indepen-

dently. (For simplicity, a flat universe with no cosmological constant is assumed.) If the perturbation itself is also spherically symmetric, the equation of motion of a point on the boundary of the overdensity, r, will be

$$\ddot{r} = -\frac{GM}{r^2} \tag{4.7}$$

where M is the mass contained inside the perturbation. The parametric solution to this equation is

$$r = A(1 - \cos\theta) \tag{4.8}$$

$$t = B(\theta - \sin\theta) \tag{4.9}$$

where $A^3 = GMB^2$. This solution results in a singularity at $r = 0$ as θ goes to 2π. The time at which this occurs is frequently referred to as the collapse time, $t_{\rm coll}$, and is related to B by $t_{\rm coll} = 2\pi B$. At early times, equations (4.8) and (4.9) can be expanded for small θ.

$$r \approx A\left(\frac{\theta^2}{2} - \frac{\theta^4}{24} + \cdots\right) \tag{4.10}$$

$$t \approx B\left(\frac{\theta^3}{6} - \frac{\theta^5}{120} + \cdots\right) \tag{4.11}$$

Eliminating θ and using the definition of $t_{\rm coll}$ and $A^3 = GMB^2$, yields r as a direct function of t:

$$r = \frac{(GM)^{1/3}(6t)^{2/3}}{2}\left[1 - \frac{1}{20}\left(\frac{12\pi t}{t_{\rm coll}}\right)^{2/3}\right] \tag{4.12}$$

The density of the perturbation at early times is then

$$\begin{aligned}\rho &= \frac{3M}{4\pi r^3} \\ &= \frac{1}{6\pi G t^2}\left[1 - \frac{1}{20}\left(\frac{12\pi t}{t_{\rm coll}}\right)^{2/3}\right]^{-3} \\ &\approx \frac{1}{6\pi G t^2}\left[1 + \frac{3}{20}\left(\frac{12\pi t}{t_{\rm coll}}\right)^{2/3}\right]\end{aligned} \tag{4.13}$$

The mean density of a flat, matter-dominated universe evolves as

$$\bar{\rho} = \frac{1}{6\pi G t^2} \tag{4.14}$$

Therefore, at early times, the overdensity which would collapse to a singularity at $t_{\rm coll}$ grows as

$$\delta(t) = \frac{3(12\pi)^{2/3}}{20}\left(\frac{t}{t_{\rm coll}}\right)^{2/3} \tag{4.15}$$

A slightly different, and more useful, interpretation of equation (4.15) can be obtained by solving for $t_{\rm coll}$.

$$t_{\rm coll} = \left(\frac{\delta_c}{\delta}\right)^{3/2} t \tag{4.16}$$

where $\delta_c = 3(12\pi)^{2/3}/20 \sim 1.69$ is the critical density. Therefore, if at a given time t, the linearly extrapolated density perturbation exceeds the critical density, the density perturbation will have already collapsed.

By averaging over regions containing a mass M centred at $\vec{x}$, one can determine when objects of a given mass, rather than a given overdensity, have collapsed.

$$\delta(M,\vec{x}) = \int W_M(|\vec{x}-\vec{y}|)\delta(\vec{y})d^3\vec{y} \tag{4.17}$$

If $\delta(M,\vec{x}) > \delta_{c0}$, the region containing mass M centred at $\vec{x}$ will collapse by $t_{\rm coll}$. W_M is a window function chosen such that the total mass inside the function is M. In order to eliminate the positional dependence, one can look at the variance of perturbations of size M

$$\Sigma(M) = \sigma(M)^2 = \left\langle |\delta(M,\vec{x})|^2 \right\rangle \tag{4.18}$$

From the convolution theorem, the mass variance can also be expressed in terms of the Fourier transforms of the window function and overdensity

$$\Sigma(M) = \sum_{\vec{k}} \left\langle |\delta_{\vec{k}}|^2 \right\rangle \hat{W}_M^2(\vec{k}) \tag{4.19}$$

The Fourier transform of the density fluctuations is related to the power spectrum of the initial perturbations through

$$P(k) = \left\langle |\delta_k|^2 \right\rangle \tag{4.20}$$

If the windowing function is taken to be a step function in k-space, the fraction of mass bound in objects between mass M and $M + dM$ at time t can be shown to be (Press and Schechter, 1974; Lacey and Cole, 1994; Bond et al., 1991; Bower, 1991)

$$\frac{df}{dM} = \frac{\delta_c(t)}{\Sigma(3/2)(M)\sqrt{2\pi}} \left|\frac{d\Sigma(M)}{dM}\right| \exp\left(-\frac{\delta_c^2(t)}{2\Sigma(M)}\right) \tag{4.21}$$

4.2.1 Merger Histories

While equation (4.21) provides a useful model to describe how the mass in the universe is distributed, it is does not provide any information about how objects arrive in the predicted state. For example, if a large portion of the mass exists in a single clump, it does not answer whether it formed from a single large collapse, or through the merger of many smaller objects. The extended Press-Schechter technique (Bond et al., 1991; Lacey and Cole, 1993) provides an analytic means to model the growth of the Milky Way, or any cosmological conglomeration such as groups and clusters. If the present mass of the Galactic halo is M_0, then at redshift z the average number of progenitors of this halo that have mass between m and $m + dm$ is approximated by

$$\frac{dN}{dm}dm = \frac{1}{\sqrt{2\pi}} \frac{M_0}{m} \frac{\delta_c(z) - \delta_c(0)}{(\Sigma(m) - \Sigma(M_0))^{3/2}} \exp\left[\frac{(\delta_c(z) - \delta_c(0))^2}{2\left(\Sigma(m) - \Sigma(M_0)\right)}\right] \left|\frac{d\Sigma}{dm}\right| dm \tag{4.22}$$

where ρ_0 is the present mean density of the universe, and $\delta_c(z)$ is the amplitude that a linear density perturbation, extrapolated to the present epoch, must have in order for the associated object to reach turnaround by redshift z. In a matter-dominated, Einstein-de Sitter ($\Omega_0 = 1$) universe, $\delta_c(z) = \delta_{c0}\,(1 + z)$, where $\delta_{c0} \equiv \delta_c(t_0) = 0.15\,(3\pi^2)^{2/3} \simeq 1.44$. Note that this differs from the more common value discussed in the previous section of $\delta_{c0} = 0.15\,(12\pi)^{2/3} \simeq 1.69$ since the latter is associated with the collapse time, not the time of turnaround. In other cosmological models, the time-dependence of δ_c differs from the expression above, while the value of δ_{c0} is relatively insensitive to cosmological parameters (Lacey and Cole, 1993, for example). For definiteness, we assume a cold dark matter model universe with

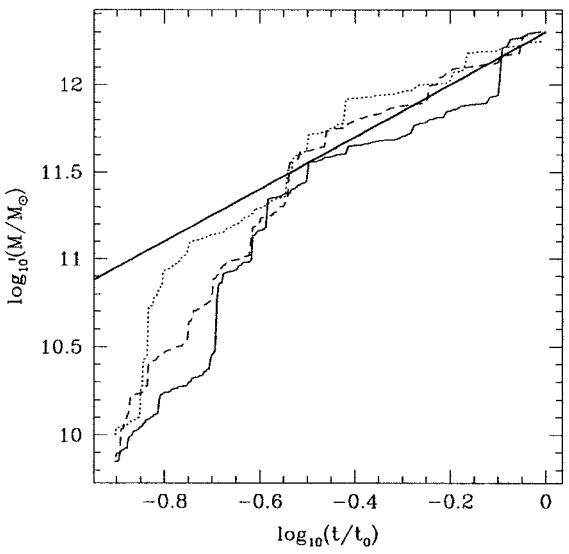

Figure 4.2: Three random realizations of the growth of a $2 \times 10^{12} M_\odot$ dark halo. The heavy straight line is the analytic fitting formula $M(t) = M_0(t/t_0)^{1.5}$ used to calculate $dP/d\rho$.

$\Omega_0 + \Omega_\Lambda = 1$, $\Omega_0 = 0.3$, and $h = 0.7$, where h is the present value of the Hubble parameter in units of $100\,\mathrm{km\,s^{-1}Mpc^{-1}}$, and Ω_0 and Ω_Λ are the contributions to the total mass density, in units of the critical density ρ_{crit}, from non-relativistic matter (dark matter and baryons) and the cosmological constant. The primordial power spectrum is chosen to have the scale-invariant form expected from inflation, $P_i(k) \sim k$, and the present spectrum is normalized to agree with the observed cluster abundance, i.e., $\sigma_8 = 0.90$. (This particular value is obtained from the algorithm described in Navarro et al. (1996).) This choice of cosmological model fixes the expression for $\delta_c(z)$ and also determines $\Sigma(M)$.

The average growth rate of a dark matter halo can be determined using eq. (4.22). Nusser and Sheth (1999) have developed a simple algorithm for generating possible histories of the most massive progenitor, several of which are shown in Figure 4.2. (See also Lacey and Cole, 1993; Somerville and Kolatt, 1999) Though there is sig-

nificant stochasticity in the various histories we assume a simple power-law model for the growth in mass of the Galactic halo

$$M(t) = M_0 \left(\frac{t}{t_0}\right)^{\alpha} , \tag{4.23}$$

where $\alpha = 1.5$ (solid line in Figure 4.2) for the cosmology that we have used. We adopt a Milky Way halo mass $M_0 = 2 \times 10^{12} M_{\odot}$, the value derived in Wilkinson and Evans (1999) from observations of globular clusters and satellite galaxies. The exact details of the halo growth do not significantly affect our calculation of $dP/d\rho$, since it is the long term deepening of the potential well of the Galaxy that is most important, not the short term fluctuations in the merger rate. In addition, we make the reasonable assumption that the angular momentum distribution for the accreting clumps is independent of their mass, so that the J-dependence of $\mathcal{N}$ separates out. This assumption, together with equations (4.22) and (4.23), yields the following approximate form for $\mathcal{N}$

$$\mathcal{N}(z_{\rm ta}, J, m) = \alpha M_0 \left(\frac{t_{\rm ta}}{t_0}\right)^{\alpha-1} \frac{dN}{dm} \chi(J, z_{\rm ta}) , \tag{4.24}$$

where $\chi(J, z_{\rm ta})$ is the normalized clump distribution as a function of angular momentum at turnaround ($\int dJ \chi(J, z_{\rm ta}) = 1$). In principle, χ may be determined from simulations or from a detailed analysis of tidal torques in the hierarchical clustering scenario. For the present discussion, we assume a scaling form for χ, namely $\chi(J, z_{\rm ta}) = \chi(J/J_{\rm circ}(z_{\rm ta}))$ where $J_{\rm circ}(z_{\rm ta})$ is the angular momentum for a clump in a circular orbit at the radius $r_{\rm ta}$. In particular, we assume that the clumps are uniformly distributed in J^2. χ then takes the form

$$\chi(J, z_{\rm ta}) dJ = \Theta(J_{\rm max} - J) \frac{2\beta^2}{J_{\rm circ}(z_{\rm ta})^2} J dJ \tag{4.25}$$

where $\Theta(x)$ is the Heaviside function, $\beta \equiv J_{\rm circ}/J_{\rm max}$, and $J_{\rm max}$ is a model parameter that characterizes the spread in angular momentum of the clumps. We adopt a value of $\beta = 2$, implying that the maximum angular momentum that a clump can have is

one-half that required for circular orbits. It is trivial to consider different choices of β since $dP/d\rho$ scales with β^2. At most, with our choice of β, we overestimate $dP/d\rho$ by a factor of 4. This would require merging clumps to be on circular orbits which is very unlikely. In fact, β could be significantly higher than 2 if infalling clumps are on predominantly radial orbits.

Though halos are never in true virial equilibrium, approximate equilibrium is reached provided no major merger events have occurred in the recent past. It is then customary to set the turnaround radius equal to twice the virial radius, r_{200}, where the latter is defined as the radius within which the mean density of the halo is $200\rho_{\rm crit}(t)$. For the ΛCDM model, the turnaround radius can then be written

$$\begin{aligned} r_{\rm ta}(t) &= 2\left(\frac{3M(t)}{800\pi\rho_{\rm crit}(t)}\right)^{1/3} \\ &= 520\,{\rm kpc}\left(\Omega_0\,(1+z)^3+1-\Omega_0\right)^{-1/3}\left(\frac{t}{t_0}\right)^{\alpha/3} . \end{aligned} \tag{4.26}$$

It is well known that the Press-Schechter mass distribution used above does not agree precisely with results from N-body simulations (e.g., Jenkins et al. (2001)). The mass function obtained from N-body simulations generally has more high-mass objects and fewer low-mass objects than the Press-Schechter distribution predicts. Correcting this difference would have little effect on our final value for $dP/d\rho$. The more massive infalling clumps would create larger tidal tails, thereby increasing the probability of encountering one today. On the other hand, there would also be fewer low-mass objects falling into the Milky Way. Taken together, these effects should partially cancel, suggesting that that the error introduced by using the Press-Schechter distribution instead of the numerically determined distribution should be small. Moreover, the Press-Schechter expression for the progenitor distribution at moderate redshift is more accurate than the Press-Schechter mass function at late times.

4.3 Model Parameters

4.3.1 Potential of the Milky Way

The simulations follow the evolution of an individual clump in a rigid, time-dependent gravitational potential designed to represent the Galaxy. We adopt a three-component model for the Galactic potential out to a truncation radius, $r_{\rm trunc}$, which is determined by the total mass of the system. Beyond the truncation radius, the potential is assumed to be Keplerian:

$$\Phi = \begin{cases} \Phi_{\rm halo} + \Phi_{\rm spher} + \Phi_{\rm disk} & \text{if } r < r_{\rm trunc} \\ -\frac{GM}{r} + \Phi_{\infty} & \text{if } r > r_{\rm trunc} \end{cases} \tag{4.27}$$

The model halo is described by a logarithmic potential, the spheroid by a Hernquist potential (Hernquist, 1990), and the disk by the spherical analog of a Miyamoto-Nagai potential (Johnston et al., 1996). The components of the Galactic potential in our model are thus:

$$\Phi_{\rm halo} = \frac{1}{2} v_{\rm halo}^2 \ln\left(r^2 + a^2\right) , \tag{4.28}$$

$$\Phi_{\rm spher} = -\frac{GM_{\rm spher}}{r+b} , \tag{4.29}$$

$$\Phi_{\rm disk} = -\frac{GM_{\rm disk}}{\left(r^2 + c^2\right)^{1/2}} , \tag{4.30}$$

where $v_{\rm halo}$, M, and a are all time-dependent, with $M(t)$ given by equation (4.23). We assume that $r_{\rm trunc}$ and a scale with time at the same rate as $r_{\rm ta}$ (equation (4.26)). The time dependence of $v_{\rm halo}$ is then set by the relation

$$v_{\rm halo}^2 = \frac{GM}{r_{\rm trunc}} \frac{r_{\rm trunc}^2 + a^2}{r_{\rm trunc}^2} \tag{4.31}$$

The disk and spheroid potentials are assumed to be time-independent. The values used for the disk and bulge are the same as those found in Johnston et al. (1996):

$b = 0.7\,\mathrm{kpc}$, $c = 6.5\,\mathrm{kpc}$, $M_{\mathrm{spher}} = 3.4 \times 10^{10} M_{\odot}$, and $M_{\mathrm{disk}} = 10^{11} M_{\odot}$. However, we adopt slightly different values for the present-day halo parameters: $a(t_0) = 16.5\,\mathrm{kpc}$ and $v_{\mathrm{halo}}(t_0) = 200\mathrm{km\ s^{-1}}$. These parameters imply a circular speed at r_s of $220\mathrm{km\ s^{-1}}$, the accepted IAU value. Additionally, the implied mass of the Milky Way halo within 200 kpc is $M_0 = 2 \times 10^{12} M_{\odot}$ in agreement with recent work on the dynamics of satellite galaxies and globular clusters (Wilkinson and Evans, 1999). The current value of the truncation radius in our model is $r_{\mathrm{trunc}} = 216$ kpc and the rotation curve is relatively flat out to this radius.

While the shapes of dark halos are not well constrained, the results of Ibata et al. (2001) on the tidal stream associated with the Sagittarius dwarf speriodal galaxy suggest that the Milky Way halo potential is close to spherical. The assumption of a spherical disk potential is less realistic but should not affect our results significantly. While a planar disk would cause the orbits of an otherwise spherical model to precess and leave the orbit plane, it will not affect the properties upon which our subsequent calculations are most dependent – the number and density of the tidal streams.

Selected orbits for which the clump reaches perigee at the present time, $t_0 = 13.5$ Gyr, on its first, second, third, or fourth orbits through the Galaxy are shown in the right panel of Figure 4.3. To construct these orbits, the (r_{ta}, J)-parameter space is sampled at random, and those initial conditions for which the orbits satisfy $r < r_s$ at $t = t_0$ are marked in the left panel of Figure 4.3. As noted above, the decrease in apogee with time is due to the time-dependent nature of the Galactic potential. The orbits are followed from turnaround, which occurs at redshifts $z_1 = 0.26$, $z_2 = 0.56$, $z_3 = 0.79$, and $z_4 = 1.0$ respectively.

4.3.2 *Structure of the Infalling Clumps*

We next turn our attention to the structure of the clumps at turnaround, before they have been subjected to the tidal fields of the Galaxy. We treat the clumps as composed purely of dark matter, i.e., we ignore the dynamical effects of baryons

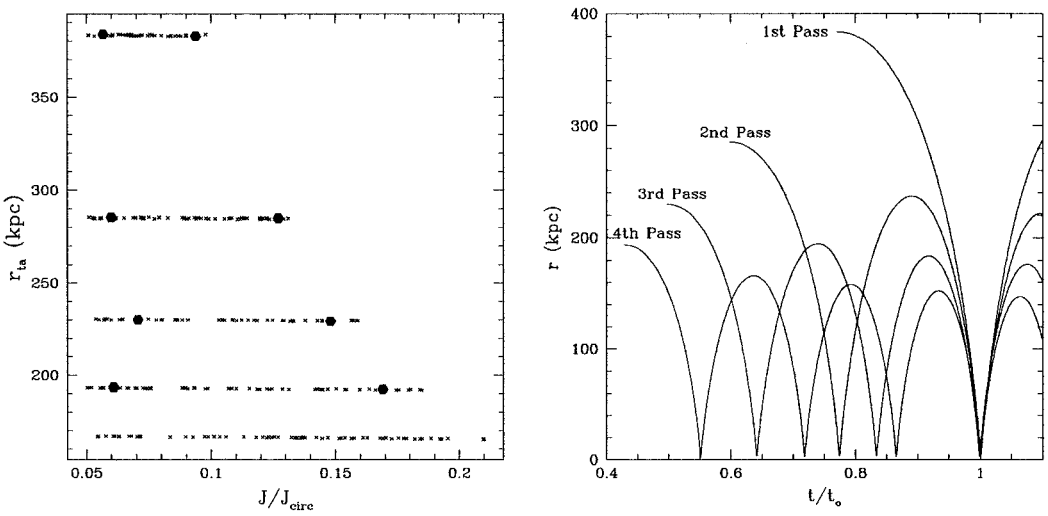

Figure 4.3: Initial condition parameter space and corresponding orbits. Left: $r_{ta} - J$ parameter space for orbits that are near the surface S at $t = t_0$. The strips of points at $r_{ta} = 380, 285, 230$, and 195 kpc correspond to particles that reach S after 1, 2, 3 or 4 orbits through the Galaxy respectively. (Those at $r_{ta} = 165$ kpc merger before $z = 1$ and are not considered.) The large dots are the initial conditions used in the numerical simulations. Right: Distance from the Galactic centre as a function of time for the orbits shown in the left panel.

in the clumps. Numerical simulations (e.g., Dubinski and Carlberg (1991); Navarro et al. (1996); Moore et al. (1998)) suggest that the density profiles of dark-matter halos have a 'universal' shape characterized by an inner power-law cusp and an r^{-3} density fall-off at large radii. These include the NFW profile (Navarro et al., 1996) and that proposed by Moore et al. (1998). However, for convenience, we model the infalling clumps as Hernquist spheres (Hernquist et al., 1991), for which the density profile is given by

$$\frac{\rho(r)}{\rho_{\rm crit}} = \frac{\xi_c a^4}{r\,(r+a)^3} \quad . \tag{4.32}$$

where $\rho_{\rm crit}$ is the critical density for closure, a is the scale radius of the halo, and ξ_c is the characteristic density in units of $\rho_{\rm crit}$. Since the density falls off asymptotically faster than r^{-3}, this model has the practical advantage that the total mass is finite, $M = 2\pi\xi_c\rho_{crit}a^3$, without having to impose a truncation radius. Furthermore, the corresponding particle distribution function, $f(E)$, can be expressed analytically for the Hernquist model, while no closed form is available for the NFW or Moore profiles (however, see Zhao, 1997; Widrow, 2000; Łokas and Mamon, 2001).

The characteristic density ξ_c and scale length a are determined using the algorithm outlined by Navarro et al. (1996). Given the virial mass, M_{200}, and the redshift at which the halo is identified (in our case the turnaround redshift), both the virial radius, r_{200}, and characteristic density, ξ_c, can be calculated independently of the halo model assumed. The virial mass and virial radius are defined through the relation

$$M_{200} \equiv \frac{800}{3}\pi r_{200}^3\rho_{crit} \quad . \tag{4.33}$$

ξ_c and r_{200} can then be used to calculate the scale length, a, of the Hernquist profile. For the Hernquist model, the virial mass, as derived from (4.32), is

$$M_{200} = 2\pi\xi_c\rho_{crit}a^3\frac{r_{200}^2}{(r_{200}+a)^2} \quad ; \tag{4.34}$$

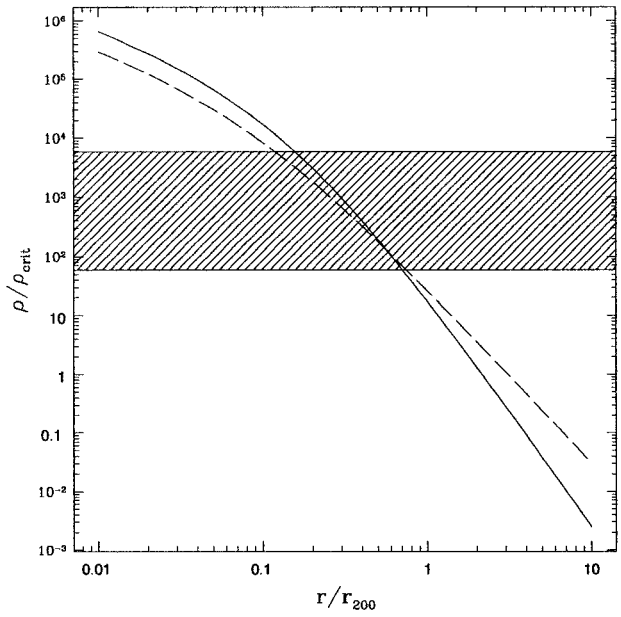

Figure 4.4: Density profiles for Hernquist (solid curve) and NFW (dashed curve) models assuming a virial mass, $10^9 M_\odot$. The shaded region corresponds to densities at the detector of $\rho = (10^{-3} - 10^{-1})\rho_B$ where $\rho_B = 6 \times 10^4 \rho_{\rm crit}$ is the density of dark-matter particles in the background.

when combined with the definition of M_{200} (equation (4.33)) it yields

$$\xi_c = \frac{400}{3} x(1+x)^2 \ , \tag{4.35}$$

where $x \equiv r_{200}/a$. Thus, once ξ_c and r_{200} are known, the scale length a can be readily calculated.

While we implicitly assumed a one-to-one correspondence between ξ_c and a, the results of N-body simulations show that there is an intrinsic scatter in the $\xi_c - a$ relationship (Navarro et al., 1996). This stochasticity will not significantly alter the results since these fluctuations are largely erased when one integrates over the ensemble of infalling clumps.

The details of the density profile for the clumps (e.g., Hernquist vs. NFW) should not significantly alter our results. As shown in Figure 4.4, the central profiles

have the same r^{-1} behavior, while the NFW profile falls off less rapidly at large r. However, it is the intermediate region, where the density is close to the background dark-matter density in the solar neighbourhood (the shaded region in Figure 4.4), that is of greatest interest. The central cores of the accreting clumps remain compact while the outer regions are quickly stripped by the tidal field of the Galaxy. Since the density fall-off is more gradual for the NFW model the resulting tidal streams would be longer, slightly increasing the probability that the solar system is in a low density stream today. Thus, the choice of a Hernquist profile should underestimate $dP/d\rho$ at low clump densities.

As described previously, the calculation of $dP/d\rho$ requires that we evaluate the quantity f_n in equation (4.4) for various clump parameters. An approximate form for f_n is found by assuming that the clump is unaffected by the tidal field of the Galaxy. In this limit,

$$f_n = \frac{H_0}{4\pi r_s^2 v_{r,n}} \frac{dV}{d\ln\rho} , \tag{4.36}$$

where $v_{r,n}$ is the radial velocity of the clump on its n^{th} pass through the solar neighbourhood (see Figure 4.3). The quantity $dV/d\rho$ is readily calculated from the clump density profile. The resulting expression for f_n can be compared directly with the measurement of f_n in the simulations (equation (4.4)), as we will see in the next section.

4.4 Numerical Simulations

We use numerical simulations to study the effects of tidal fields on clumps as they pass through the inner regions of the Galaxy. Clumps of various masses, initially described by the Hernquist spheres, are set on orbits such that a point particle with the same initial conditions would reach the solar radius today. The clumps are followed as they move through the rigid, time-dependent Galaxy potential described in Section 4.3.1. Each clump consists of 10^4 particles. The code used was a

modified version of the treecode made available by J. Barnes[1]. The time step Δt is dynamically adjusted (Pearce et al., 1994) using

$$\Delta t = \alpha \sqrt{\frac{\epsilon}{a_{\max}}}, \tag{4.37}$$

where ϵ is the softening length, $a_{\max}$ is the maximum acceleration that any particle has for that timestep, and $\alpha \sim 0.5$ is a fixed parameter adjusted to optimize the performance of the treecode. The softening length is taken to be 1/40th of the scale radius of the infalling halo. We have checked that the results do not change significantly when the number of particles is increased or the timestep reduced.

4.4.1 *Dynamical Friction*

We note that the effects of dynamical friction on the evolution of the clumps are not included in the code. Dynamical friction due to the motion of a clump through the Galactic halo would cause a steady deceleration of the clump in the direction of its motion, leading it to spiral into the centre of the Galaxy. These effects should be negligible for the problem at hand, since the timescale for dynamical friction is generally much longer than the age of the universe. For example, for a clump of mass $M \simeq 10^9 M_\odot$ travelling at speed $v_{\rm clump} = 500$ km s^{-1} through the halo, with a perigee of $r = 8.5$ kpc, the timescale for the clump to spiral into the Galactic centre is at least

$$t_{\rm fric} \simeq 2.5 \times 10^{10} \left(\frac{r}{8.5{\rm kpc}}\right)^2 \left(\frac{v_{\rm clump}}{500{\rm kms}^{-1}}\right)^2 \left(\frac{10^9 M_\odot}{M}\right) \text{ years} \tag{4.38}$$

(See for example Binney and Tremaine, 1987, Section 7.1). This is a conservative underestimate of the friction timescale because it assumes the clump spends all of its time at perigee and ignores the spatial extent of the clump. A clump more massive than this which penetrates the solar orbit could in principle suffer significant

[1] The original version of the treecode is avaiable from http://www.ifa.hawaii.edu/~barnes/treecode/treeguide.html

dynamical friction. However, even in this case, we expect the clump to be ripped apart by the halo tidal field before it is appreciably slowed by dynamical friction; as a result, the effective clump mass (as far as friction is concerned) is reduced, again rendering friction unimportant. To see this, a crude estimate of the ratio of the tidal and dynamical friction forces gives

$$\frac{F_{\rm fric}}{F_{\rm tidal}} \simeq 4 \times 10^{-3} \left(\frac{M}{10^9 M_\odot}\right)^{2/3} \left(\frac{500 {\rm kms}^{-1}}{v_{\rm clump}}\right)^2 \gamma^{1/3} \tag{4.39}$$

where γ is the ratio of the clump density to the local smooth halo density. Furthermore, if we were to include dynamical friction, it would cause more clumps to pass through the solar neighbourhood (on their way to the Galactic centre), increasing the probability that one would detect a clump.

4.5 Calculation of Local Densities

The density at any point $\mathbf{r}_i$ is approximated by taking the weighted average over its N nearest neighbors:

$$\rho(\mathbf{r}_i) \simeq \sum_{j=1}^{N} m_j W\left(\mathbf{r}_i, \mathbf{r}_j\right) \ , \tag{4.40}$$

where m_j is the mass of the j'th nearest particle, $W\left(\mathbf{r}_i, \mathbf{r}_j\right)$ is the symmetric smoothing kernel,

$$W(\mathbf{r}_i, \mathbf{r}_j) = \frac{1}{2V_i} \left(w(|\mathbf{r}_i - \mathbf{r}_j|/H_i) + w(|\mathbf{r}_i - \mathbf{r}_j|/H_j)\right) \ , \tag{4.41}$$

where $V_i \equiv 4\pi H_i^3/3$, H_i is half the distance to the $N^{\rm th}$ nearest neighbor to an observer at $\mathbf{r}_i$, and

$$w(x) = \begin{cases} 1 - \frac{3}{4}(2-x)x^2 & \text{if } x < 1 \\ \frac{1}{4}(2-x)^3 & \text{if } 1 \leq x < 2 \\ 0 & \text{otherwise} \end{cases} \tag{4.42}$$

This method is used extensively in smooth particle hydrodynamics simulations.

The quantity f_n is calculated by placing fictitious observers on a spherical shell of radius $r_s = 8.5$ kpc centered on the model Galaxy. At regular intervals throughout the simulation, these "observers" record their local density using the method described above. 10^4 observers are used in order to ensure that no significant stream or clump slips through the surface S undetected.

4.6 Results

A selection of representative dark matter-halos are merged with an analytic model of the Milky Way and their densities are measured by hypothetical "observers" located in a region representative of the solar neighbourhood. Specifically, the observers are situated on a sphere with a radius of 8.5 kpc – the distance of the Sun from the Galactic centre. The observers correspond to dark matter detectors in operation on the Earth.

Figure 4.5 provides snapshots of $10^9 M_\odot$ clumps that reach the solar neighbourhood today on their first, second, third and fourth orbits through the Galaxy. Figure 4.6 illustrates what the sphere of hypothetical observers see as a clump passes through the inner part of the Galaxy for the first time. There are two distinct regions of high measured density where the clump enters and exits the $r = r_s$ sphere. Thus, at this instant, a small fraction of observers measure a high density of high-velocity clump particles while most of the observers measure a relatively low density of clump particles.

By combining many simulated merger and observation events, it is possible to calculate the probability that any given observer would measure a dark matter density, ρ_{DM}, higher than ρ. Figure 4.7 shows that after integrating over all merging halos, it is very likely that there is a streaming component of dark matter in the solar neighbourhood due to the recent accretion events. Therefore, a few percent of the local dark matter is from a recent merger event and will have a streaming velocity

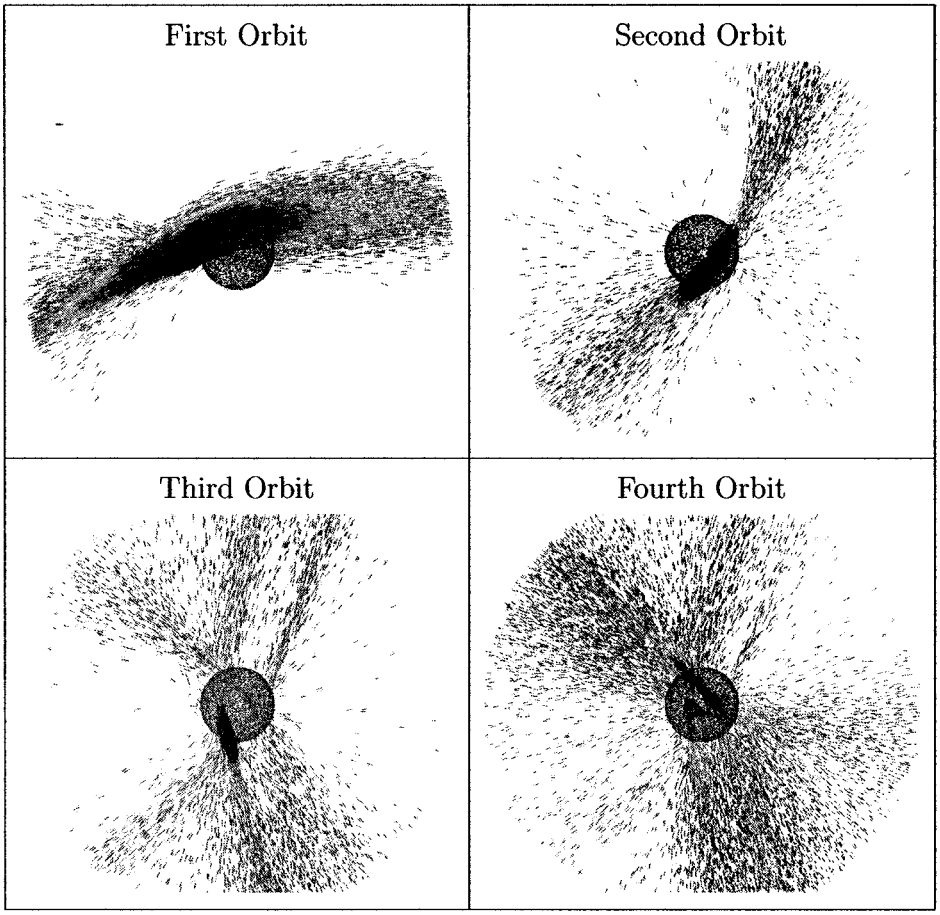

Figure 4.5: Snapshots of $10^9 M_\odot$ clumps whose centre of mass is near the surface S at $t = t_0$ on their first (upper left) through fourth (lower right) orbits through the Galaxy. The surface S is represented by the sphere in the centre of each panel. Darker regions correspond to higher densities. The symbols used for the particles are elongated in the direction of their velocity.

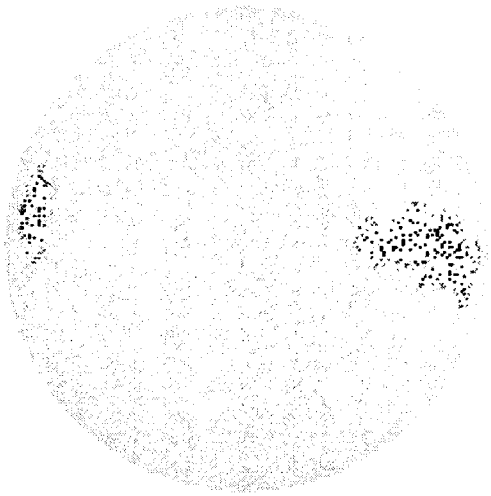

Figure 4.6: Sphere of observers and the density they measure as a stream passes through. Darker regions of the sphere correspond to higher measured densities.

significantly above the mean background speed. As indicated by the numerical simulations, the stream of particles had a mean speed of 569 km $s^{-1}$with a velocity dispersion of 25 km s^{-1}. Such a stream could have a significant effect on the dark matter spectra. A detailed study of the implications of velocity-space substructure will be conducted in Chapter 7.

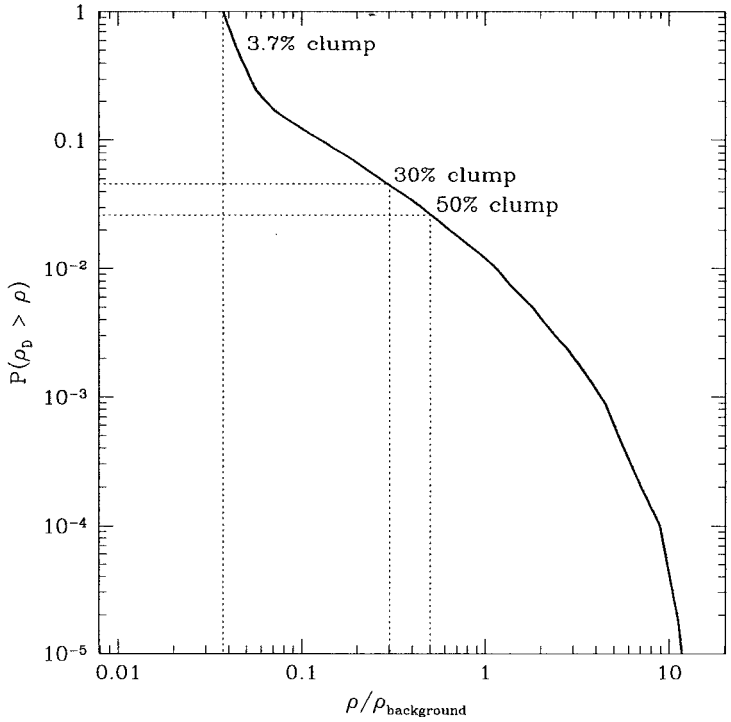

Figure 4.7: Probability for the Earth to be passing through a stream with local density greater than ρ. Since the probability goes towards unity at small densities, the local dark matter distribution has a low-density streaming component. ρ is given in units of the background density, $\rho_{bg} = 0.3$ GeVcm^{-3} $= 8 \times 10^{-3}$ $M_{\odot}$pc^{-3}.

5. "REVERSE-RUN" SIMULATIONS

The semi-analytic technique described in the previous chapter indicated that the local distribution of dark matter is not expected to be smooth. Streaming components from recent merger events could have a significant impact on the phase-space distribution of dark matter in the solar neighbourhood. However, the analytic techniques used to model the evolution of the Milky Way cannot fully match the complexity that arises in N-body simulations. Ultimately, one must resort to N-body simulations to fully understand the local distribution of dark matter. The question is then how to increase the velocity-space resolution while maintaining a small enough number of particles such that the simulation is still manageable. To accomplish this challenge, a novel numerical technique, based upon the reversibility of collisionless systems, is developed and tested. The theory behind the method is presented and demonstrated for a simple one-dimensional system. The algorithm is then applied to more complicated situations.

5.1 The Reverse-Run Technique

A system consisting of collisionless cold dark matter can be completely described by the time-dependent phase-space distribution function, $f(\vec{x}, \vec{v}, t)$. At time t, f can be regarded as either the phase-space density of particles at $(\vec{x}, \vec{v})$ or as a probability of finding a particle at that phase-space location. Regardless of the interpretation, as discussed in Chapter 3, the evolution of the distribution function is governed by

the collisionless Boltzmann equation and Poisson's equation.

$$\frac{\partial f}{\partial t} + \sum_{i=0}^{6} \frac{\partial w_i}{\partial t} \frac{\partial f}{\partial w_i} = 0 \tag{5.1}$$

$$\nabla^2 \Phi = 4\pi G M \int f(\vec{x}, \vec{v}) d^3 v \tag{5.2}$$

An important feature to note is that the potential does not depend on the velocity of the mass distribution, only on the positions. If an N-body simulation has an insufficient number of particles to accurately trace the velocity-space distribution in a given region, it may still be possible to accurately model the potential (or equivalently the density) of the system. For example, an accurate approximation of the density in the solar neighbourhood may be possible with only about 100 particles in the region around the Sun but this number is completely inadequate to accurately trace the velocity-space distribution in that region. In this numerical regime, a modest increase in velocity-space resolution can be achieved by simply adding numerous test particles to the initial particle distribution and evolving the system forward. The test particles would effectively interpolate the phase-space distribution between the massive DF tracers. The dynamics of the system is not changed with the addition of test particles, but the interpolation provides a more complete picture of the phase-space distribution of the system.

In the final output of the simulation, these test particles would be distributed throughout the simulation volume providing additional particles to map out velocity-space at *any* given position. However, when the simulations are to be used to model dark matter detection events where one is interested in the *local* velocity-space distribution, the increased resolution at a given point is modest at best since only a few test particles may be found in the volume. In order to obtain the highest velocity-space resolution, one would want *all* of the test particles to end up exactly at the point of interest. The situation could be improved by repeating the simulation several times and using the results from each preceeding simulation to refine the initial distribution of test particles so that more end up in the region of interest but

this technique has problems. In particular, the velocity-space features are limited to refinements of features detected in the first iteration only. For example, if a region of test particles in the initial simulation evolves into a low-density stream that intersects with the volume of interest, but the volume contains no particles from the stream (since it is such a low density in configuration space), the initial region of test particles would not be resampled at a higher resolution in the proceeding iterations. However, this stream could be very important in dark matter detection experiments since, by Liouville's Theorem, a low density in configuration-space must have a high density in velocity-space – i.e. the velocities are highly correlated. As illustrated in Section 1.5.2 and as will be explored in more detail in Chapter 7, such a stream could introduce significant features into the dark matter detection spectra.

A new technique to overcome these difficulties, to be used in conjunction with standard cosmological simulations, allows one to map the velocity-space distribution at a single point within a simulation. The method relies on test particles which, by design, reach the desired point (the position of the would-be detector) in the final timestep of the simulation. Through an iterative process, these test particles allow one to locate the points where the phase-space sheet describing the dark matter distribution intersects the phase space sheet describing the detector.

The starting point for our algorithm is a standard forward N-body simulation. In the final frame of the simulation an appropriate location for a detector is identified and a velocity-space spanning grid of massless test particles is placed at that location. Both the test particles and original simulation particles are then evolved backward in time to the initial frame of the simulation. The backward evolution is accomplished by simply reversing the timestep. During this "reverse run" the phase-space sheet defined by the test particles will fold and curl. At the initial time, the intersection points of the test-particle phase-space sheet and the phase-space sheet that defines the initial dark matter DF are located. These intersection points map directly into points in velocity space at the position of the detector (i.e. the initial

velocity-space distribution of the test particles). The value of the DF is calculated at each crossing point, and, by Liouville's Theorem, one can obtain the DF at the location of the detector.

The test particles provide an interpolation of the DF in the region of the detector. For the interpolation to make sense, the system must reverse properly. In essence, reversibility is equivalent to the condition that the dark matter DF, as described by the simulation particles, maintains its three-dimensional character. Chaos, driven in part by two-body interactions, combined with round-off errors, has the potential to spoil the reversibility of the time integration and destroy the integrity of the phase-space sheet. Therefore, as indicated in Chapter 3, the softening of the system should be approximately 1/4 of the initial grid spacing in periodic systems.

To obtain an estimate of the resolution of the method, one must first consider the velocity-space distribution that can be obtained from a traditional simulation. Consider a simulation with a dark matter halo of size L with a potential of depth Φ consisting of N particles. To obtain a picture of the velocity-space distribution about a given point x_o, a small volume, V', of width L' must be chosen about $\vec{x}_o$ and will contain N' particles and have a velocity dispersion of σ. Two competing factors contribute to the velocity-space resolution. The first is simply the number of particles in the volume. For a given V', the greater N', the better the resolution will be. The velocity dispersion is roughly a measure of volume in velocity space, so the velocity-space resolution, Δv, scales as

$$\frac{\Delta v}{\sigma} \sim N'^{-1/3} \tag{5.3}$$

However, the size of the volume V' itself acts to reduce velocity space resolution since one is averaging over the volume. The larger the volume, the more details will be lost due to the averaging procedure. If the potential varies by $\Delta\Phi$ across the sampled volume V', the velocity-space resolution can be estimated to be

$$\frac{\Delta v}{\sigma} \sim \frac{\Delta\Phi}{\Phi} \sim \frac{L'}{L} \sim \left(\frac{N'}{N}\right)^{1/3} \tag{5.4}$$

In order to balance these two effects, the volume V' should be chosen such that it contains $\sqrt{N}$ particles. In this case, the velocity resolution goes as $N^{1/6}$. Therefore, for traditional N-body simulations, the velocity-space resolution at a given point increases quite slowly as a function of the number of particles in the simulation. However, since one does not have to average over a small volume in the reverse-run technique, the method has a resolution in velocity space of $\Delta v/\sigma \sim N^{-1/3}$. Thus, with $N = 10^6$ particles and using the reverse-run technique, one can achieve a resolution that would have previously required 10^{12} particles!

5.2 One-Dimensional Simulations

To demonstrate this technique, it is useful to examine a much simpler scenario such as a one-dimensional simulation of planar gravity. These reduced simulations can be used to both illustrate and test the technique without the difficulties involved when dealing with the full six-dimensional phase-space distribution.

5.2.1 Planar Symmetry

The acceleration due to gravity when planar symmetry is imposed can easily be derived from Poisson's equation.

$$\nabla^2\Phi = 4\pi G\rho \tag{5.5}$$

With planar symmetry, there can be no y or z dependence. Therefore, if a thin plane with mass m is located at x_0

$$\frac{d^2\Phi}{dx^2} = 4\pi G m\delta(x - x_0) \tag{5.6}$$

In order to solve this equation, it is useful to replace the delta function with one of its limit definitions.

$$\delta(x - x_0) = \frac{1}{\pi}\lim_{\epsilon\to 0}\frac{\epsilon}{\epsilon^2 + (x - x_0)^2} \tag{5.7}$$

Therefore,

$$\frac{d^2\Phi}{dx^2} = 4Gm \lim_{\epsilon \to 0} \frac{\epsilon}{\epsilon^2 + (x - x_0)^2} \tag{5.8}$$

To solve for the acceleration, $a = -d\Phi/dx$, integrate and take the limit.

$$\begin{aligned} a &= -4Gm \lim_{\epsilon \to 0} \int \frac{\epsilon}{\epsilon^2 + (x - x_0)^2} dx \\ &= -4Gm \lim_{\epsilon \to 0} \tan^{-1}\left(\frac{x - x_0}{\epsilon}\right) \\ &= -2\pi Gm \frac{x - x_0}{|x - x_0|} \end{aligned} \tag{5.9}$$

Therefore, the magnitude of the acceleration is constant while the direction only depends upon which side of x_0 a particle is on. For multiple planes, the net acceleration is simply the sum of the acceleration due to each one individually:

$$a(x) = -2\pi G \sum_i m_i \frac{x - x_i}{|x - x_i|} \tag{5.10}$$

Effectively, this means the acceleration is simply the difference between the mass to the right of x and the mass to the left.

5.2.2 Periodic Boundry Conditions

Cosmological simulations require the implementation of periodic boundary conditions and expanding, comoving coordinates. The basic requirement is that particles in a uniform distribution experience no net force. Consider a simulation box of comoving size L, extending from $-L/2$ to $L/2$ with a total mass of M. In the non-periodic case with a uniform mass distribution, a particle at x (where $-L/2 \leq x < L/2$), experiences a net acceleration of

$$a = -4\pi GM \frac{x}{L} \tag{5.11}$$

Therefore, when periodic boundary conditions are applied, the net acceleration of a particle at x must be

$$a(x) = 2\pi G \left(2M \frac{x}{L} - \sum_i m_i \frac{x - x_i}{|x - x_i|}\right) \tag{5.12}$$

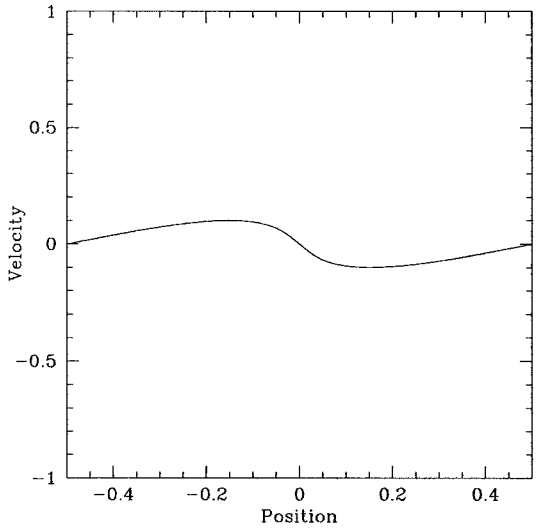

Figure 5.1: The initial phase-space distribution of the massive particles. Positions and velocities are in arbitrary units.

An alternate derivation of the periodic potential and accleration can be done using Fourier transforms to yield the same result.

5.2.3 Phase-Space Structure

For planar symmetry, the dimensionality of phase-space is simply two. The initial phase-space distribution of the massive particles in this case is just a line (Figure 5.1). This distribution started from a cold ($v = 0$), uniform density line of particles which had a sinusoidal perturbation applied. As the system evolves, the particles remain bound to a manifold of the same dimensionality as that defined by the initial conditions. In other words, since the particles started in a one-dimensional line, they must remain in a one-dimensional line. However, the accuracy with which the line of particles can be followed depends upon the number of particles used to trace it. For example, Figure 5.2 shows the final state of the initial conditions shown in Figure 5.1 using 100 particles (left) and 100 000 particles (right). In the high-resolution simulation, the line of particles can clearly be traced even through

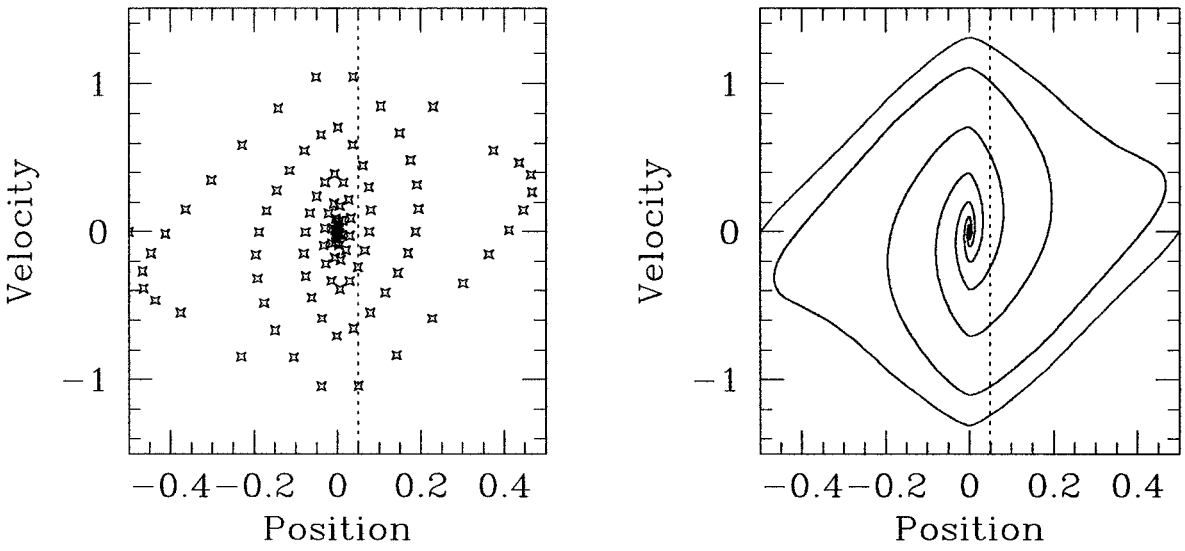

Figure 5.2: The final phase-space distribution of the massive particles. Left: 100 particles. Right: 10^5 particles

the tight windings near $x = 0$. In the low-resolution simulation, the line nature is not clearly visible though if it is known that it should be a line, a reasonable approximation can be intuitively interpolated. However, simply joining consecutive particles with a straight line segment would imply that in some cases the phase-space line could self-intersect and yields a completely false description of the nature of the distribution.

Therefore, the only way one can obtain a measure of the velocity-space distribution is to directly sample the distribution of particles in the simulation. In a one-dimensional simulation, this involves looking at the particles in a slice of width Δx about the location of interest, x_0. The simplest way to analyze the velocity distribution is to construct a velocity histogram of all the particles in the slice. However, to avoid issues related to the size of the bin used, a cumulative velocity distribution can be used instead. In order to obtain enough particles in the slice so that statistical fluctuations are minimized, the width should be chosen so that in a simulation containing N particles, roughly $\sqrt{N}$ particles reside within $x_0 \pm \Delta x/2$. Figure 5.3

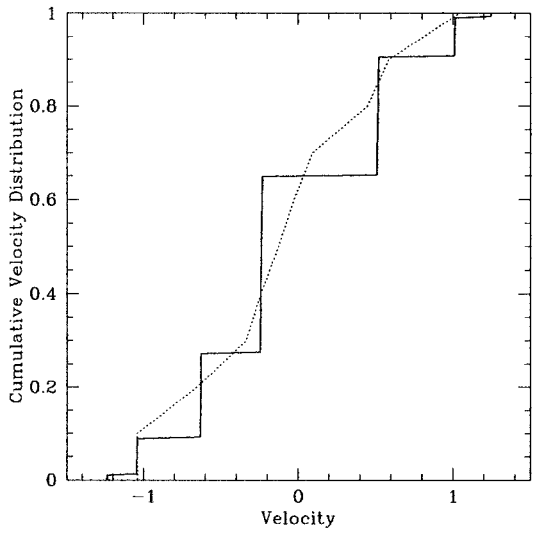

Figure 5.3: The cumulative velocity-space distribution at $x_0 = 0.05$ from the low-N (dotted) and high-N (solid) simulations. The low-N distribution tends to (incorrectly) imply a smooth, continuous velocity-space distribution. The high-N results correctly identify the 7 distinct velocity-space streams.

shows the cumulative velocity distribution at $x_0 = 0.05$ obtained from the low and high resolution simulations of Figure 5.2. The velocity distribution from the high resolution simulation clearly shows the location of the 7 streams at x_0. However, the low resolution results are completely washed out. Due to the relatively large width of the slice that was required, particles from adjacent streams are incorrectly counted in the distribution. If a more narrow slice is used instead, the blending of multiple streams can be reduced but some low-density streams could be missed completely. The reverse-run technique provides a means to obtain high-resolution velocity distributions using only the low-resolution simulation results.

The first step in the reverse-run technique is to add a uniform distribution of test particles at the location of interest which span the velocity-space. For the 1-D simulations examined above, this is simply a line of test particles extending from $v = -1.5$ to $v = 1.5$ at $x = 0.05$. Typically, the number of test particles is chosen

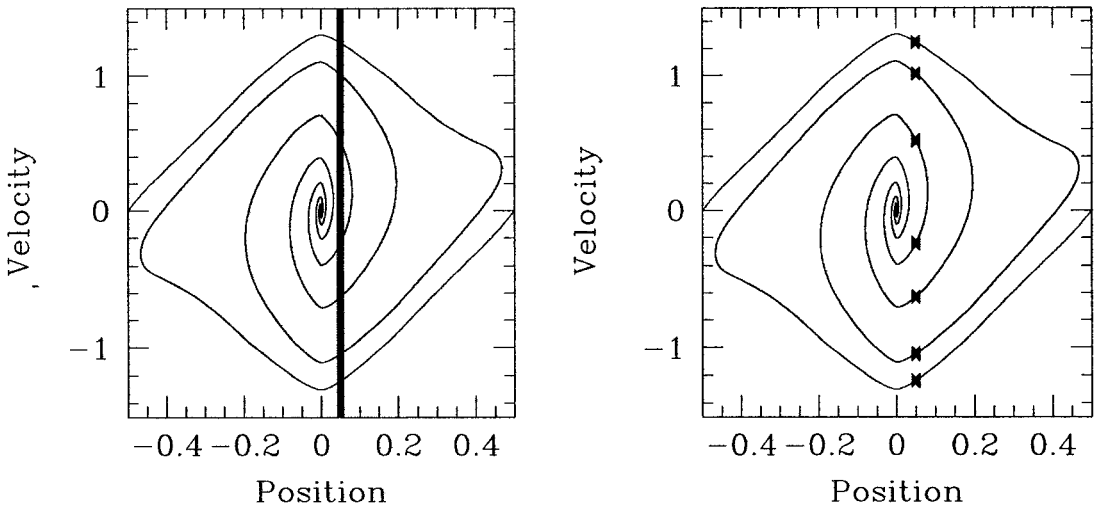

Figure 5.4: The initial distribution of test particles (thick line) and the high resolution simulation (thin line) in the first reverse-run iteration (left panel) and for the fifth iteration (right panel). Note how the test particles are now tightly clustered on the real-particle distribution.

to equal the number of massive particles in the simulation. Figure 5.4 shows the initial distribution of test particles for both the low and high resolution simulations. Once the test particles are distributed, the entire system is evolved backwards by simply reversing the time step. If, as discussed in Chapter 3, the phase-space sheet of the massive particles was properly maintained, the real particles will evolve back to their initial location. Figure 5.5 shows the state of the system after it has evolved back to $t = 0$ and the initial perturbation is removed. The points of interest are where the line of test particles crosses the unperturbed massive particles at $v = 0$. In 1-D, this can easily be determined by finding the locations in the line of test particles where the velocity switches sign.

The accuracy with which the crossing point can be determined depends upon the resolution of the test-particle distribution. The initial distribution of test particles covers a large span of velocity space and many of them do not end up anywhere

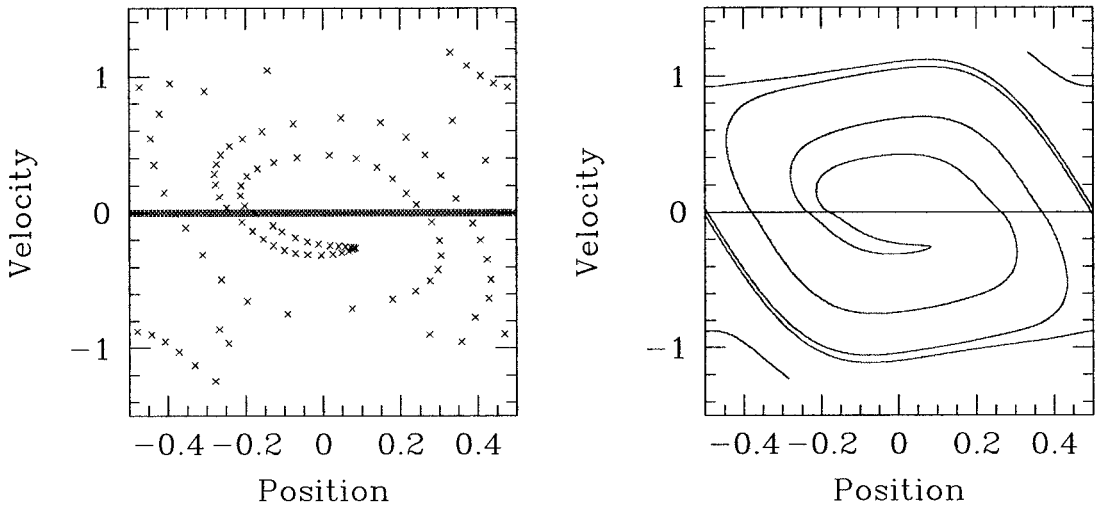

Figure 5.5: The final ($t = 0$) phase-space diagram after the test particles in the low resolution (left panel) and high resolution (right panel) simulations have been evolved backwards. Note the 7 intersections between the initial phase-space sheet and the phase-space sheet of the reversed test particles.

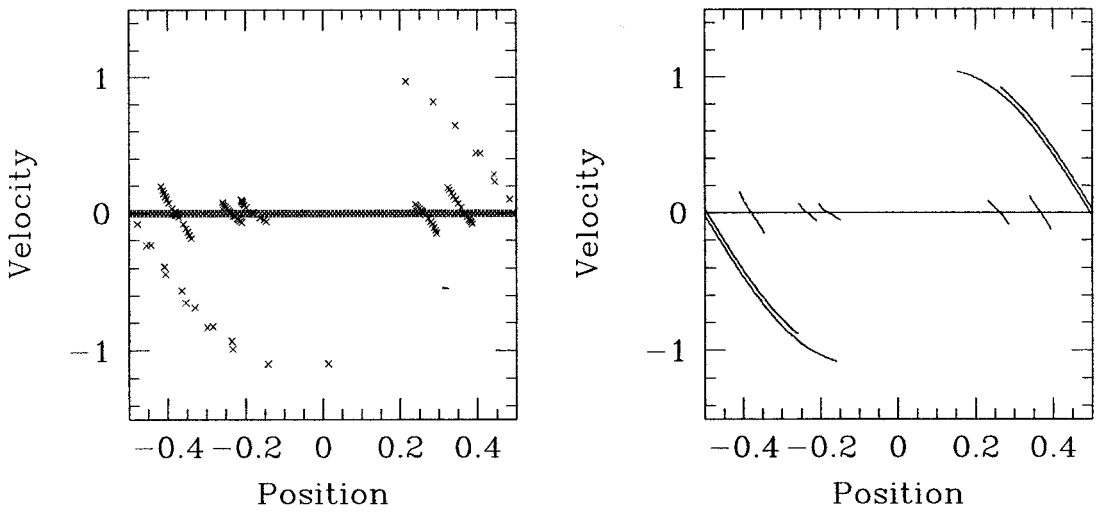

Figure 5.6: The same as Figure 5.5 but after 5 reverse-run iterations.

near a crossing point. The accuracy can be improved by iterating the reverse-run procedure several times. The location of the crossing points determined from the first reverse run can be used as centres for distributing the same number of test particles, but at a high resolution. This causes the test particles to end up closer to the initial phase-space distribution by discarding regions which end up far from it. Each successive iteration can use the previous iteration's results to improve the initial distribution of test particles. This can yield more accurate positions for the crossing points. The right-hand panel of Figure 5.4 shows the initial test-particle distribution at the beginning of the fifth iteration. The test particles are clustered about the true DF. Figure 5.6 shows the distribution of particles at the end of the fifth iteration. Note how the test particles are clustered close to the initial DF allowing for an accurate determination of the crossing points.

While the location of the crossing points, or equivalently the velocities of particle streams at $x = 0.05$ in the final frame, are important, there is no information about the relative density of each stream. This is of critical importance for dark-matter experiments since detection rates depend directly upon the density of particles. The

density of the DF in the final frame corresponding to each of the crossing points can be estimated using Liouville's Theorem which states that the comoving phase-space density is constant. Therefore,

$$\left(\frac{\rho}{\sigma}\right)_{t_1} = \left(\frac{\rho}{\sigma}\right)_{t_2} \tag{5.13}$$

where ρ is the density, and σ is the velocity dispersion of the particles. Hence, $\rho_{t_2} \propto \sigma_{t_1}^{-1}$. If t_1 is the initial time of the forward simulation, and t_2 is the final time, the final density can be determined by measuring the initial velocity dispersion. The velocity dispersion is proportional to the particle density in velocity space, or for a fixed number of particles the velocity-space volume V, so

$$\rho_{t_2} \propto V_{t_1}^{-1} \tag{5.14}$$

This relationship applies to both massive and test particles. Therefore, if one measures the volume defined by test particles surrounding the crossing point, one can approximate the density of the corresponding stream in the final state of the simulation. In 1-D, the "volume" is simply the distance between the particles spanning the crossing point. Figure 5.7 shows the cumulative velocity distribution from the low-N reverse-run after 5 iterations. As is apparent in the Figure, the velocities of the streams are accurately determined but there is some drift in the relative densities of the streams. This is primarily due to an overestimate of the density of the stream near $v = -1$. This stream is considerably more dense than from the direct high resolution simulations, which, due to the use of the normalized cumulative velocity distribution, shifts the other streams up and reduces their apparent density. Additionally, the low-resolution system will evolve slightly differently from the high-resolution system simply due to the different number of particles and slightly different densities may be expected. Nonetheless, the results are a very significant improvement over the information which can be obtained directly from a low resolution simulation. The general trends are quite accurate with outer low-density, high velocity streams and higher density, lower velocity streams towards the centre.

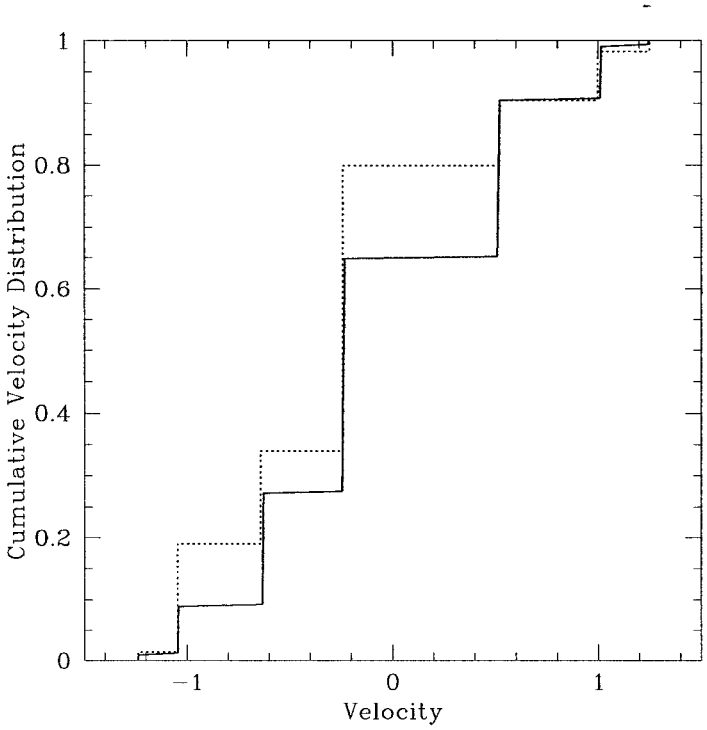

Figure 5.7: The cumulative velocity-space distribution at $x_0 = 0.05$ from the low resolution reverse-run (dotted) and high-N (solid) forward simulations. The 7 streams are successfully identified using the reverse-run technique with approximately the correct densities.

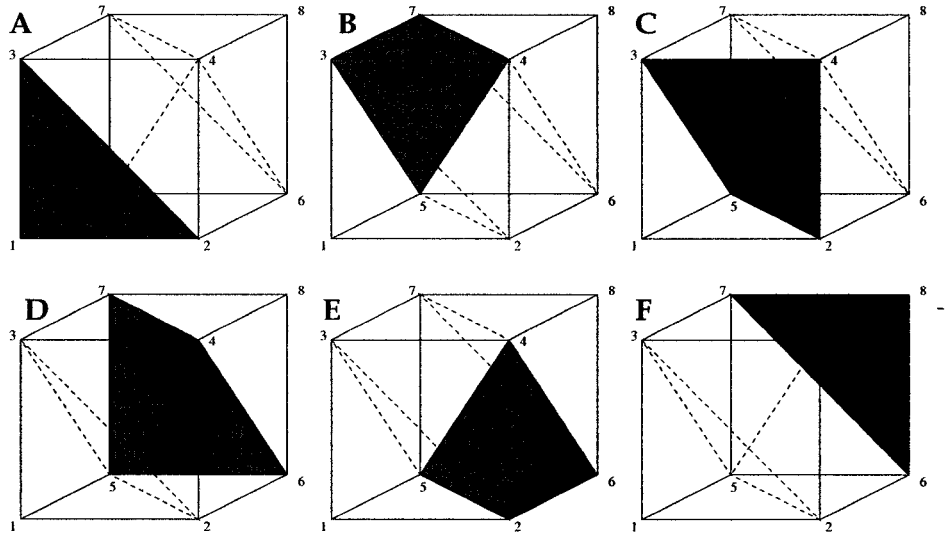

Figure 5.8: A cube can be divided into 6 non-overlapping tetrahedra.

5.3 3-Dimensional Simulations

While the simple 1-dimensional simulations clearly illustrate the theory and the potential of the technique, it must be verified that it is practical to implement in 3-dimensions. A simple test case in 3-dimensions is a "cosmological" spherical cold collapse model. A more realistic model investigated in Section 5.5 involves adding perturbations to the spherical distribution so that the system will involve in a hierarchical manner. The majority of the procedure can be conducted in exactly the same manner as in the one-dimensional case except that it is extended to the higher number of dimensions. For example, when adding the test particles to the final frame of the simulation, they are uniformly distributed throughout the velocity-space volume rather than simply in a line. However, while it is trivial to determine the intersection of the initial phase-space sheet of the massive particles and the test particles in one dimension, in 3-dimensions it is not quite so obvious.

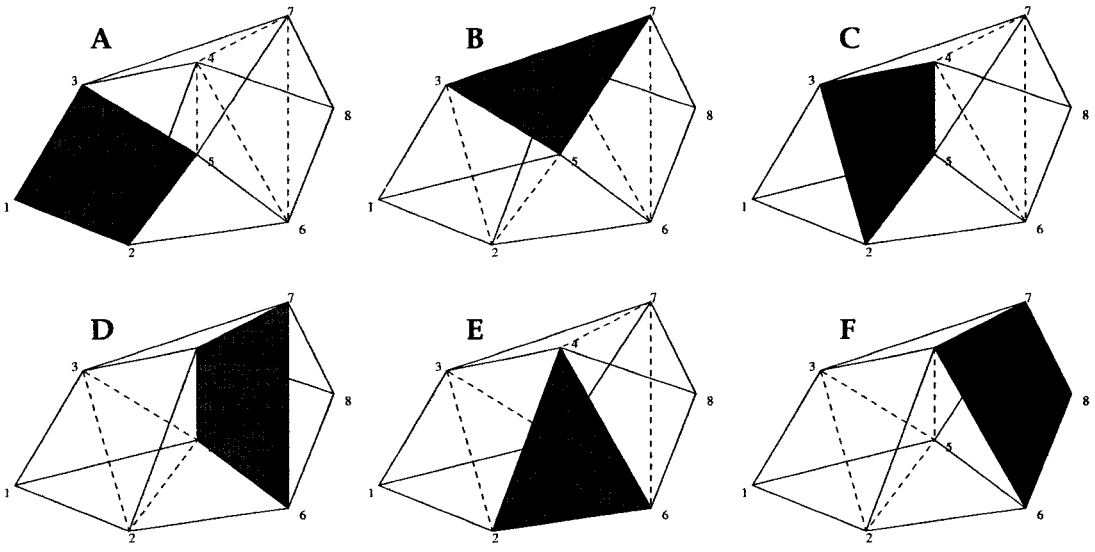

Figure 5.9: As the cube is distorted, the 6 tetrahedra still fill the volume.

5.3.1 *Calculation of Intersection Points*

In the one-dimensional models, the phase-space sheet of the initial distribution and the test particles are simple lines in two-dimensional phase-space. Two adjacent test particles could simply be connected with a straight line to see if the test particle sheet would intersect with the sheet of massive particles. In a full 3-dimensional simulation, the subspaces of interest are now two 3-dimensional "sheets" intersecting in 6-dimensional phase-space. It is no longer trivial to determine the set of points where the sheets overlap. Fortunately, in most cases the initial distribution function after the perturbations are removed is very simple. For example, in a spherical model to be investigated later,

$$f(\vec{x},\vec{v}) = \Theta(r_{\max} - |\vec{x}|)\delta(\vec{v}) \tag{5.15}$$

where $\Theta(x)$ is the Heaviside function, $r_{\max}$ is the maximum extent of the DF and $\vec{v}$ is the peculiar velocity. Since the position and velocity dependence are separable, each subspace can be treated independently.

The clue to identifying the points of intersection is to note that since the initial

distribution of the test particles is a uniform grid degenerate in position, a set of adjacent test particles define a cube in velocity space. This cube can be decomposed into 6 tetrahedra which completely fill the volume as shown in Figure 5.8. As the test particles evolve backward through the potential, the tetrahedra will become distorted but continue to fill the volume. (Though it is possible that the tetrahedra may not exactly fill the volume of the distorted cube (Bagemihl, 1948), when the adjoining cubes are considered, no regions will be missed.) At the inital frame, there are two tests that must be performed to determine if a given tetrahedron of test particles intersects with the initial distribution function. The first is to verify that the position of a tetrahedron overlaps with the configuration-space distribution of the particles. A simple test checks that at least one vertex at $\vec{x}$, lies within $|\vec{x}| < r_{\max}$ or that the midpoint of the tetrahedron is close to the real distribution function. The second test is to see if $\vec{v} = \vec{0}$ lies within the velocity-space spanned by the tetrahedron.

To test if a point lies inside a tetrahedron, one needs to see if the point of interest and each of the vertices lie on the same side of the plane defined by the three other vertices. For example, if the vertices of a tetrahedron are at $\vec{a}$, $\vec{b}$, $\vec{c}$, and $\vec{d}$, and the point of interest is $\vec{x}$, then if $\vec{x}$ and $\vec{d}$ are on the same side of the plane which contains $\vec{a}$, $\vec{b}$, and $\vec{c}$, then the point *could* be inside. If it is true for each vertex, then the point lies inside the tetrahedron. This can be tested by checking that the components of the vectors between the plane and $\vec{x}$ and between the plane $\vec{d}$ are in the same direction. Explicitly,

$$\text{sign}\left[\left(\left(\vec{b}-\vec{a}\right)\times\left(\vec{c}-\vec{a}\right)\right)\cdot\left(\vec{d}-\vec{a}\right)\right] = \text{sign}\left[\left(\left(\vec{b}-\vec{a}\right)\times\left(\vec{c}-\vec{a}\right)\right)\cdot\left(\vec{x}-\vec{a}\right)\right] \quad (5.16)$$

Figure 5.10 illustrates this test. Both $\vec{d}$ and $\vec{x}$ are on the same side of the plane defined by $\vec{a}, \vec{b}$, and $\vec{c}$, so both $\vec{x}-\vec{a}$ and $\vec{d}-\vec{a}$ will have a component parallel to $\vec{n} = \left(\vec{b}-\vec{a}\right)\times\left(\vec{c}-\vec{a}\right)$. On the other hand, $\vec{y}$ lies on the opposite side of the plane so it will have a component anti-parallel to $\vec{n}$. This can be rewritten as

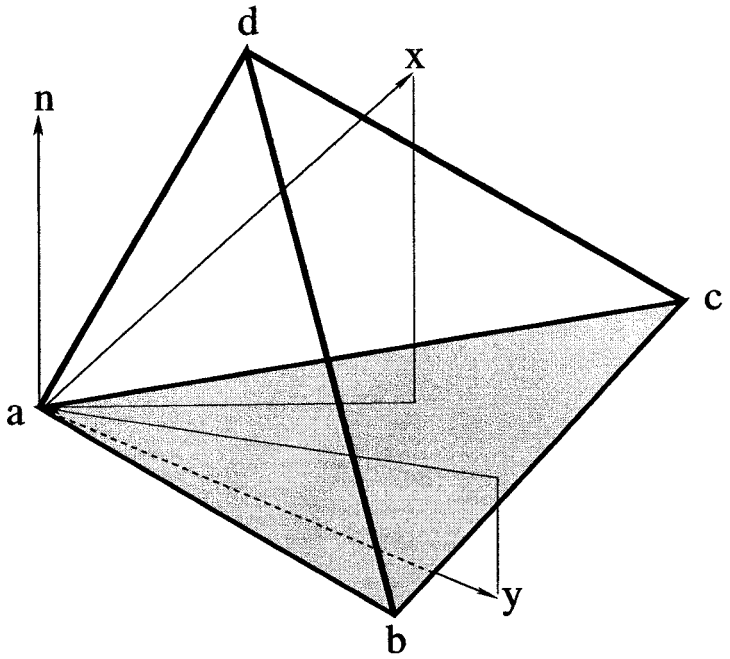

Figure 5.10: Tetrahedron test to see if a point and one vertex are on the same side of the plane defined by the 3 other vertices.

$$\text{sign}\begin{vmatrix} a_x & a_y & a_z & 1 \\ b_x & b_y & b_z & 1 \\ c_x & c_y & c_z & 1 \\ d_x & d_y & d_z & 1 \end{vmatrix} = \text{sign}\begin{vmatrix} a_x & a_y & a_z & 1 \\ b_x & b_y & b_z & 1 \\ c_x & c_y & c_z & 1 \\ x_x & x_y & x_z & 1 \end{vmatrix} \tag{5.17}$$

This can be repeated for each vertex.

$$D_0 = \begin{vmatrix} a_x & a_y & a_z & 1 \\ b_x & b_y & b_z & 1 \\ c_x & c_y & c_z & 1 \\ d_x & d_y & d_z & 1 \end{vmatrix} \tag{5.18}$$

$$D_1 = \begin{vmatrix} x_x & x_y & x_z & 1 \\ b_x & b_y & b_z & 1 \\ c_x & c_y & c_z & 1 \\ d_x & d_y & d_z & 1 \end{vmatrix} \tag{5.19}$$

$$D_2 = \begin{vmatrix} a_x & a_y & a_z & 1 \\ x_x & x_y & x_z & 1 \\ c_x & c_y & c_z & 1 \\ d_x & d_y & d_z & 1 \end{vmatrix} \tag{5.20}$$

$$D_3 = \begin{vmatrix} a_x & a_y & a_z & 1 \\ b_x & b_y & b_z & 1 \\ x_x & x_y & x_z & 1 \\ d_x & d_y & d_z & 1 \end{vmatrix} \tag{5.21}$$

$$D_4 = \begin{vmatrix} a_x & a_y & a_z & 1 \\ b_x & b_y & b_z & 1 \\ c_x & c_y & c_z & 1 \\ x_x & x_y & x_z & 1 \end{vmatrix} \tag{5.22}$$

Therefore, if point $\vec{x}$ lies inside the tetrahedron then D_0, D_1, D_2, D_3, and D_4 will all have the same sign. It can also be shown that the volume of the tetrahedron is $V = D_0/6$ which is required to calculate the density of any streams.

5.4 Spherical Cold Collapse

Since the eventual goal is to apply the reverse-run technique to a simulation of the formation of the Milky Way, it is useful to consider a simple model in a cosmological context. Therefore, one can consider a spherical overdensity surrounded by a uniform universe. Fortunately, it can be shown that the region inside the overdensity will evolve independent of the region outside so that one can simply consider the isolated sphere (Peebles, 1982). Ryden and Gunn (1987) developed a reasonable model for the density profiles inside a spherical overdensity which collapses to form galaxies and clusters. Their density profile, and the corresponding mass profile at $z = 44$ are shown in Figure 5.11. At large r, the density profile flattens and the mass profile approaches r^3 as the overdense region merges with the outside density

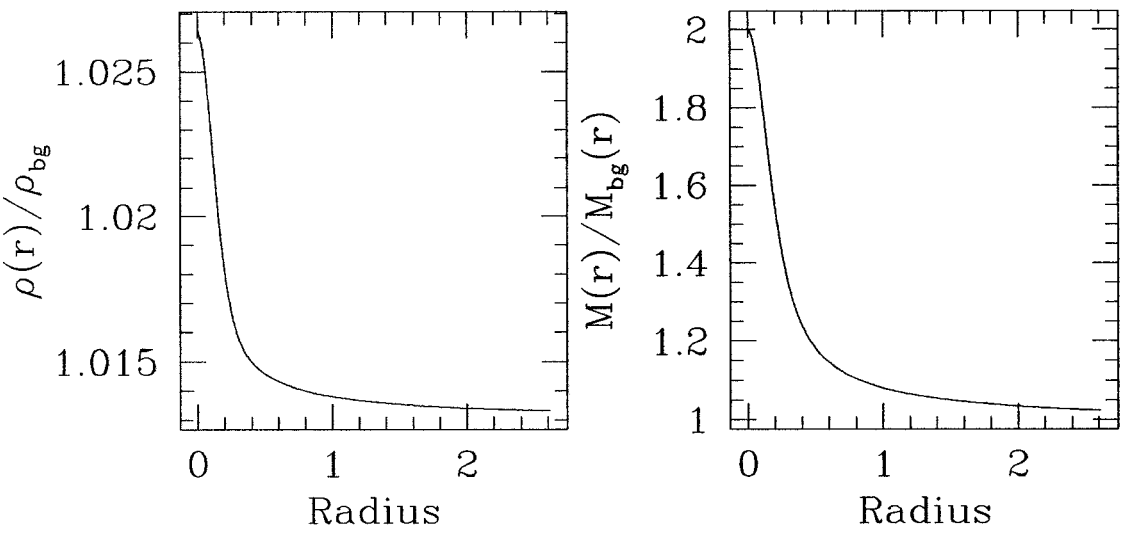

Figure 5.11: Initial density profile (left) and mass profile (right) of the spherical density perturbation compared to the background density at $z = 44$. As large r, both the density and mass profiles approach the background values.

distribution. Since a cosmological-style simulation is being performed, the initial distribution of particles are also given Hubble velocities.

5.4.1 Forward-Run Simulation

The first step in the reverse-run technique is to do a traditional forward simulation. The simulation is run from $t = 0$ to $t = 12$ (in units with $M_{\text{total}} = 100$ and $G = 1$) with approximately 33,000 particles and uses the same N-body code that will be used in subsequent, more realistic simulations. The initial and final phase-space distribution are shown in Figure 5.12. Note that the figure shows a two-dimensional projection of the full six-dimensional phase-space distribution. As a result, the appearance of the streams is greatly enhanced due to the favourable symmetry. If one considers a point at $r = 2$, there are clearly 11 streams. Since the system is spherically symmetric, any position in the system with the same radius should have the same number of streams. However, if one examines the full six-dimensional

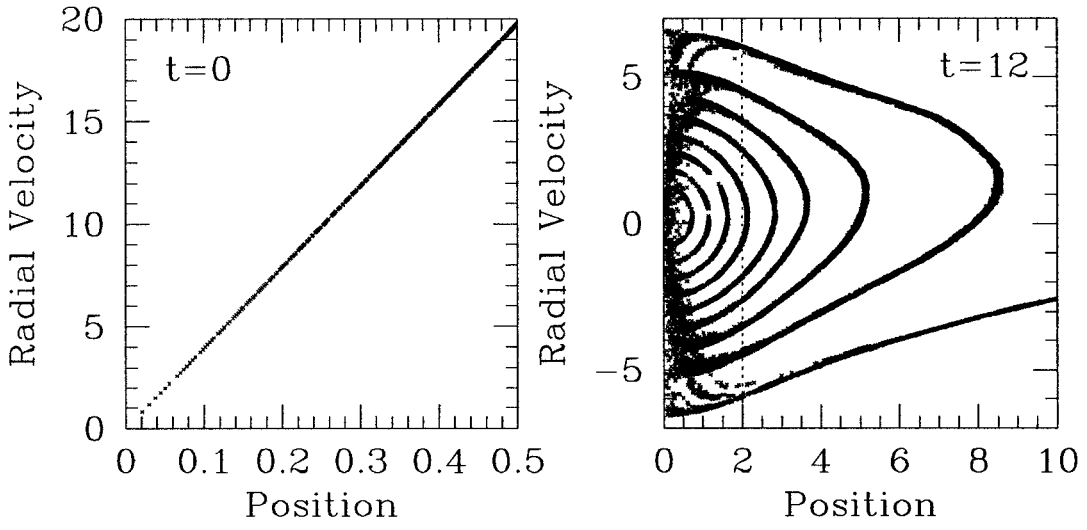

Figure 5.12: The initial phase-space distribution (left) and the final distribution (right) of a spherical collapse simulation with initial Hubble velocities. The vertical line at $r = 2$ indicates the location of interest at $t = 12$.

distribution at a given point with the same radius, i.e. $\vec{x}_0 = (2, 0, 0)$, a significantly different picture is obtained. As discussed with respect to the one-dimensional simulations in Section 5.2.3, the volume/resolution trade-off comes into effect. If a small volume is chosen (left panel in Figure 5.13), streams are completely missed. If a larger volume is chosen (right panel in Figure 5.13), the streams are largely washed out.

5.4.2 Reverse-Run Results

The next step in the reverse-run procedure is to populate the point of interest in the final forward-run output with test particles which span the velocity-space of the system. After evolving the system backwards, the intersections between the initial massive particle DF and that of the test particles can be determined. The velocity-space volume of the tetrahedron which contains $\vec{v} = (0, 0, 0)$ can be used to estimate the density of the stream in the final frame. Figure 5.14 shows the radial

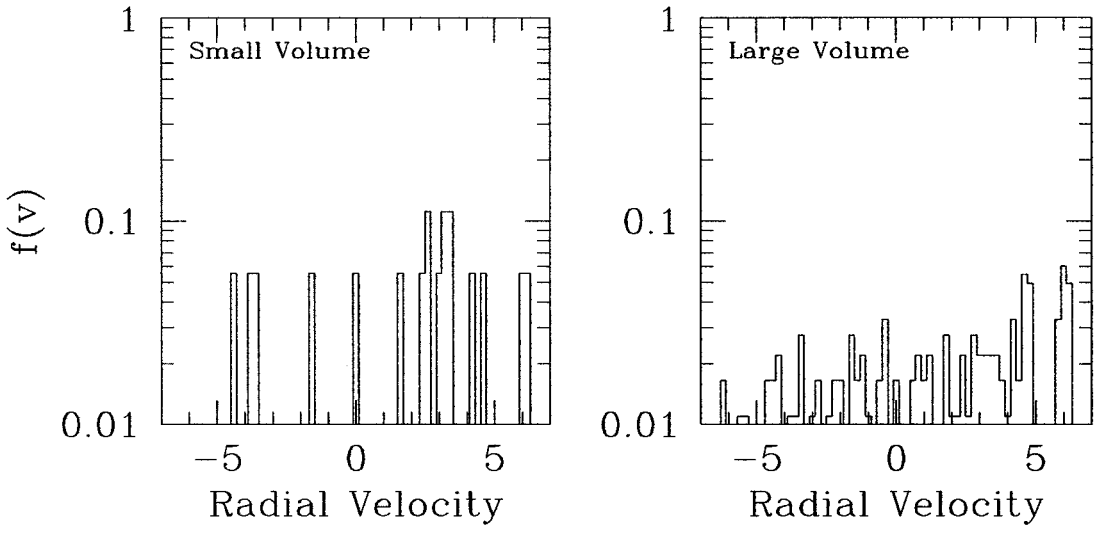

Figure 5.13: The radial velocity distribution at x_0 using a small volume with 45 particles (left) and a larger volume with 189 particles (right).

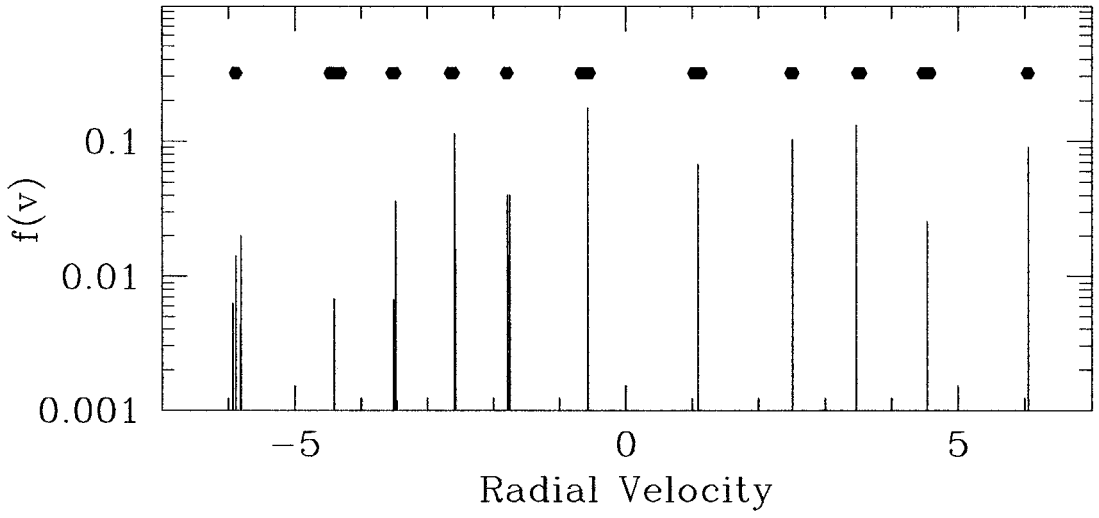

Figure 5.14: The radial velocity distribution at x_0 after 5 iterations. For comparison, the locations of the streams determined using spherical symmetry are indicated by the dots at the top of the figure.

velocity distribution after 5 iterations. The resolution with which the streams are determined is far superior to any measurements that could be obtained simply from the forward run even when spherical symmetry is used to enhance the results as indicated by the dots in the top of each panel. The width of the dots corresponds to the actual range of velocities that were found when looking at $r_0 \pm \Delta r/2$ with $\Delta r = 0.005$. Even with the advantage of symmetry, smaller values of Δr miss the low-density streams entirely.

The successful identification of the streams from the full 3-dimensional spherical collapse simulations indicate that the reverse-run technique can successfully be extended beyond rather trivial 1-dimensional toy models.

5.5 Spherical Collapse with Perturbations

To test the technique in a more realistic simulation, a spectrum of perturbations can be added to the spherical collapse model from the previous section. The detailed nature and origin of the perturbations will be discussed in Chapter 6 but for the moment it is sufficient to state that the spectrum of perturbations is chosen to be consistent with bottom-up hierarchical formation scenarios. This style of simulation was originally performed by Katz and Gunn (1991) to model the effects of gas dynamics on galaxy formation, but it can be applied to purely collisionless simulations as well. It has also been applied by Dubinski and Carlberg (1991) to investigate the structure of dark matter halos.

5.5.1 Forward-Run Simulation

The forward simulation was conducted in the same manner as the purely spherical collapse in the previous section. The perturbations applied can be seen in the density fluctuations in the initial conditions of the simulation (left panel of Figure 5.15). The final state of the system is shown in the right panel of Figure 5.15. The point of interest (as indicated by the arrow and green dot in the Figure) was

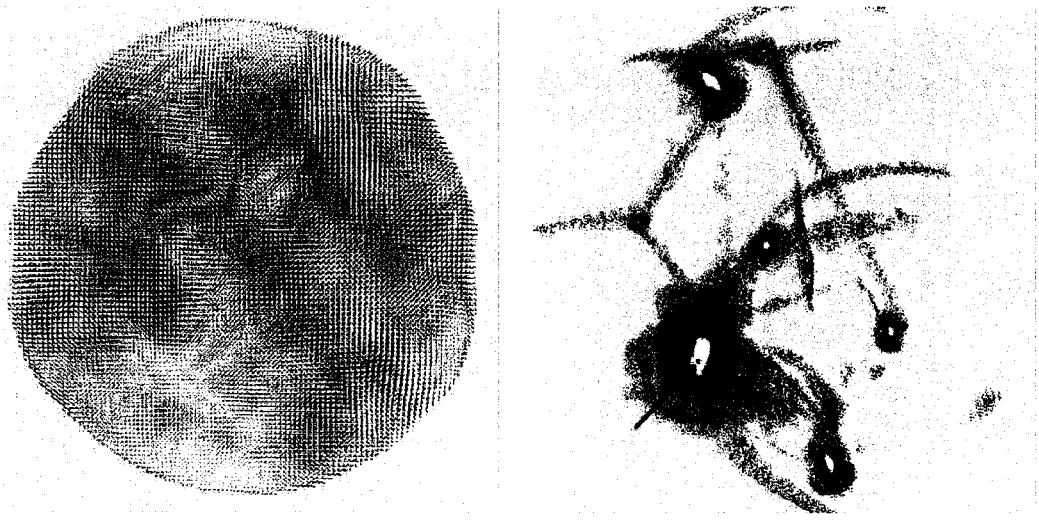

Figure 5.15: The initial conditions (left) and the final state (right) of a spherical collapse model with perturbations. The colour represents the density ranging from low-density (blue) to high-density (yellow), though the absolute densities vary significantly between each panel. The arrow in the right panel indicates the point of interest in the simulation.

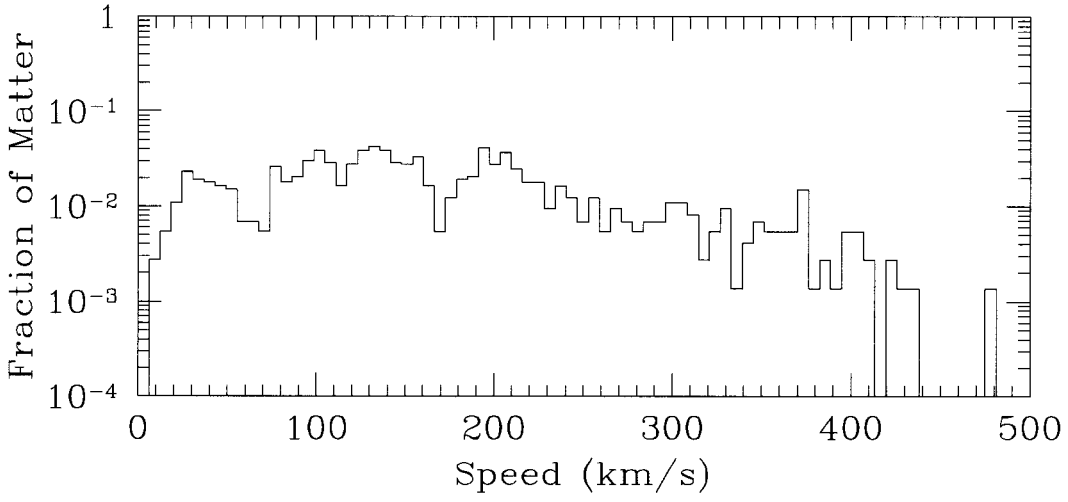

Figure 5.16: The speed distribution at x_0 obtained from the forward run using the nearest $\sqrt{N} \sim 700$ particles.

chosen to lie at approximately one softening length from the centre of the largest galaxy in the simulation. The galaxy chosen qualitatively resembles the dark matter distribution of the Milky Way with a mass of $5 \times 10^{12} M_{\odot}$ and virial radius of 500 kpc, roughly twice the size of the actual Milky Way. Figure 5.16 shows the speed distribution (with respect to the global rest frame) of dark matter measured using the 700 particles nearest to the point of interest. Note that the vertical axis is logarithmic. The speed distribution appears quite smooth, in agreement with what other studies have found (Moore et al., 2001; Helmi et al., 2003). However, this effect is primarily due to the finite resolution and large volume required to obtain a reasonable number of particles. Applying the reverse-run technique yields a significantly different picture.

5.5.2 *Reverse-Run Results*

The reverse-run technique avoids the problems associated with averaging over large volumes of space to obtain velocity-space information. By placing the test particles at the point of interest, and evolving the system backwards, a significant increase in velocity-space resolution can be obtained. Figure 5.17 shows the speed distribution obtained from the reverse-run algorithm after 10 iterations. Increasing the number of iterations beyond 10 does not significantly alter the results. Instead of an almost smooth distribution of speeds, the velocity-space spectrum is dominated by a couple of specific speeds. In order to determine if the particles with these speeds are correlated (ie: the particles belong to distinct streams arriving from a specific direction) or are more uniformly distributed (i.e: a smooth, uniform infall into the Galaxy from all directions), one can look at the orientation of the dark matter particles with respect to the mean bulk velocity in the region. Figure 5.18 shows the correlation between the direction of the dark matter particles and the speed of each particle. The particles are not uniformly distributed in angle indicating that the dark matter particles are arriving from preferred directions.

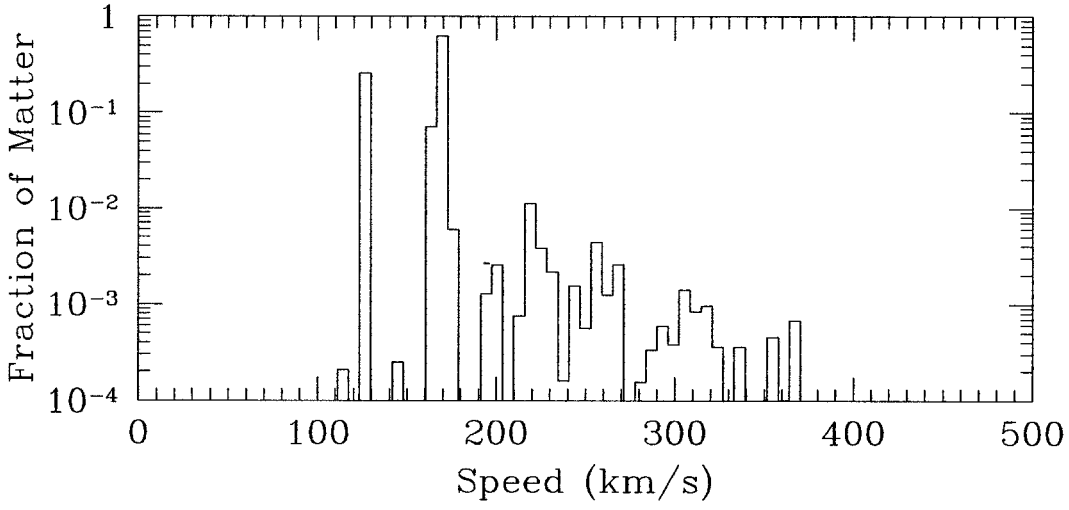

Figure 5.17: The speed distribution at the point of interest obtained from the reverse-run technique.

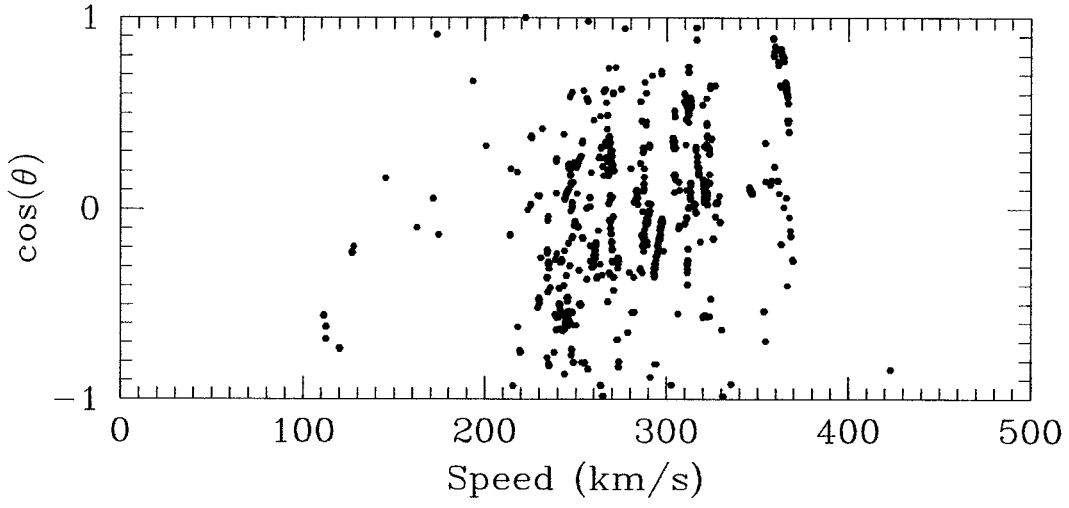

Figure 5.18: The speed of dark matter particles versus the angle between each particle's velocity and the bulk motion of the forward simulation. The dark matter streams are not smoothly distributed in angle and speed, and therefore are preferentially arriving from specific directions.

While this spherical collapse model with perturbations more closely resembles the formation of a system which is qualitatively similar to the Milky Way within the Local Group, in order to develop the most realistic picture possible of the phase-space distribution of dark matter in the solar neighbourhood, one must turn to full cosmological simulations. As will be presented in the upcoming chapter, this involves performing simulations with periodic boundary conditions and a proper normalization of the perturbations.

6. COSMOLOGICAL SIMULATION

In order to apply the reverse-run technique to the problem of dark-matter detection in the solar neighbourhood, one requires a traditional N-body simulation which contains a region that resembles the Milky Way. Several studies have been done to generate N-body initial conditions which evolve into systems which resemble the Local Group or Local Supercluster (Klypin et al., 2001; Hoffman and Zaroubi, 2000; Zaroubi, 2002). However, in order to understand the limitations of such techniques it is necessary to investigate the origin and evolution of density perturbations in the early universe, and their relationship to N-body initial conditions.

6.1 Initial Conditions

In the early universe, small density perturbations seed the growth of larger structures. The evolution of these density fluctuations can be modelled by considering the material as a simple gravitating perfect fluid governed by Poisson's equations and the conservation of mass and energy:

$$\nabla^2\Phi = 4\pi G\rho \tag{6.1}$$

$$\left(\frac{\partial\rho}{\partial t}\right)_{\vec{r}} + \nabla_{\vec{r}}\cdot\rho\vec{u} = 0, \tag{6.2}$$

$$\rho\left[\left(\frac{d\vec{u}}{dt}\right)_{\vec{r}} + (\vec{u}\cdot\nabla_{\vec{r}})\vec{u}\right] = -\nabla_{\vec{r}}p - \rho\nabla_{\vec{r}}\Phi \tag{6.3}$$

where $\vec{r}$ and $\vec{u}$ are the proper distance and velocity of a fluid element relative to a fixed origin. If one considers the evolution of the density contrast, $\delta = (\rho - \bar{\rho})/\bar{\rho}$, in comoving coordinates under the assumption of small perturbations ($\delta \ll 1$),

equations (6.2), (6.3), and (6.1) can be linearized (refer to Appendix B for details) to yield

$$\frac{\partial^2\delta}{\partial t^2} + 2\frac{\dot{a}}{a}\frac{\partial\delta}{\partial t} = \frac{4\pi G\rho_0}{a^3}\delta \tag{6.4}$$

where $a(t)$ is the cosmological expansion factor. The solution to (6.4) is (Peebles, 1980):

$$\delta_1(\vec{x},t) = \frac{\dot{a}}{a}\int_0^t \frac{dt}{\dot{a}^2}\,\delta(\vec{x},t_0),\quad \delta_2(\vec{x},t) = \frac{\dot{a}}{a}\,\delta(\vec{x},t_0) \tag{6.5}$$

Note that δ_1 describes the evolution of a growing perturbation, while δ_2 describes a decaying mode.

To generate initial conditions appropriate for a cosmological simulation, one starts with a cube of uniformly distributed particles. These particles are then perturbed to match the density contrast predicted from linear theory. A technique to accomplish this was first presented by Zel'Dovich (1970). If the initial comoving location of a particle is $\vec{q}$ and it has no peculiar velocity, then its perturbed position, $\vec{x}$ and velocity, $\vec{v}$, at time t are

$$\vec{x}(t) = \vec{q} + \delta_1(t)\sum_{\vec{k}}\frac{i\vec{k}}{k^2}\delta_k e^{i\vec{k}\cdot\vec{q}} \tag{6.6}$$

$$\vec{v}(t) = \dot{\delta}_1(t)\sum_{\vec{k}}\frac{i\vec{k}}{k^2}\delta_k e^{i\vec{k}\cdot\vec{q}} \tag{6.7}$$

(see Appendix B for technical details). Here $\delta_1(t)$ is the linear growth factor given in equations (B.13) or (B.16) depending upon the cosmology under investigation and δ_k is related to the initial power spectrum of density perturbations in the early universe, $P(k)$, via

$$P(k) = \langle\delta_k\rangle^2 \tag{6.8}$$

Note that in general δ_k is a complex value to allow for both the amplitude and the phase of the perturbations. In order to construct realistic N-body simulations, one must determine the proper form for the power spectrum, $P(k)$.

6.1.1 Power Spectrum

Inflationary models and "naturalness" arguments (Peebles, 1993, for example) indicate that a scale-free power spectrum is likely with

$$P(k) \propto k^n \tag{6.9}$$

with $n = 1$. Recent observations of the cosmic microwave background support this model indicating that $n = 0.99 \pm 0.04$ (Spergel et al., 2003). If, as the universe evolves, the various components of the early universe behave in the same manner, the perturbations would continue to have this form on all scales. However, interactions between radiation, baryonic matter, and dark matter can act to suppress the growth of perturbations on particular scales. For example, prior to the epoch of recombination, density fluctuations propagate as acoustic waves in both the photons and baryons due to strong coupling. After recombination the situation changes. The two components now evolve separately which causes the shape of the initial power law spectrum to be modified. The full details of the evolution of the early universe have been numerically modelled in exquisite detail in the numerical package CMBfast (Zaldarriaga and Seljak, 2000). This utility would allow the complete determination of the power spectrum. It is very computationally intensive, calculating much more than the power spectrum and it is not practical for many situations which do not need such accurate detail or auxillary information. Instead, several empirical fitting formulae have been derived to allow rapid approximations of the power spectrum for a variety of cosmologies. The power spectrum is usually split into the power-law component, and the transfer function, $T(k)$.

$$P(k) = Ak^n T^2(k) \tag{6.10}$$

where A is a normalization factor. The model form of the transfer function used here is given by Eisenstein and Hu (1998).

The transfer function can differ considerably depending upon the cosmological

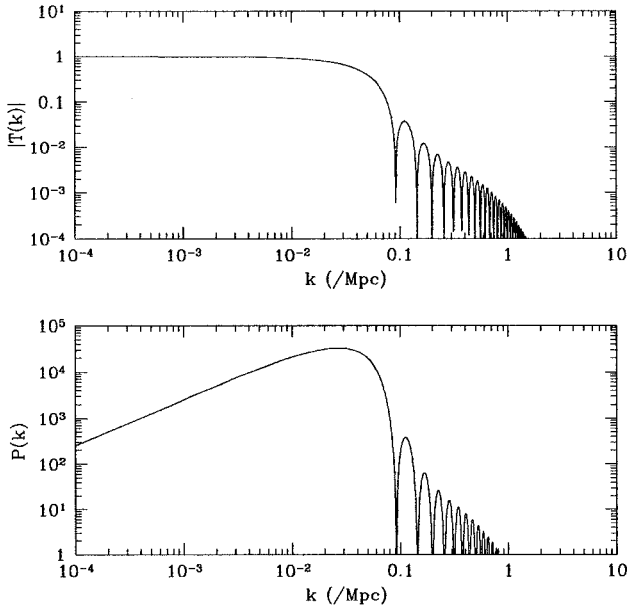

Figure 6.1: Transfer function (top) and power spectrum (bottom) for a flat baryon-dominated universe ($\Omega_b = \Omega_M = 1, \Omega_\Lambda = 0$). Note the numerous features at large k introduced by baryon interactions.

model under investigation. Any flat cosmology can be characterized by three primary parameters:

$\mathbf{\Omega_M}$ The amount of matter (both dark and baryonic) in the universe,

$\mathbf{\Omega_b}$ The amount of baryons in the universe (Note that $\Omega_b \leq \Omega_M$.)

$\mathbf{\Omega_\Lambda}$ The strength of the cosmological constant

Note that all parameters are measured as fractions of the critical density. (Refer to Appendix A for a review of cosmology and cosmological parameters.) Observations indicate that the universe is flat which requires $\Omega_M + \Omega_\Lambda = 1$. One of the simplest, original cosmological models is a baryon-dominated universe with $\Omega_b = \Omega_M = 1$, and $\Omega_\Lambda = 0$. In the early universe, there are complex interactions between baryonic matter and between baryons and photons such as the propagation of acoustic waves

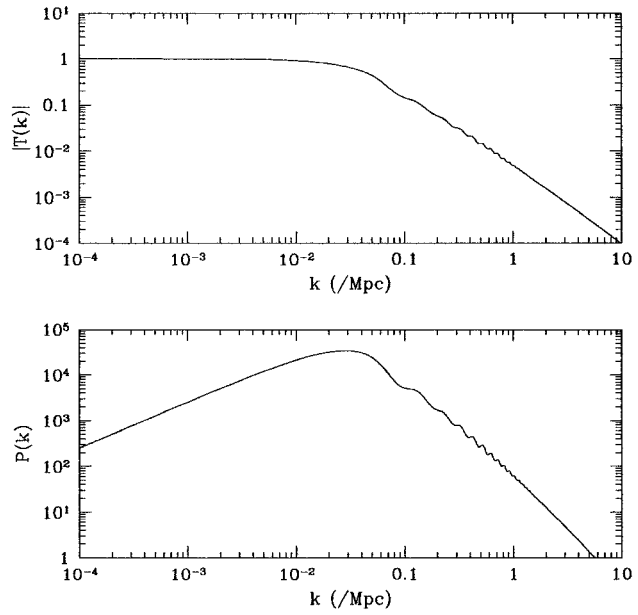

Figure 6.2: Transfer function (top) and power spectrum (bottom) for a $\Omega_b = 0.5, \Omega_M = 1.0, \Omega_\Lambda = 0$ universe.

in the plasma and Compton drag. As shown in Figure 6.1, these interactions give rise to a rapid falloff in the transfer function and numerous oscillations in the power spectrum. When dark matter is added to the mix, such as for the half baryonic matter ($\Omega_b = 0.5$), and half weakly interacting dark matter ($\Omega_M = 1$) model shown in Figure 6.2, the baryonic interactions are dampened. The power spectrum has a less pronounced k-cutoff, but still has noticeable features at large k. Figure 6.3 reflects the model currently favoured by observations of the cosmic microwave background (CMB) (Spergel et al., 2003) and supernova measurement results (Perlmutter et al., 1999) with $\Omega_b = 0.04, \Omega_M = 0.27$ and, $\Omega_\Lambda = 0.73$. Due to the very small baryonic fraction of this model, baryons have a negligible effect in the early universe. The evolution of the power spectrum is dominated by the cosmological constant and dark matter. As a result, this power spectrum is very smooth and can be well fit by

$$P(k) = Ak(1 + b_1 k^2 + b_2 k^{3.5})^{-1} \tag{6.11}$$

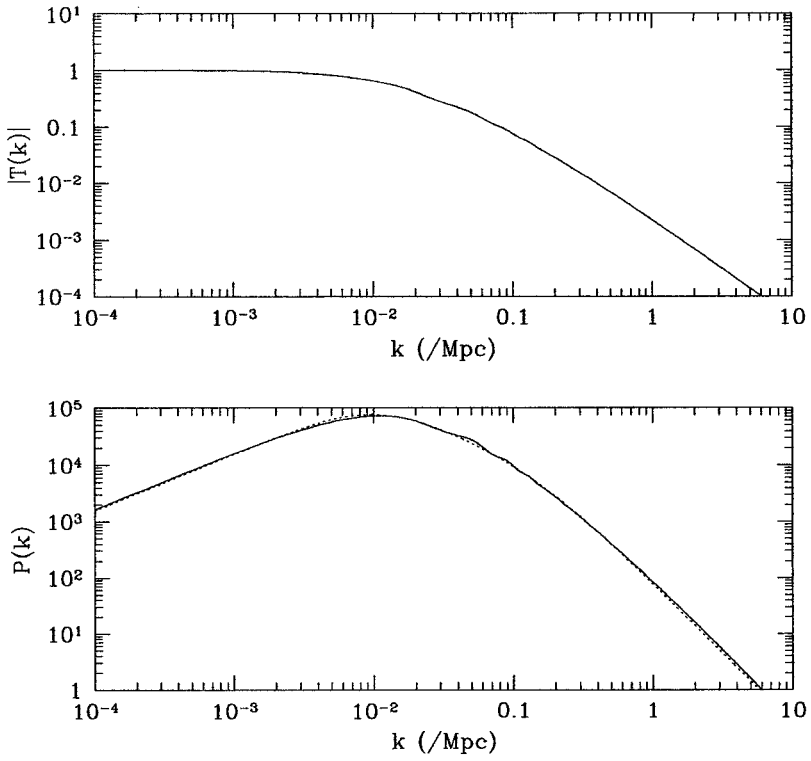

Figure 6.3: Transfer function (top) and power spectrum (bottom) for a $\Omega_b = 0.04, \Omega_M = 0.27, \Omega_\Lambda = 0.73$ universe. The dashed line is the fit from equation (6.11).

with $A = 1.57 \times 10^7, b_1 = 1.04 \times 10^4, b_2 = 1.96 \times 10^5$. The fit curve is the dashed line in Figure 6.3.

While careful modelling of the physics of the early universe can describe the location and relative amplitude of the features in the power spectrum, there is currently no way to predict the overall normalization. To determine this, one must look at observational constraints.

6.1.2 Normalization

There are two methods used to normalize the primordial power spectrum. The first is based on measurements of the cosmic microwave background from the COBE

satellite, while the second is constrained by galaxy counts. Using the COBE data, Bunn and White (1997) have determined that the present-day normalization of the power spectrum is well fit by

$$P(k) = \frac{2\pi^2}{k^3}\delta_H^2 \left(\frac{ck}{H_0}\right)^{3+n} T^2(k) \tag{6.12}$$

where the normalization parameter, δ_H, is given by

$$\delta_H = \begin{cases} 1.95 \times 10^{-5}\Omega_M^{-0.18-0.19\ln\Omega_M - 0.17n} e^{0.86-0.72n-0.14n^2} & \text{if } \Omega_\Lambda = 0 \\ 1.94 \times 10^{-5}\Omega_M^{-0.785-0.05\ln\Omega_M} e^{0.781-0.612n-0.169n^2} & \text{if } \Omega_\Lambda = 1-\Omega_M \end{cases} \tag{6.13}$$

The second way to normalize the power spectrum requires the variance of mass fluctuations within a sphere of radius R. (Peebles, 1980, for example). The mass variance is given by

$$\sigma^2(R) = \int_0^\infty Ak^{n+3}T^2(k)\left(\frac{3(\sin kR - kR\cos kR)}{(kR)^3}\right)^2 dk \tag{6.14}$$

$\sigma(R)$ is an observable quantity which can be used to constrain A. For $R = 8h$ Mpc, $\sigma(8h)$ is of order unity. However, for the simulations presented here, the COBE normalization will be used.

The normalized power spectrum presented above is the *present-day* power spectrum that is linearly interpolated from the initial small fluctuations. To generate initial conditions for a numerical simulation, one needs the power spectrum at the initial time of the simulation. Therefore, the present-day power spectrum must be extrapolated backwards in time using the linear growth factors described in Appendix B.1.

$$P(k;z) = P(k;z=0)\left(\frac{\delta(z)}{\delta(z=0)}\right)^2 \tag{6.15}$$

For example, Figure 6.4 compares the power spectrum using the present-day normalization (upper curve) to that at $z = 15$ (lower curve). As expected, the amplitude of the power-spectrum, and hence the magnitude of the initial perturbations, are significantly reduced.

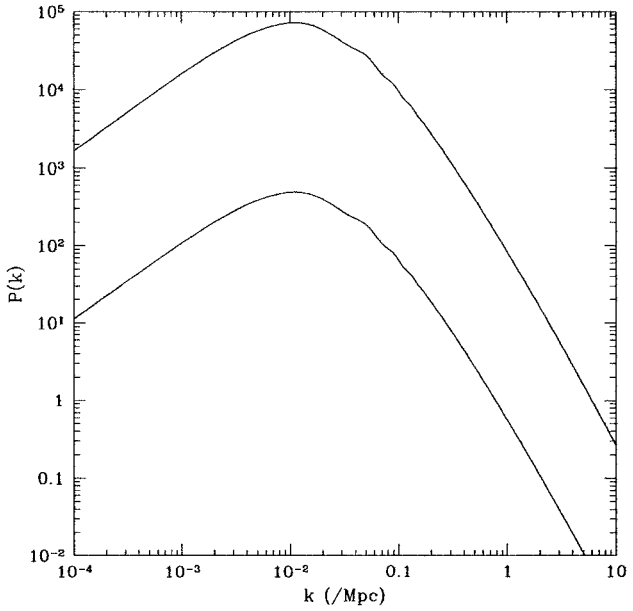

Figure 6.4: The present-day power spectrum (upper curve) and the power spectra scaled to $z = 15$ (lower curve).

6.2 Local Group Simulations

The Milky Way exists in a small group of about 40 galaxies called the Local Group. Of these galaxies, the Milky Way and the Andromeda Galaxy (M31) are the dominant members while the remainder are relatively small dwarf galaxies. The Milky Way has a mass of approximately $2.5 \times 10^{12} M_{\odot}$ (Sakamoto et al., 2003; Wilkinson and Evans, 1999). The mass of M31 is less well known but current estimates indicate that it is roughly $1.5 \times 10^{12} M_{\odot}$ but depends upon the assumed mass distribution (Evans and Wilkinson, 2000; Gottesman et al., 2002; Côté et al., 2000). The next largest member of the Local Group with a known mass is M33 with a mass of just $2.5 \times 10^{10} M_{\odot}$ (Mateo, 1998). Therefore, the dynamics of the Local Group are largely governed by the Milky Way and M31. These galaxies are currently separated by a distance of 770 kpc (Freedman and Madore, 1990).

In order to ensure that the N-body simulations resemble the Local Group, it

is important that the Milky Way and M31 exist in the simulation with properties similar to those stated above. Ideally, in order to form systems which are similar to the region around the Milky Way, the amplitude and phases of the power spectrum could be constrained by observations of the present-day mass fluctuations and velocity flows. Klypin et al. (2001) successfully constrain the power spectrum to form the Local Supercluster, a region much larger than the Local Group, and identify all of its major components such as the Virgo, Perseus-Pisces, and Coma clusters as well as the Great Attractor. However, all of these features exist on scales and distances of tens to hundreds of megaparsecs. When looking at smaller features on the order of a megaparsec, such as the galaxy distribution in the Local Group, the evolution of structure is only weakly constrained and the correlation between the simulation results and observations is tenuous. Therefore, observational constraints cannot currently be used to significantly constrain the initial conditions of simulations on the scale of the Local Group. Alternative techniques must be used to ensure that the simulation results sufficiently match the true distribution of galaxies in the Local Group. The simplest method is to simply run a suite of small-N simulations with different initial conditions and pick the one which most closely resembles to Local Group for use in higher resolution studies.

In order to apply the reverse-run technique to investigate the distribution of dark matter in the solar neighbourhood, one requires a simulation with sufficient resolution that the mass distribution is reasonably accurate. This can be accomplished in two complimentary manners:

1. use a large number of particles, and

2. only simulate the region required.

Therefore, the forward simulation is designed such that the total mass is comparable to that of the Local Group, $M_{\rm LG} = 5 \times 10^{12} M_{\odot}$. Assuming that the mean density of matter over the Local Group volume is the same as that of the universe as a whole,

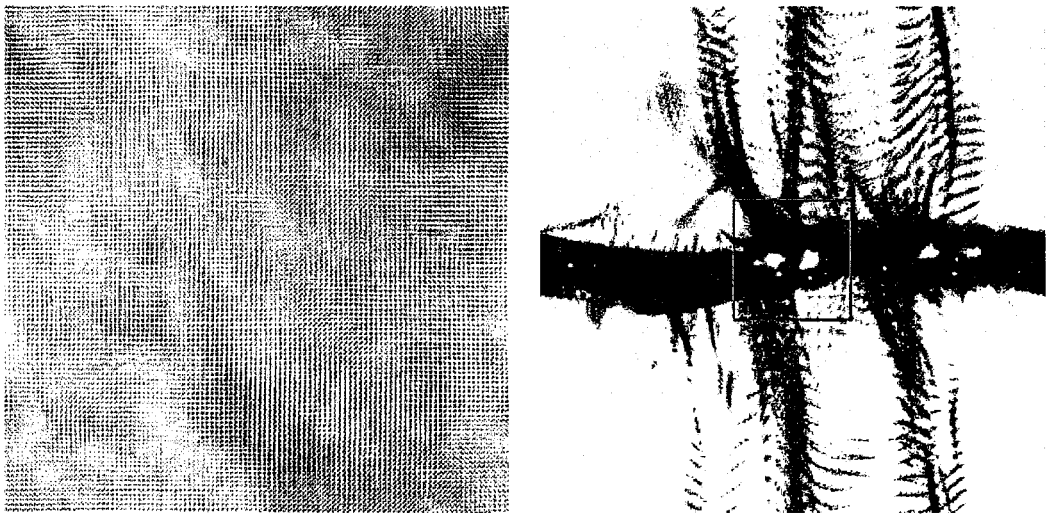

Figure 6.5: The initial conditions (left) and the final state (right) of local cluster simulation. The colour represents the density ranging from low-density (blue) to high-density (yellow), though the absolute densities vary significantly between each panel. The region which resembles the Local Group is indicated by the green box.

the present-day length of a side of the simulation volume must be

$$L = \left(\frac{8\pi M_{\rm LG} G}{3\Omega_M H_0^2}\right)^{1/3} \tag{6.16}$$

where Ω_M is the current cosmological mass density and H_0 is the present-day Hubble constant. In order to ensure that sufficient environmental effects due to regions surrounding the Local Group are included, a total mass of $M = 3.6 \times 10^{13} M_\odot$ was used which yields a simulation volume with $L = 10$ Mpc.

6.3 Forward Run Results

Figure 6.5 shows the initial and final state of a forward-run simulation with 10^6 particles. The green box in the right-hand panel indicates the region similar to the Local Group in that it contains two large galaxies, each with masses of approximately $3 \times 10^{12} M_\odot$ separated by 720 kpc. These galaxies are slightly larger than the true

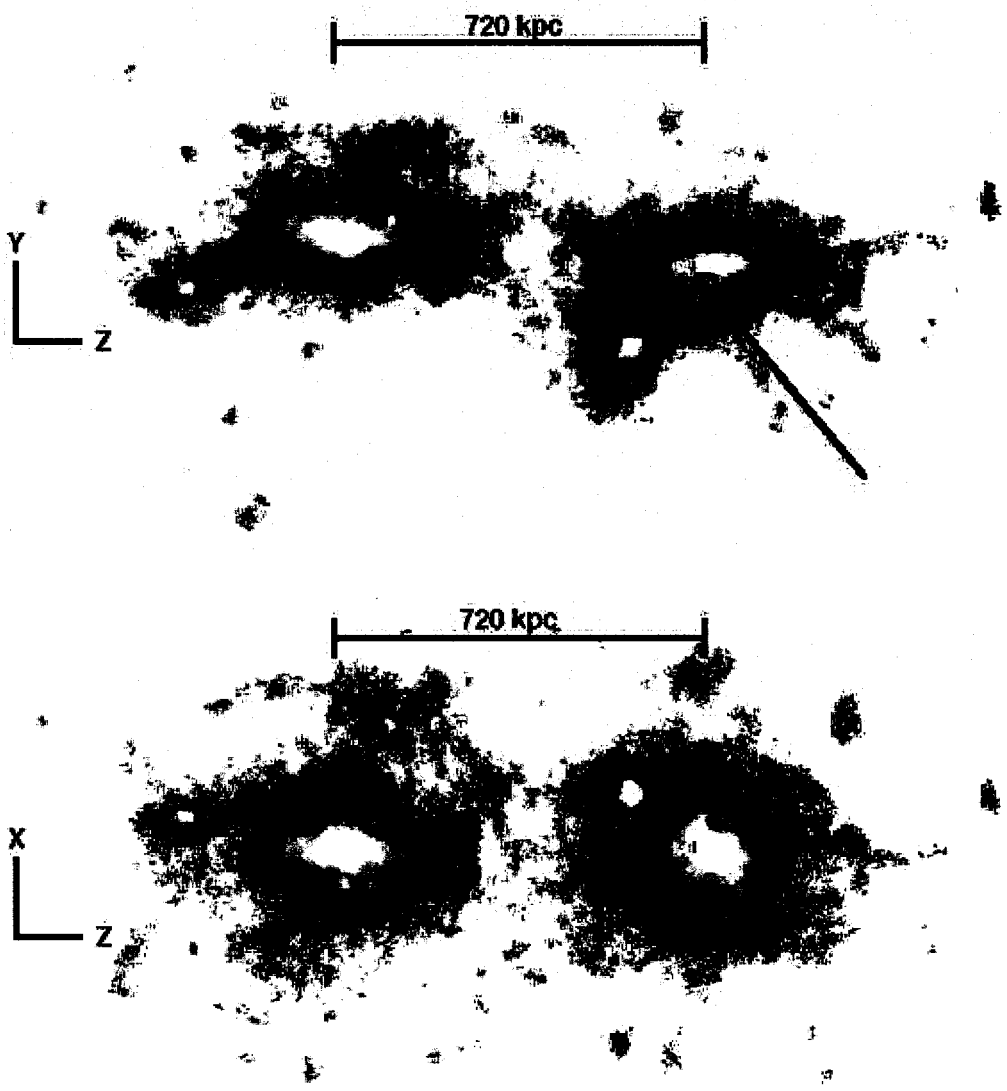

Figure 6.6: A close up of the "Local Group" environment shown in the $x - z$ and $y - z$ projections. The separation of the centres of the two main galaxies is 720 kpc. The point of interest, located approximately 25 kpc (the softening length) from the centre of the "Milky Way" on the right, is indicated by the green dot and arrow. Blue is low density, yellow is high density.

Number of massive particles	10^6
Number of test particles	5×10^5
Simulation box size	10 Mpc
Softening length	25 kpc
Initial redshift	35
Number of steps	1000

Table 6.1: Summary of parameters for the "Local Group" simulation.

masses of the Milky Way ($2.5 \times 10^{12} M_\odot$) and M31 ($1.5 \times 10^{12} M_\odot$) and slightly closer together at 720 kpc than the currently accepted distance of 770 kpc. Nonetheless, the dynamics of the system are likely a close approximation to the dynamics of the true Milky Way/M31 system. Figure 6.6 shows a close-up of the simulated "Local Group." The point of interest, indicated by the green dot and arrow, lies roughly 25 kpc from the centre of one galaxy. This distance is roughly equal to the softening length used in the simulation. A summary of the parameters used in the simulation are shown in Table 6.1.

It should be noted that the apparent regularity in the final distribution, particularly the numerous, approximately horizontal density contrasts, is a selection effect due to the requirement that the simulation have a region which resembles the Local Group with two large galaxies resembling the Milky Way and M31. If a different random seed had been used, no such regularity would be appear.

Figure 6.7 shows the speed distribution obtained using the $\sqrt{N} \sim 1000$ nearest particles to the point of interest. Note how the speed distribution is quite smooth, with no significant features. While this tends to indicate that the distribution of dark matter is smoothly distributed in velocity space, there is also the possibility that the particles are moving in a coherent direction but with a smooth spread of speeds. To check for this possibility, one can examine the distribution of angles, θ, between dark matter particles and the bulk motion in the region surrounding the detector. If

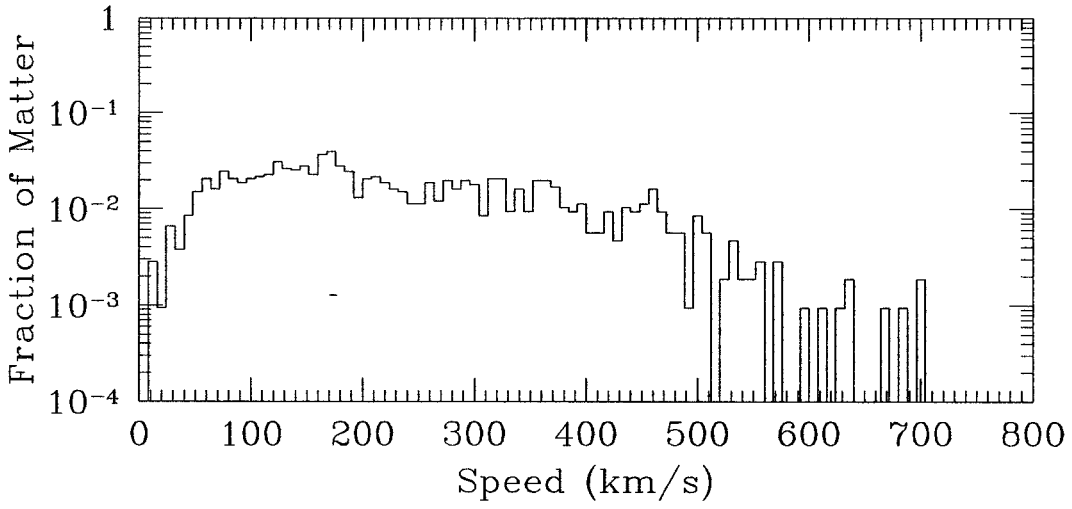

Figure 6.7: The speed distribution at the point of interest obtained from the forward run using the nearest $\sqrt{N} \sim 1000$ particles.

the particles are moving coherently, or in several smaller flows, the particles should be be clumped in $\cos\theta$-speed parameter space. On the other hand, if the particles are smoothly distributed throughout velocity-space, there should be no significant correlations. Figure 6.8 shows that the particles are randomly distributed with respect to the mean motion in the region surrounding the point of interest. From the standard forward cosmological simulation, there are no clear indications of any streams or clumps of dark matter passing through the solar neighbourhood. This is the result found by others (Moore et al., 1998; Helmi et al., 2003).

6.4 Reverse Run Results

Applying the reverse-run technique to the Local Group simulation yields a significantly different picture of the speed distribution. Instead of the rather smooth distribution shown in Figure 6.7, Figure 6.9 shows a complicated distribution with numerous peaks and voids.

Furthermore, the streams of dark matter are not uniformly distributed in direc-

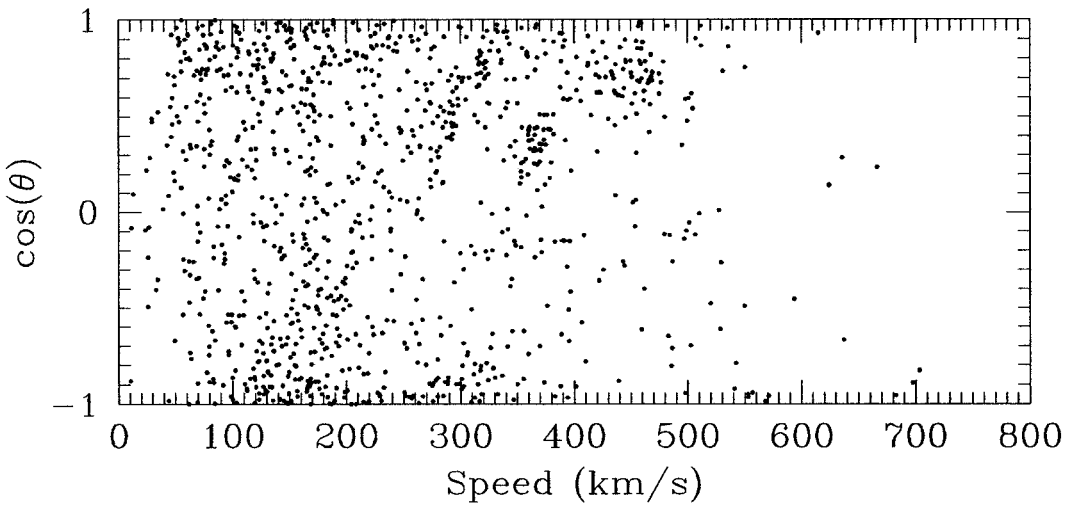

Figure 6.8: The angular distribution of $\sim$ 1000 particles near the point of interest shows no clear correlation between the angle and speed.

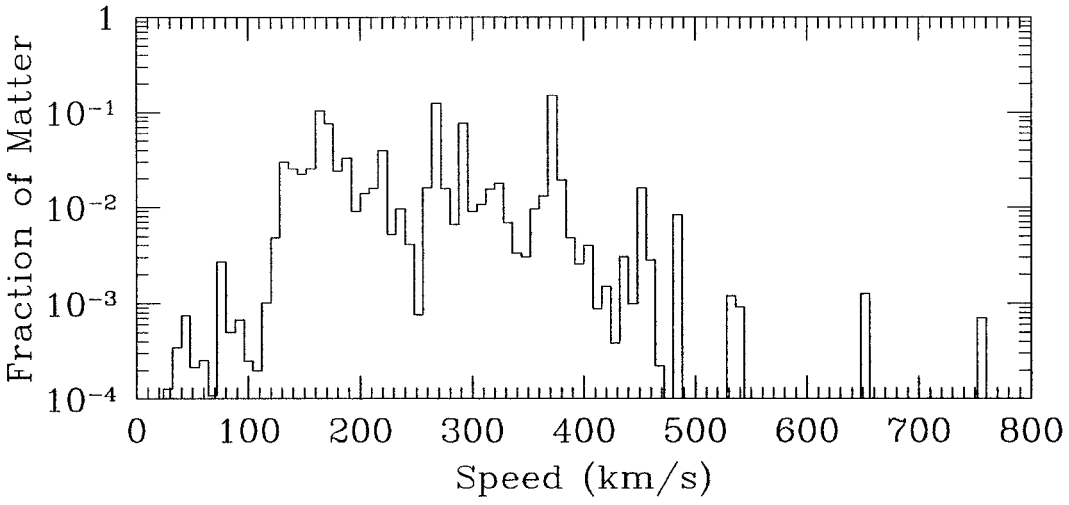

Figure 6.9: The speed distribution at the point of interest obtained from the reverse-run technique.

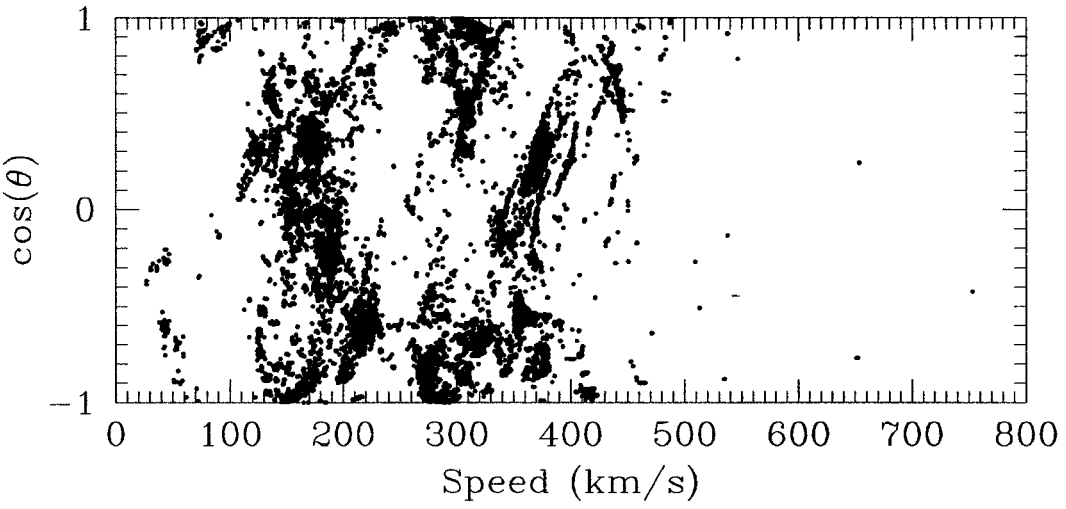

Figure 6.10: The speed of dark matter particles versus the angle between each particle's velocity and the bulk motion of the forward simulation. The dark matter streams are not uniformly distributed preferentially arriving from specific directions.

tion. Figure 6.10 shows the direction that the dark matter particles are travelling relative to the mean motion in the region surrounding the point of interest. At a given speed, the particles tend to be clumped in direction rather than uniformly distributed in all directions. This indicates that the dark matter is in streams or partial shells of infalling material rather than thoroughly virialized into a smooth distibution.

It should be noted that since the location of the detector was chosen to be 25 kpc from the Galactic centre, the velocities from the simulation tend to be lower than those found in the solar neighbourhood which is 8 kpc from the centre. In order to more accurately represent the dark matter as viewed from the Earth, the simulation velocities were scaled up by the ratio of the circular velocities ($v_{\rm circ} \propto r^{-1/2}$) from $r = 25$ kpc to $r = 8$ kpc. This may have the effect of slightly overestimating the amount of structure present since the system may be slightly less evolved farther from the Galactic centre. This issue can be overcome by simply using a higher

resolution simulation in the future.

The combination of the results from the cosmological reverse-run simulations, and the semi-analytic modelling from Chapter 4, indicate that the dark matter distribution in the solar neighbourhood is not smooth. Instead it is composed of a set of distinct dark matter streams with unique velocities and effectively random orientations. This picture of the dark matter in the solar neighbourhood is significantly different than that traditionally assumed for dark matter detection experiments. Chapter 7 will now examine the implications of non-uniform dark matter distributions on the expected signatures of terrestrial dark matter detection experiments.

7. EFFECTS OF SUBSTRUCTURE ON DARK MATTER DETECTION

The results from the Chapters 4 and 6 indicate that the local distribution of dark matter is not well modelled by a smooth Maxwellion distribution. Instead the velocity distribution of dark matter in the solar neighbourhood has at least a small component which is "streaming" possibly with a velocity significantly higher than the mean speed expected from a virialized dark matter distribution. As dark matter detectors become more advanced and obtain more data, they must start considering the possibility that the dark matter distribution is not smooth. The demonstration in Chapter 1 indicated that substructure in velocity-space could have a significant impact on the dark matter detection spectra. In order to examine this effect in more detail, one must first determine the velocity of the dark matter relative to the detector taking into account the motion of the Sun through the Galaxy, and the Earth's orbit about the Sun. Once the correct relative velocities are determined, detection spectra can be modelled and compared for both uniform (Maxwellian) and non-uniform (N-body) distribution.

7.1 Current Dark Matter Detectors

There are currently over 20 dark matter detectors in various stages of development and operation around the world searching for both WIMPs and axions. As these detectors increase their exposures and sensitivities, it will be necessary to have an accurate model of the dark matter distribution in the solar neighbourhood.

7.1.1 WIMP Detectors

At present, there are many more WIMP detectors in operation or under development than axion detectors. Three of the leading detectors, representative of different approaches to WIMP detection, are the Cryogenic Dark Matter Search (CDMS) (Abrams et al., 2002, for example), the DAMA detector (Bernabei et al., 2002), and DRIFT (Martoff et al., 1999). The DAMA experiment, which detects photons emitted when a WIMP scatters with NaI in the detector, has reported a positive detection of the annual modulation (to be discussed in Section 7.2.2) of the WIMP signal (Bernabei et al., 2002). However, CDMS and several other experiments such as EDELWEISS (EDELWEISS Collaboration et al., 2002) and the Zeplin series of experiments (Lüscher et al., 2001), have not detected any significant WIMP signal. In particular, CDMS has detected only 23 possible events, all of which are consistent with a neutron background. An analysis of the CDMS results excludes the region of WIMP masses and interaction cross-section parameter space favoured by DAMA at the 99.9% confidence level. Figure 7.1 shows the current limits of several WIMP detectors. The region above the curves is eliminated. It is important to note that the standard analysis assumes a smooth dark matter distribution in the solar neighbourhood. Copi and Krauss (2003) and Belli et al. (2002) have investigated the effect of smooth non-isotropic dark matter distributions on CDMS and DAMA results with conflicting conclusions.

DRIFT is a directionally-sensitive detector which has only recently started operation. It has not yet released any data regarding WIMP masses or cross-sections. However, due to its exceptional background rejection, it should be able to clearly identify a smooth Maxwellian halo with fewer than 100 detection events (Martoff et al., 1999).

The next generation of WIMP detectors is already under development including improvements to CDMS, EDELWEISS, Zelplin, and DRIFT. In all cases, the new detectors will strive to increase efficiency and sensitivity by several orders of mag-

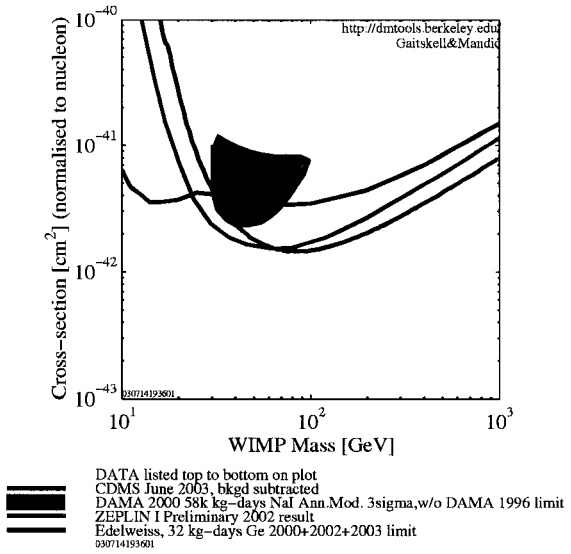

Figure 7.1: The current exclusion limits for WIMP candidates from a variety of detectors. The region favoured by DAMA is indicated by the solid red region. Figure from http://dmtools.berkeley.edu/

nitude. A proper understanding of the local dark matter distribution is essential to take full advantage of the improvements in upcoming detectors.

7.1.2 Axion Detectors

There are several axion experiments presently in operation. These includes the Axion Dark Matter Experiment (ADMX) (Asztalos et al., 2002), CAST (Zioutas et al., 1999), and PVLAS (Cantatore et al., 2001). Of these detectors, only ADMX is searching for cosmological axions. CAST primarily focuses on axions arriving from the Sun, while PVLAS looks for any axions created in a terrestrial laboratory experiment. Nonetheless, all three can place constraints on the possible range of axion mass and cross-section. Figure 7.2 shows the current range of excluded axion masses and cross-sections obtained from ADMX (Asztalos et al., 2002). Note the very fine energy resolution with which the axion mass could be determined. Current axion detectors have exceptional energy resolution on the order of $\Delta E/(m_a c^2) \sim$

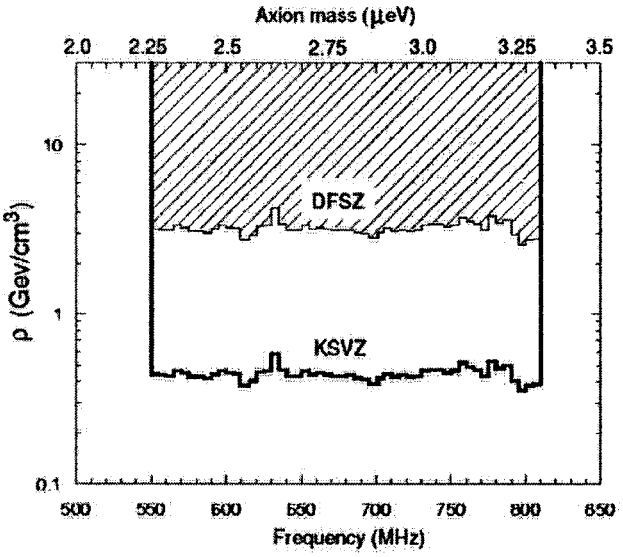

Figure 7.2: The current exclusion limits for axion candidates from ADMX for the two different axion models. Regions inside the curves (i.e. where the labels are located) are excluded. Figure from Asztalos et al. (2002).

10^{-11} (Asztalos et al., 2001) where m_a is the rest-mass of the axion. This high energy resolution could provide a very high resolution spectrum of the speed distribution of dark matter in the solar neighbourhood.

7.2 The Earth's Motion in the Galaxy

All of the previously mentioned dark matter detectors are sensitive to the speed distribution of the dark matter. In Chapter 1, it was shown that WIMP recoil spectra depend upon the integrated one-dimensional speed distribution (equation 1.7) due to the random scattering angle in the nuclear collision. On the other hand, axion detectors can directly determine the speed distribution by measuring the energy of the photon created through Primakoff conversion. Ideal directionally-sensitive detectors can measure the full three-dimensional velocity distribution. In all cases however, the detection event is dependent upon the velocity of the dark matter relative to

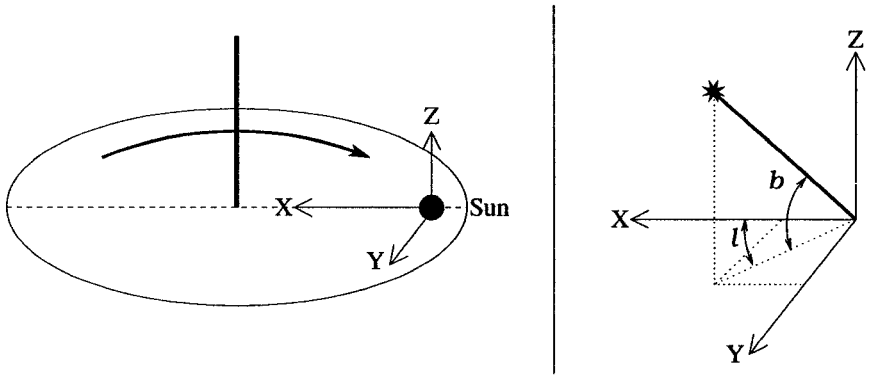

Figure 7.3: The Sun's motion in Galactic coordinates (left) and the definition of Galactic latitude (b) and longitude (l) on the right.

the Earth. Since the Earth is not stationary in Galactic coordinates, the velocity of the dark matter must be transformed to the correct frame of reference.

7.2.1 Solar Motion

In all of the discussion of the velocity distribution of dark matter so far, the frame of reference was that of the overall system in isolated systems, or relative to the Galaxy being examined. For example, in the cosmological simulations of the formation of the Local Group in Chapter 6, the velocities were measured with respect to the motion of the Milky Way-like galaxy. However, the velocity of interest for terrestrial dark matter detection experiments is the velocity of the dark matter relative to the Earth. To first order, this can be accounted for by simply considering the Sun's motion around the centre of the Galaxy. Though there is uncertainty in the speed with which the Sun orbits the Galactic centre, the most commonly accepted value is roughly 230 km s^{-1}(See for example Feast and Whitelock, 1997; Kerr and Lynden-Bell, 1986). In Galactic coordinates, as shown in Figure 7.3, the Sun moves in the positive Y direction[1] with positive X towards the Galactic centre. Therefore, the

[1] Technically, the postive Y direction is defined by the motion of the Local Standard of Rest (LSR) which is the average motion of stars in the region surrounding the Sun. The Sun has a

Sun's velocity in Galactic coordinates is simply

$$\vec{v}_{\odot} = (0, 230, 0) \text{ km s}^{-1} \tag{7.1}$$

It is also convenient to define Galactic latitude (b) and longitude (l) to specify where objects appear on the sky. As illustrated in Figure 7.3, Galactic latitude is the angle above or below the Galactic plane, while Galactic longitude is the angle in the plane from the Galactic centre. Since the Sun is travelling in the plane in the positive Y direction, it is headed in the direction $(b, l) = (0, 90°)$.

If, on average, the dark matter is at rest with respect to the Galaxy, the Sun's motion will effectively create a "wind" of particles flowing against the Earth's motion. This would results in a significant directional bias for dark matter detection events. The implications of this directional sensitivity will be investigated later. The Sun's motion through the Galaxy also boosts the velocity of dark matter particles compared to in the Galactic frame. This results in higher velocities and more available energy to deposit in dark matter detectors.

7.2.2 Seasonal Variation

Though the Sun's motion about the Galactic centre, and the motion of the dark matter itself, are the dominant contributions to the relative velocity between the dark matter and the Earth, there is another small, but important, velocity shift due to the Earth's motion about the Sun. For both smooth and non-uniform dark matter distributions, the Earth's orbit around the Sun can cause a seasonal modulation in the detected spectra. As illustrated in Figure 7.4, for half of the year a component of the Earth's orbital velocity will be partially aligned with the orbital motion of the Sun around the centre of the Galaxy. This effectively increases the Earth's speed relative to the Galaxy. For the other six months, the opposite is true and the Earth's

small, constant, peculiar velocity with respect to the LSR which would shift the Sun's velocity from the pure Y direction.

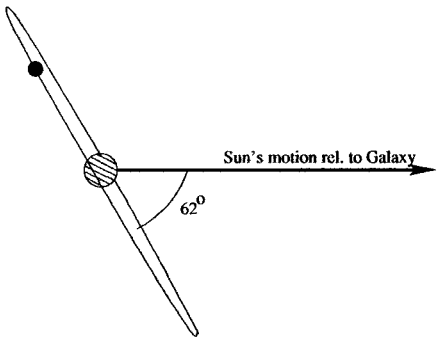

Figure 7.4: The Earth's motion around the Sun increases and decreases its net speed through the Galaxy.

speed is effectively reduced. The velocity of the Earth in Galactic coordinates can be approximated by (Gelmini and Gondolo, 2001)

$$\vec{v}_e(t) = v_e \left[\hat{e}_1 \sin\omega(t - t_0) - \hat{e}_2 \cos\omega(t - t_0)\right] \tag{7.2}$$

where $v_e = 29.8$ km s^{-1} is the Earth's orbital speed, $\omega = 2\pi \text{yr}^{-1}$ is the Earth's angular speed, $t_0 \sim 80$ days is the time of the vernal equinox, and $\hat{e}_1$ and $\hat{e}_2$ point towards the Sun at the spring equinox and summer solstice respectively:

$$\hat{e}_1 = (-0.0670, 0.4927, -0.8676) \tag{7.3}$$

$$\hat{e}_2 = (-0.9931, -0.1170, 0.01032) \tag{7.4}$$

This approximation neglects the small ellipticity of the Earth's orbit but, as shown in Green (2003), the maximum difference between the much more complicated full expression and this approximation is only about 1 km s^{-1}.

Therefore, the velocity of the Earth in Galactic coordinates is

$$\vec{v}_e = v_e \left[\hat{e}_1 \sin\omega(t - t_0) - \hat{e}_2 \cos\omega(t - t_0)\right] + (0, 230, 0)\text{km s}^{-1} \tag{7.5}$$

Figure 7.5 shows the variation in Galactic speed due to the Earth's motion about the Sun. It ranges from 216 km s^{-1} in December to 246 km s^{-1} in June.

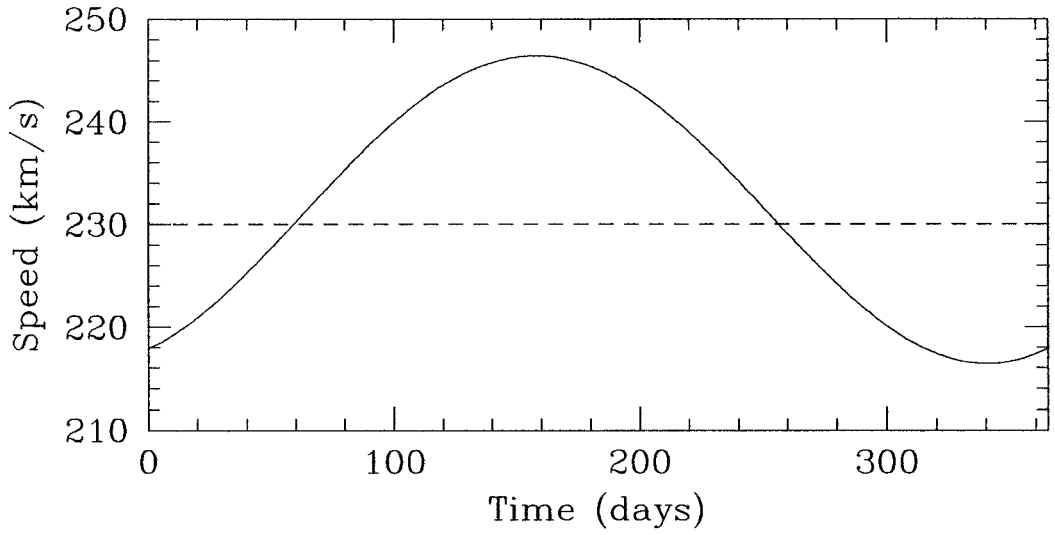

Figure 7.5: The yearly variation of the speed of the Earth in Galactic coordinates due to the Earth's motion about the sun.

As will be shown, this slight shift in speeds throughout the year can have a noticeable effect on dark matter spectra and can be used both to help distinguish true detection events from the background and to reconstruct dynamical properties of any non-uniform streaming component of the dark matter. In order to quantify the effect that the seasonal modulation has on detection experiments, it is useful to define the seasonal modulation factor:

$$\mathcal{F} = \frac{\text{Rate(June)} - \text{Rate(December)}}{\text{Rate(June)} + \text{Rate(December)}} \tag{7.6}$$

where the "Rate" refers to the detection measure appropriate for the dark matter candidate in question.

A careful analysis of the effect of the Earth's motion on predominantly smooth dark matter distributions by Green (2003) indicated that proper modelling of the Earth's seasonal motion is important and oversimplification of astrophysical constraints can lead to errors in interpretation of experimental results as large as tens of percent.

7.3 Analytic Detection Models

When modelling dark matter detection events, it has been traditionally assumed that the dark matter distribution can accurately be modelled as a smooth Maxwellian distribution truncated at the local Galactic escape speed. Various minor perturbations have been applied such as breaking the spherical symmetry by using an oblate or prolate halo, or adding some rotation (see for example Copi and Krauss, 2003; Belli et al., 2002). However, in order to compare the effects of velocity-space substructure to the traditional smooth assumptions, a simple Maxwellian distribution will be assumed. In the Galactic frame of reference, the distribution is

$$f(\vec{v}_{DG}) = \frac{1}{\pi^{3/2} v_o^3} e^{-v_{DG}^2/v_0^2} \tag{7.7}$$

where $v_0 = 220\text{km s}^{-1}$ is the halo velocity dispersion, and $\vec{v}_{DG}$ is the velocity of the dark matter (D) relative to the Galaxy (G). (Neglecting the cutoff at the escape speed of $v_e \sim 500$ km s^{-1} (Binney and Tremaine, 1987) has a negligible effect on the detection spectra since over 98.5% of the particles in this Maxwellian distribution have speeds below v_e.)

7.3.1 Axion Detectors

Axion detectors, based on the Primakoff conversion of axions to photons, obtain a direct measure of the total energy (rest mass plus kinetic) of the axions. Therefore, axion detectors can directly measure the *speed* distribution of dark matter.

For a Maxwellian distribution, the one-dimensional speed distribution in the frame of the Earth is

$$f_1(v_{DE}) = \frac{v_{DE}}{v_{EG} v_o \sqrt{\pi}} \left(\exp\left[-\frac{(v_{DE} - v_{EG})^2}{v_o^2} \right] - \exp\left[-\frac{(v_{DE} + v_{EG})^2}{v_o^2} \right] \right) \tag{7.8}$$

where v_{DE} is the speed of the dark matter relative to the Earth and v_{EG} is the speed of the Earth relative to the Galaxy. Since the Earth's speed relative to the Galaxy varies throughout the year as it orbits the Sun, the location and shape of

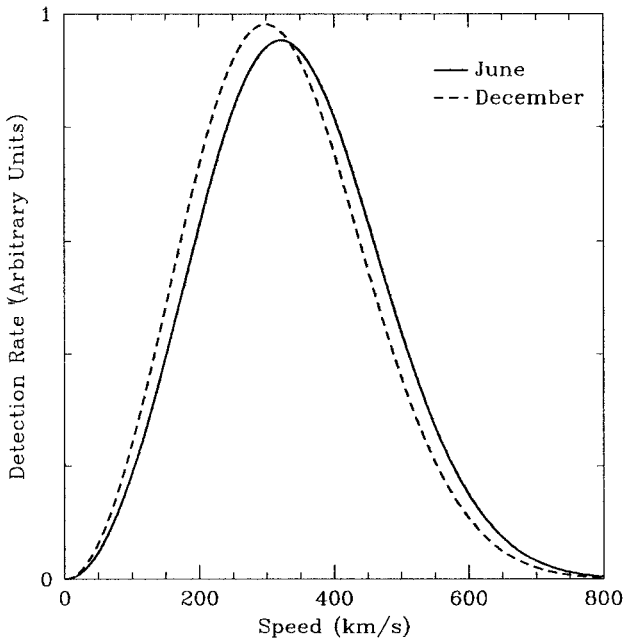

Figure 7.6: The seasonal shifting of an axion spectrum due to the Earth's motion around the Sun. The solid line shows the spectrum due to a smooth distribution in June, while the dashed line is the same distribution but for December.

the one-dimensional velocity dispersion will change slighty between the extrema in June and December. Figure 7.6 shows the expected detection spectra of an ideal axion detector in June and December.

In order to quantify the seasonal variation, it is useful to examine the seasonal variation defined in equation (7.6). Figure 7.7 clearly shows the bias of high-speed detections in June due to the increased relative speed between the Earth and the Galactic halo.

Current cosmological axion detectors are not directionally-sensitive (Daw, 2001). They only can detect that an axion has arrived, but cannot tell the direction from which it came. However, experiments which are searching for solar axions are directionally-sensitive and there have been proposals to adapt this technology to search for cosmological axions (Zioutas et al., 1999). If a directionally-sensitive

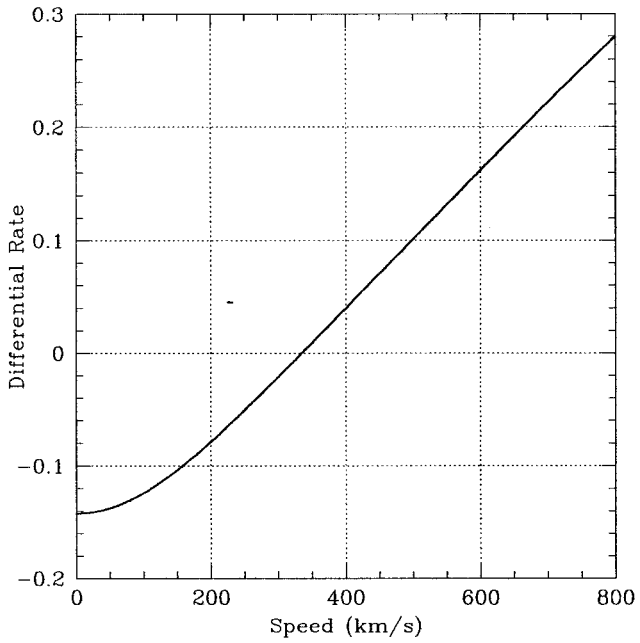

Figure 7.7: The seasonal modulation factor, as defined in equation (7.6), highlights the differences between the June and December spectra.

cosmological axion detector is constructed, it would be able to probe the full three-dimensional velocity distribution, $f(\vec{v}_{DE})$, directly. Separating the velocity of the dark matter into its component relative to the Earth, and the Earth's motion relative to the Galaxy yields the directional distribution function:

$$f(\vec{v}_{DE}) = \frac{1}{\pi^{3/2} v_0^3} e^{-(v_{DE}^2 + v_{EG}^2 + 2 v_{DE} v_{EG} \cos\theta)/v_o^2} \tag{7.9}$$

where θ is the angle between the direction of the dark matter in the Earth's frame and the direction of the Earth's motion. The top half of Figure 7.8 shows the expected detection rate (in units of maximum June detection rate) for a directionally-sensitive axion detector in June and December. Note the subtle changes in the shape of the contours due to the seasonal motion of the Earth. In June, slightly more high speed events are detected with a slight bias towards oncoming particles. In December, there is a slight increase in axions which are more parallel to the Earth's motion.

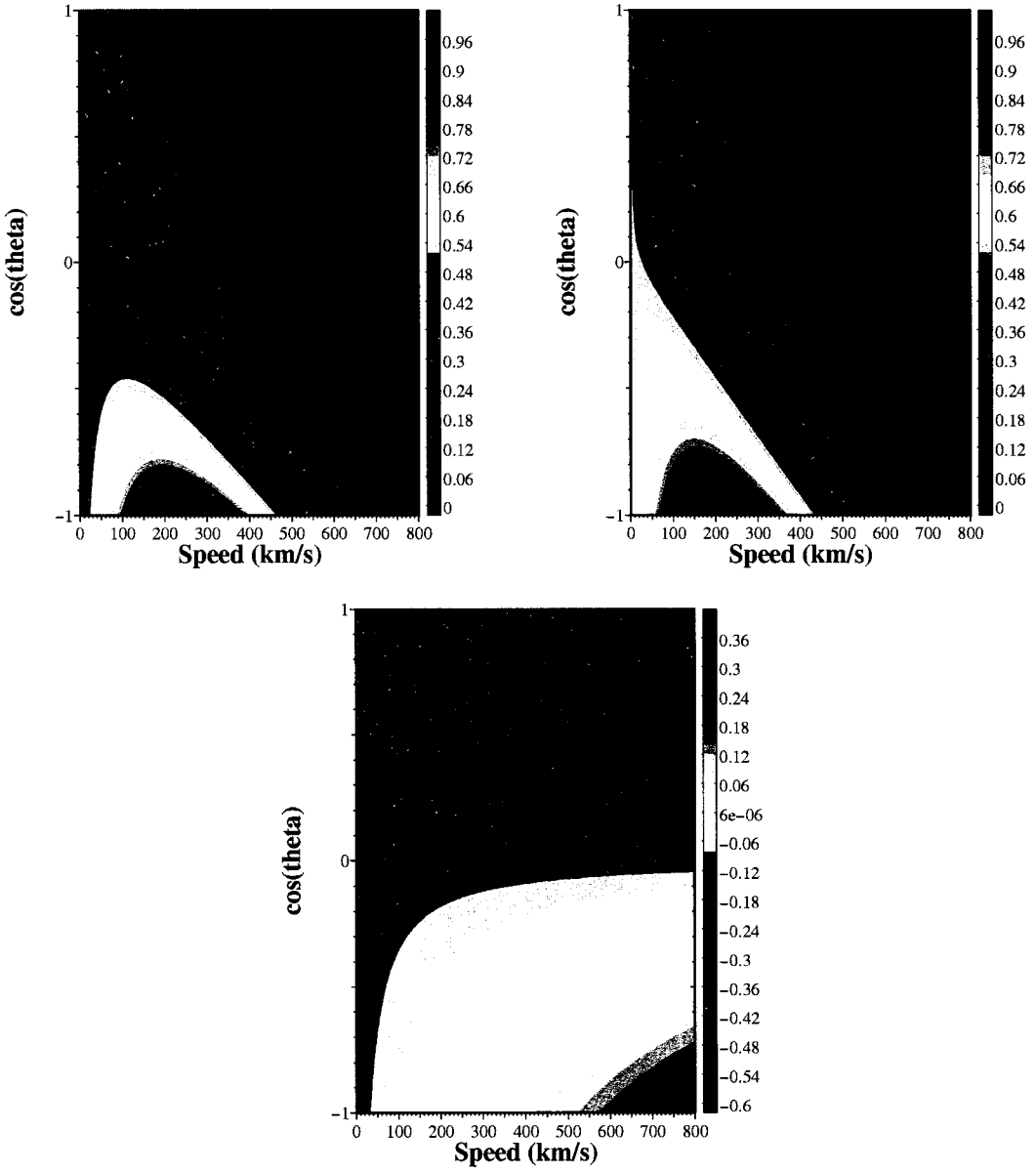

Figure 7.8: **Top**: Directional axion spectra for June (left) and December (right) in units of the peak June detection rate. **Bottom**: The seasonal modulation factor for the above spectra.

In order to clearly illustrate the annual modulation of the detection rates, the seasonal variation of the detection rate, defined in equation (7.6), is shown in the lower half of Figure 7.8. As in the speed distribution modulation (Figure 7.7), the most pronounced modulation occurs at the highest speeds. However, there is very little variation at low speeds for any angle of encounter.

In a smooth halo, directionally-sensitive detectors would be highly biased towards particles which appear to be coming from the forward direction (moving in a direction 180° relative to the Earth's motion). Since the Earth's speed through the Galactic halo is comparable to the velocity dispersion in the halo itself, it is very difficult to have particles "catch-up" to the Earth from behind with any significant speed. This is visible in Figure 7.8 where the detection rate falls rapidly for angles less than 90° (or $\cos\theta > 0$).

The seasonal effects are most pronounced however, when the net flux of axions arriving from a given direction on the sky is considered. The total event rate arriving from direction (b, l) in the sky is given by integrating over all speeds in that direction.

$$F(b,l) = \int_0^\infty \frac{1}{\pi^{3/2} v_0^3} e^{-(v_{DE}^2 + v_{EG}^2 + 2 v_{DE} v_{EG} \cos\theta)/v_o^2} v_{DE}^2 dv_{DE} \tag{7.10}$$

$\cos\theta$ is related to the direction of the detected particle and the direction of the Earth's motion, (b', l'), via

$$\cos\theta = \cos b \cos l \cos b' \cos l' + \cos b \sin l \cos b' \sin l' + \sin b \sin b' \tag{7.11}$$

Figure 7.9 shows the net axion flux arriving from different parts of the sky. The peak is clearly in the direction of the Sun's motion, however the exact location and intensity shifts as the Earth orbits the Sun. The decrease in peak intensity in December is accompanied by an increase in detections throughout the remainder of sky. From Figure 7.8, this increase in flux is from lower velocity axions with speeds of about 200 km s^{-1}.

However, even with the seasonal modulation, if the halo is correctly described by a Maxwellian distribution, an axion detector would be dominated by particles

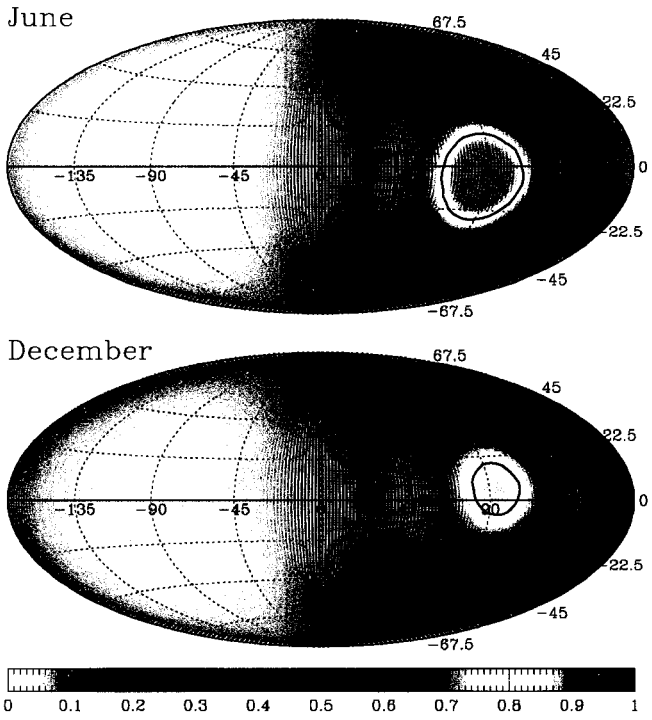

Figure 7.9: Sky plot for the net direction rate of axions arriving from a given direction in a smooth Maxwellian halo in June (upper plot) and December (lower plot) normalized to the peak June rate.

from in front of the Earth with very few detection of axions parallel to the Earth's motion.

7.3.2 WIMP Detectors

The analysis of WIMP detection is more complicated than for axion detection experiments. Since WIMP detectors are based upon the scattering of WIMPs off detector nuclei, there is a random scattering angle involved. Therefore, the detection rate must involve an integral over all possible scattering angles. As shown in Jungman et al. (1996, and references therein), the detection rate for WIMPs is given by

$$\frac{dR}{dQ} = \frac{\sigma_0 \rho_0}{2 m_\chi m_r^2} F^2(Q) \int_{v_{\min}}^{\infty} \frac{f_1(v)}{v} dv \tag{7.12}$$

where σ_0 is the scattering cross-section, ρ_0 is the local density of WIMPs, m_χ is the mass of the WIMP, $m_r = m_\chi m_N/(m_\chi + m_N)$ is the reduced mass, and m_N is the mass of the nucleus in the detector. Finally, $v_{\min}$ is the minimum velocity of a WIMP which could deposit an energy of Q into the detector:

$$v_{\min} = \sqrt{\frac{Q m_N}{2 m_r^2}} \tag{7.13}$$

For example, in a germanium-based detector ($m_N = 68.5$ GeV), if an energy of 100 keV is detected and a WIMP mass of 50 GeV is assumed, the minimum speed which the WIMP could have had is 607 km s^{-1}.

For the Maxwellian speed distribution from equation (7.8), the detection rate can be evaluated analytically:

$$\frac{dR}{dQ} = \frac{\sigma_0 \rho_0}{2 m_\chi m_r^2} F^2(Q) \frac{1}{2 v_{EG}} \left[\mathrm{erf}\left(\frac{v_{\min} + v_{EG}}{v_0} \right) - \mathrm{erf}\left(\frac{v_{\min} - v_{EG}}{v_0} \right) \right] \tag{7.14}$$

Figure 7.10 illustrates the expected detection rate (in arbitrary units) of an ideal WIMP detector for June and December. As with axion detectors, the variation of the Earth's speed in the Galaxy causes a shift in the detected recoil rates with a decrease in high energy events in December. Figure 7.11 highlights this seasonal

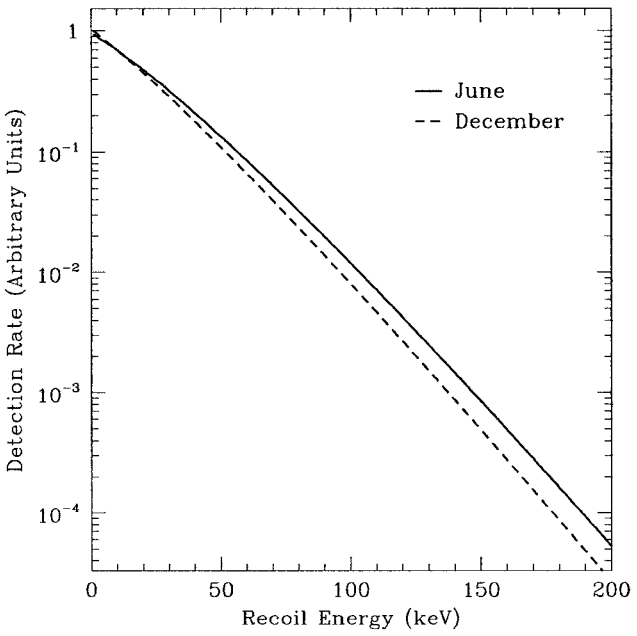

Figure 7.10: Seasonal effect due to the Earth's motion on WIMP detection in a smooth halo. Moving into the halo in June increases the detection rate compared to December for all but the lowest recoil energies.

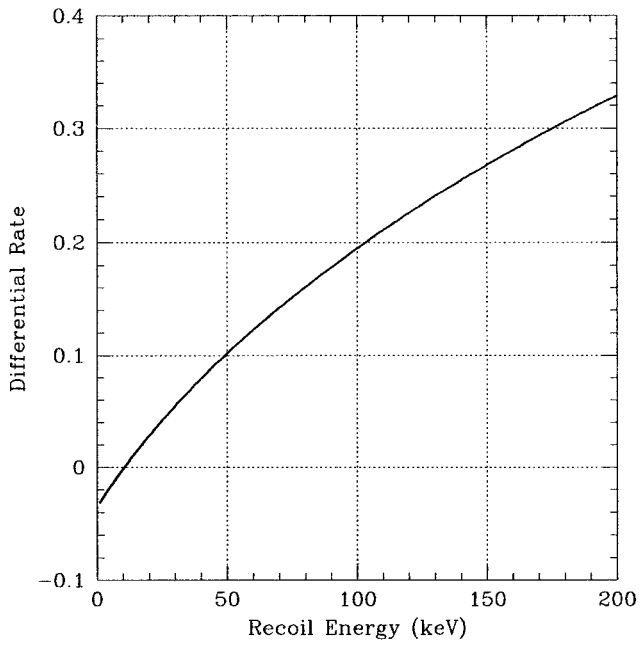

Figure 7.11: The seasonal modulation factor for WIMP detection experiments.

variation by plotting the seasonal modulation factor.

The design of directionally-sensitive WIMP detectors is further advanced than for directionally-sensitive axion detectors. Several experiments are currently underway or in development to record not only the recoil energy of the WIMP, but also its direction.

The one-dimensional velocity distribution in equation (7.12) can be expanded to yield

$$\frac{dR}{dQ} = \frac{\sigma_0 \rho_0}{2 m_\chi m_r^2} F^2(Q) \int_{v_{\min}}^{\infty} \int_0^{\pi} \int_0^{2\pi} f(\vec{v}) v d\phi \sin\theta d\theta dv \tag{7.15}$$

The differential detection rate for a given direction is then

$$\frac{d^2R}{dQ d\cos\theta} = \frac{\sigma_0 \rho_0 \pi}{m_\chi m_r^2} F^2(Q) \int_{v_{\min}}^{\infty} f(v,\theta) v dv \tag{7.16}$$

For the usual Maxwellian distribution, this can be evaluated to give the angular-dependent recoil spectrum:

$$\frac{d^2R}{dQ d\cos\theta} = \frac{\sigma_0 \rho_0 \pi}{2 v_o m_\chi m_r^2} F^2(Q) \exp\left(-\frac{v_{\mathrm{EG}}^2}{v_o^2}\right) \times$$

$$\left[v_{\rm EG}\cos\theta\sqrt{\pi}\exp\left(\frac{v_{\rm EG}^2\cos^2\theta}{v_o^2}\right)\left(\mathrm{erf}\left(\frac{v_{\rm min}+v_{\rm EG}\cos\theta}{v_o}\right)-1\right)\right.$$
$$\left.+v_o\exp\left(-\frac{v_{\rm min}^2+2v_{\rm EG}v_{\rm min}\cos\theta}{v_o^2}\right)\right] \quad (7.17)$$

where θ is the direction of the arriving WIMP relative to the Earth's motion, not the angle of recoiled nuclei.

The top portion of Figure 7.12 shows the directional WIMP recoil spectrum for June and December. The contours are logarithmic spanning 25 orders of magnitude! Therefore, as with the axion spectra, the vast majority of events would occur from WIMPs travelling against the Earth's motion. The highest event rate would occur for small recoil energies since WIMPs of all velocities can contribute. The contours shift slightly between the June (left) and December (right) spectra. This variation is illustrated by the seasonal variation factor shown in the lower portion of the Figure.

The origin of WIMPs in the sky will be the same as for axions shown in Figure 7.9 since it is simply a measure of the net flux of particles. Therefore, if the smooth virialized halo model is correct, almost all detected particles should be travelling against the Earth's motion with only a small probability of low energy events arriving from behind.

7.4 N-body Results

The results from the reverse-run cosmological simulation from Chapter 6 are in the form of a Monte-Carlo representation of the distribution function, not a smooth analytic function. In order to compare the results of the N-body simulation with the analytic models from the previous section, numerical routines must be developed to simulate the observation of axions and WIMPs.

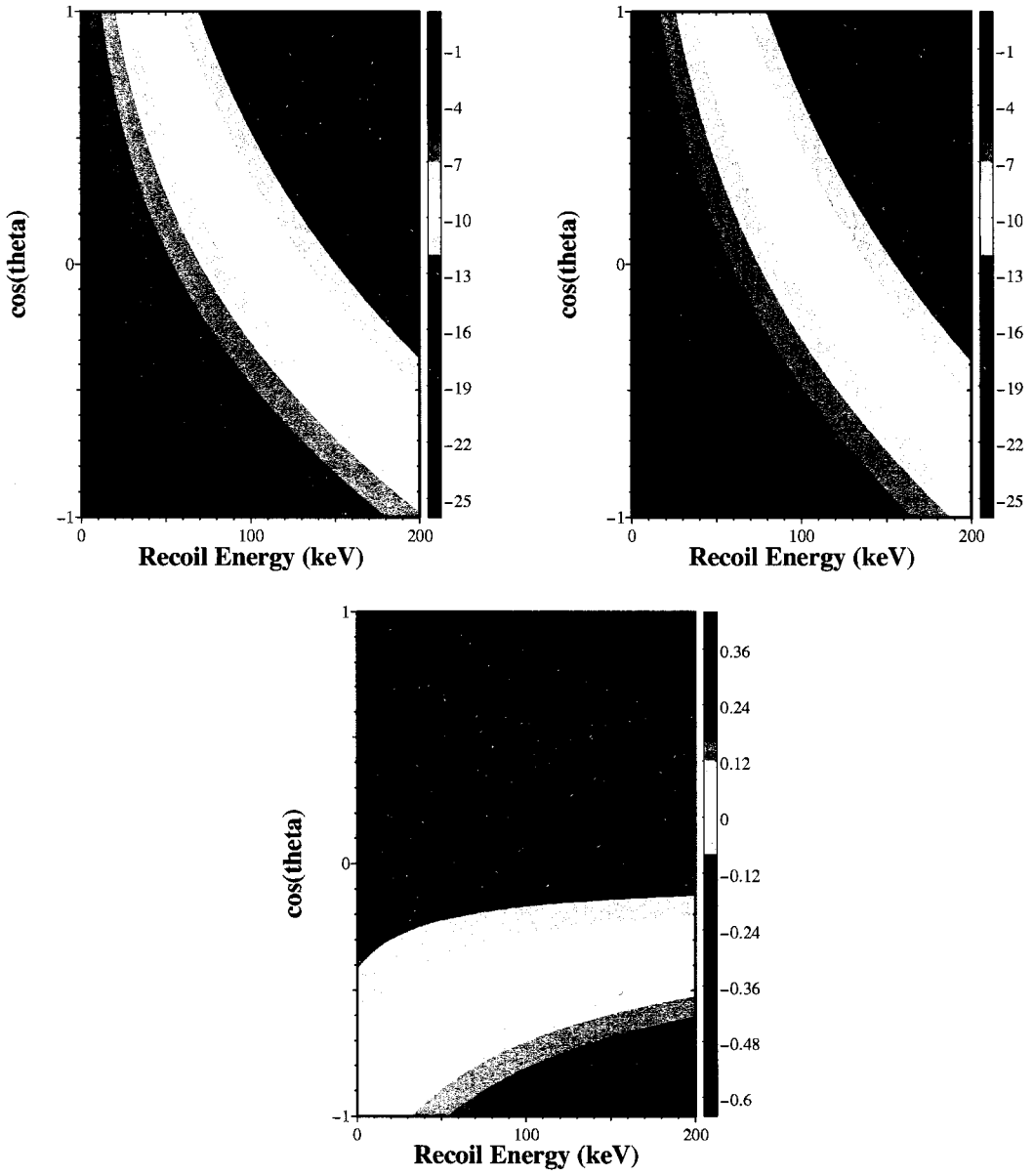

Figure 7.12: **Top**: Recoil spectra for an ideal directionally-sensitive WIMP detector for June (left) and December (right). The contours are *logarithmic* so from dark red (highest detection rates) to dark blue (lowest detection rates) they span 25 orders of magnitude. **Bottom**: The seasonal modulation factor for an ideal directionally-sensitive WIMP detector clearly show the bias towards higher velocity particles. Note the contours are linear in this figure.

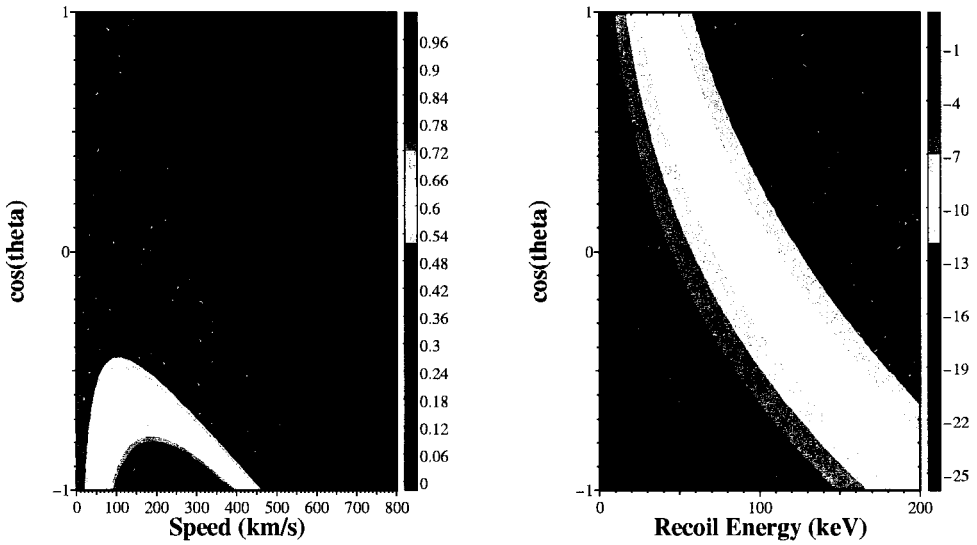

Figure 7.13: Directional detection spectra for axions (left) and WIMPs (right) from a numerical realization of a Maxwellian distribution. Contours are as in Figures 7.8 and 7.12 respectively.

7.4.1 Numerical Analysis Routines

In order to verify the analysis routines, a numerical representation of the Maxwellian distribution used for the analytic plots was generated. This N-body Maxwellian was then analyzed using the same routines that will be used for the cosmological results. Figure 7.13 shows the predicted detection rates for direction-sensitive axion (left panel) and WIMP (right panel) experiments. In both cases, the June spectrum was analyzed. These figures agree with the analytic models presented in Figures 7.8 and 7.12, providing confidence that any effects seen in the cosmological simulation results are truly representative of the distribution of the dark matter, and not an interpretation issue.

In addition to the axion and WIMP detection spectra, the directional sky plots of the origin of dark matter are important. Figure 7.14 illustrates the direction of incoming dark matter realized from the numerical Maxwellian distribution. It agrees with the analytic model shown in Figure 7.9.

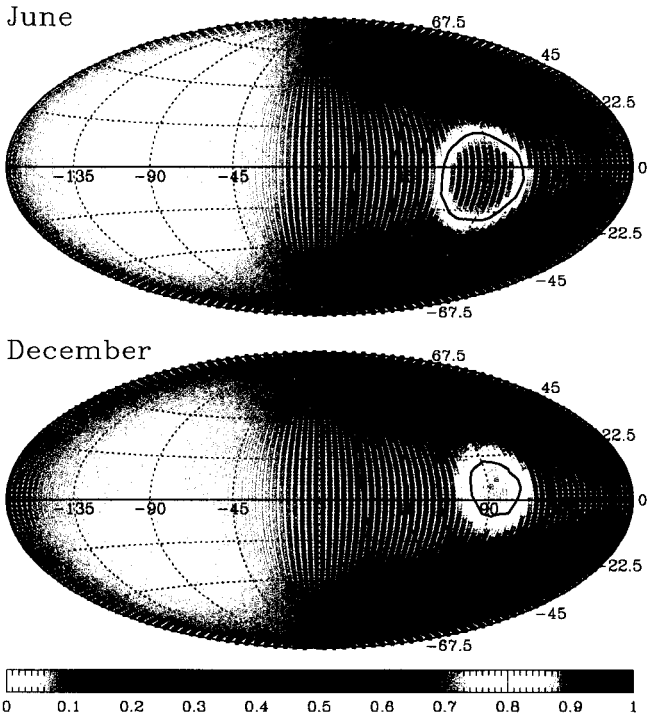

Figure 7.14: Sky view of dark matter flux from a numerical Maxwellian distribution. The projection is normalized to the peak June rate.

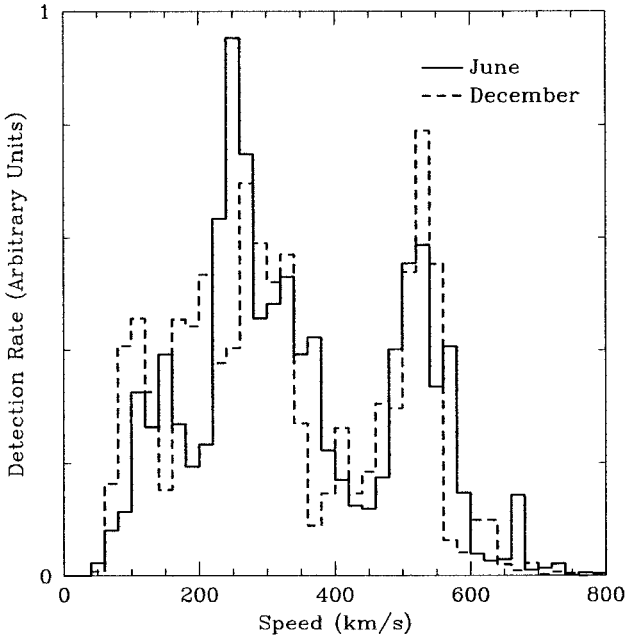

Figure 7.15: Axion detection spectra from the cosmological simulation of Chapter 6. The solid line shows the spectrum in June, while the dashed line is the same distribution but for December.

7.4.2 Axion Detectors

Since axion detectors directly measure the speed distribution of the particles, it is straightforward to calculate the axion detection spectra from the cosmological simulation results from Chapter 6. Figures 7.15 and 7.16 show the detection spectra for June and December, and seasonal modulation factor respectively. The spectra have a general form as due to the Maxwellian distribution with the detection rate rising from $v = 0$, peaking around $v = 300 - 400$ km s^{-1}and falling to 0 by 800 km s^{-1}. However, there are significant differences. Most importantly are the many localized peaks in the distribution. These are streams or partial shells of matter which are not in virial equilibrium with the rest of the dark matter in the solar neighbourhood. As the Earth orbits about the Sun, the changing relative velocity between the terrestrial detector and dark matter causes the locations of some of

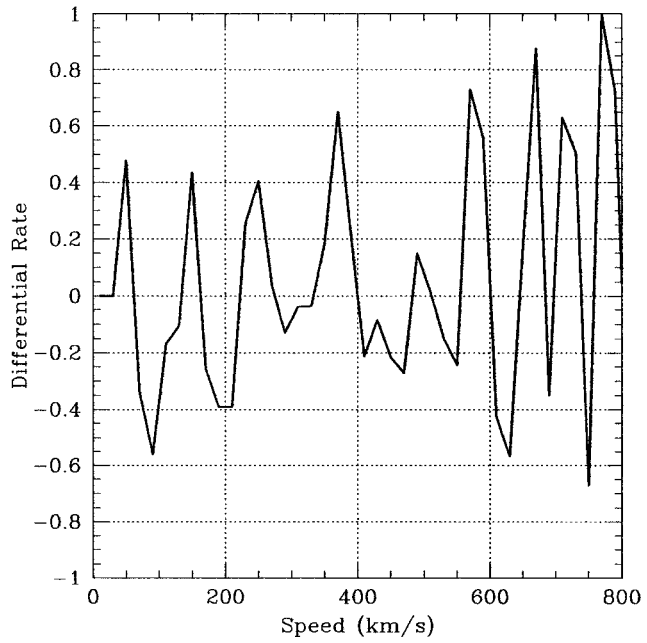

Figure 7.16: The seasonal modulation factor, as defined in 7.6, highlights the differences between the June and December spectra from the N-body data.

the peaks to shift. The amount of variation in the location of the peak yields some dynamical information about the streams of dark matter. For example, if a peak shows no or very little seasonal variation, the dark matter stream must be oriented roughly perpendicular to the plane of the Earth's orbit. A large seasonal variation indicates that the stream must be parallel to the Earth's orbit. The seasonal modulation factor also shows clear signs of the streaming nature of the dark matter. As the location of the peaks moves, it results in a large seasonal change in detection rates over a small range of speeds.

The differences between the assumed smooth Maxwellian distribution and the N-body results are more pronounced in the direction-sensitive axion spectra. Figure 7.17 shows the directional dependence of the axion signal for the N-body results. Though the general trend of a higher range of detected speeds near $\cos\theta = -1$, and only small velocities near $\cos\theta = 1$ is still visible, instead of the smooth variations

seen in the analytic model in Figure 7.8, the reverse-run spectra consists of many small, isolated features. This clearly shows that a large portion of the material is not smoothly distributed but instead resides in streams or clumps which are passing through the solar neighbourhood.

The differences between the June and December spectra are also much more pronounced. This gives rise to the rapidly varying seasonal modulation factor shown in the lower half of Figure 7.17. The seasonal modulation factor has almost extreme values (± 1) for a wide variety of speeds and angles. Since the seasonal modulation is caused by the change in velocity and angles of a dark matter stream during the year, large variation in the seasonal modulation factor usually occurs in pairs. Many of the small isolated features in the directional spectra appear as a pair of nearby points where one has a value of $\mathcal{F} = +1$, while the other has $\mathcal{F} = -1$. This arises simply due to the change in $\cos\theta$ and v of the stream between June and December and the lack of any nearby streams to mask the variation.

The prominent features visible in the directional axion spectra can be confirmed to be streams by looking at the origin of the axions in the sky. Figure 7.18 shows the intense features from the directional axion spectra are visible in the sky plot of the N-body results as concentrated points. Figure 7.18 also clearly illustrates that, as in the smooth analytic models, the majority of detection events will be of particles travelling against the Earth's motions. However, the maximum detection rates are no longer directly ahead of the Earth. In this realization of the Milky Way, the maximal signals would be arriving from closer to the Galactic poles than from straight ahead. However, it should be noted that the simulation from Chapter 6 is only one random model of the Milky Way and a slightly different simulation could yield streams arriving from different directions. Nonetheless, the qualitative nature of the stream-dominated dark matter distribution, rather than a smooth Maxwellian distribution, would still remain. For example, if the Sun's motion is assumed to be in a different randomly chosen direction in the Galaxy, the location of peaks in the

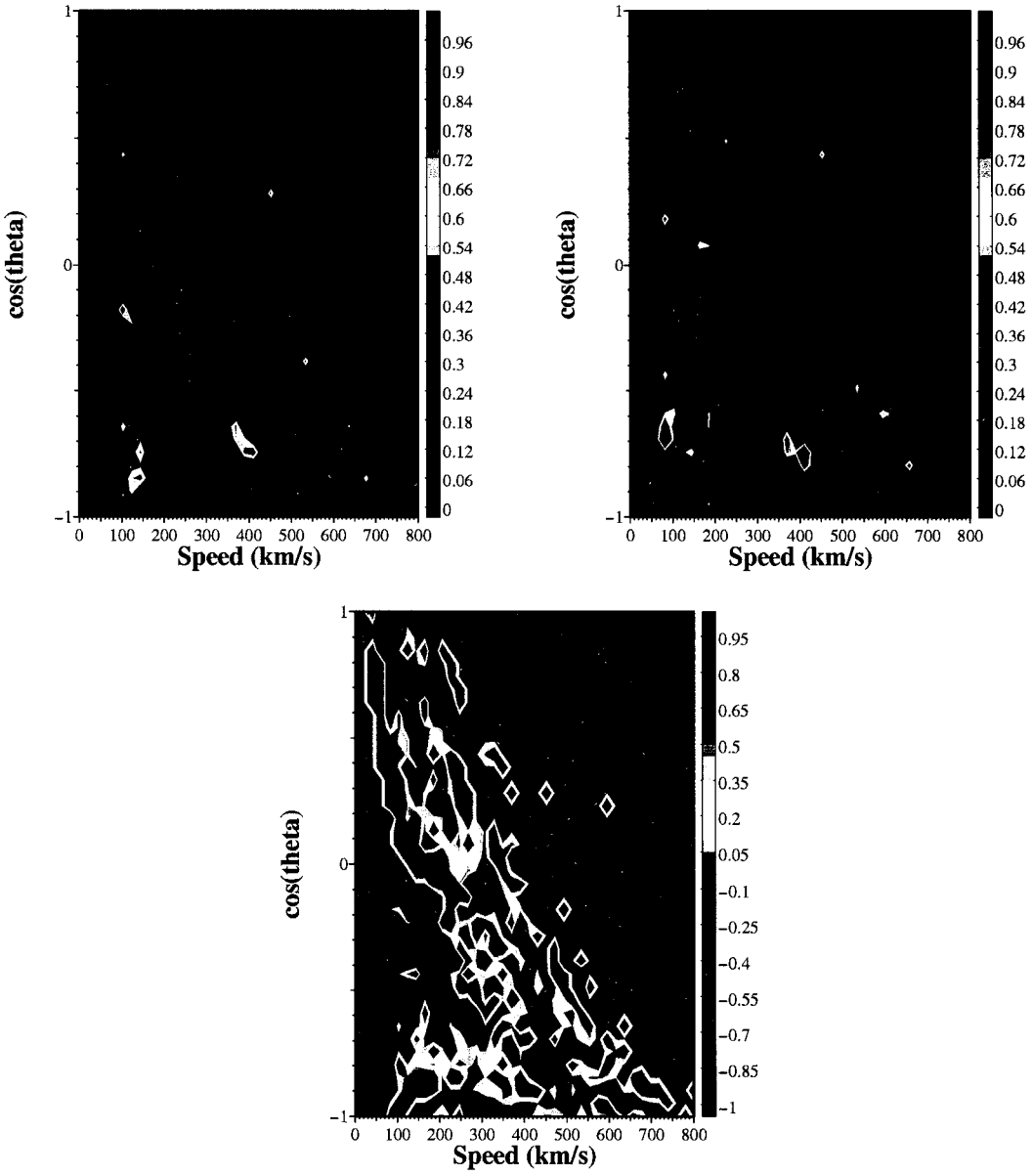

Figure 7.17: **Top**: Directionally-sensitive axion spectra for the results from the N-body simulation of Chapter 6 in June (left) and December (right). Contours are as in Figure 7.8. **Bottom**: The seasonal modulation factor for the above spectra. Note the rapid variation in both speed and angle.

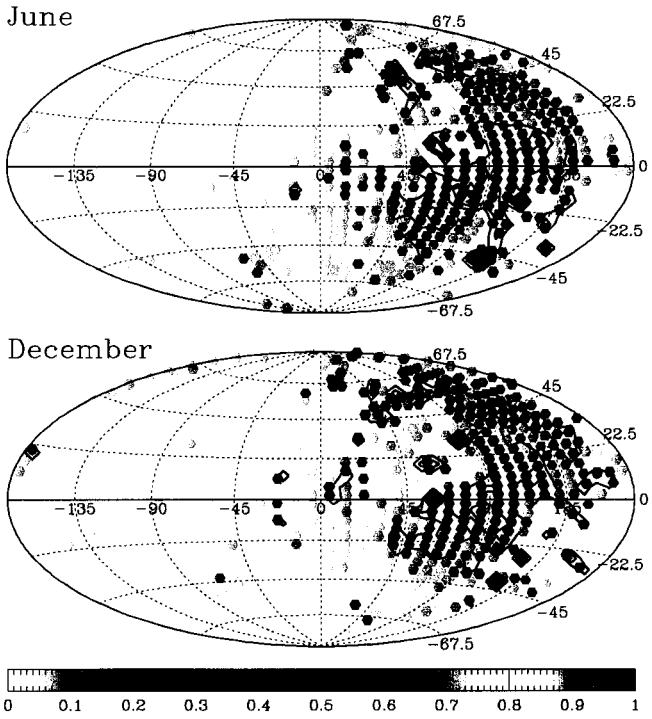

Figure 7.18: Sky plot for the direction of origin of axions from the N-body simulation in June (upper plot) and December (lower plot).

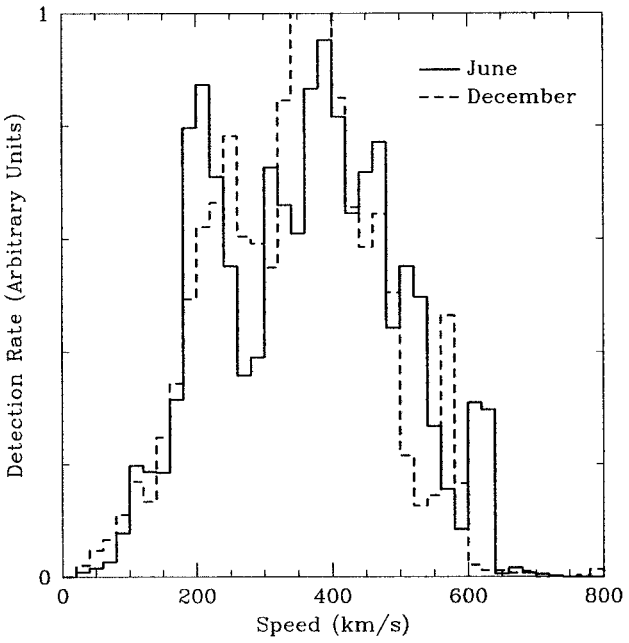

Figure 7.19: Axion detection spectra from the cosmological simulation of Chapter 6 assuming a different direction of the Sun than in Figure 7.15. The solid line shows the spectrum in June, while the dashed line is the same distribution but for December.

speed distribution shift, but the qualitative nature of the distribution remains the same. Figure 7.19 shows the same dark matter distribution from Figure 7.15 but the Sun's motion was assumed to be in a different direction. The peaks in the spectrum remain, but their location shifts.

7.4.3 WIMP Detectors

An analysis of the cosmological reverse-run simulation for WIMP detections is slightly more complicated than for axion detection experiments since it involves an integral over all velocities above the minimum value. Nonetheless, it can be computed through a straightforward application of equation (7.12) with the integral performed numerically. Figure 7.20 shows the June (solid line) and December

(dashed line) recoil spectra for a germanium detector ($m_N = 68.5$ GeV) and a 50 GeV WIMP. At low recoil energies, the general trend of both spectra is very similar to that of the smooth distribution shown in Figure 7.10 (and as indicated by the long dashed line in Figure 7.20). However, the N-body spectrum has numerous bumps and changes in slope. This is due to the inhomogenous nature of the dark matter distribution. In particular, at higher recoil energies the recoil spectrum becomes quite "step-like". This is due to the fact that streams of uniform velocity (i.e. streams where the velocity dispersion within the stream is small compared to its bulk motion) have a maximum energy that they can contribute to the recoil spectrum. This results in a sharp truncation of the recoil energy spectrum at the maximum transferable energy of the stream. Therefore, the several steps at higher recoil energy in the spectrum indicate that at high velocities, the dark matter distribution is dominated by streams of particles, rather than a smooth distribution.

The seasonal modulation of the recoil spectra, shown in Figure 7.21, also clearly differs from the smooth transitions in the Maxwellian distribution. While at low energies, it varies somewhat smoothly, at high energies it varies rapidly. This is related to the conclusion that the dark matter distribution is dominated by streams at higher velocities. As the Earth orbits the Sun, the relative velocity between the stream and the detector will change causing the maximum energy deposited in the detector to vary. This is clearly visible for the large stream with a maximum recoil energy of approximately 130 kev in June, but which falls to about 110 kev in December. This causes a very large seasonal modulation in this range of energies.

As in the case of the axion spectra, the one-dimensional spectra provide hints of underlying structure in the velocity-space distribution of the dark matter, but cannot yield too many specific details. The directionally-sensitive plots of the WIMP detection rates from the cosmological simulation (Figure 7.22), can be used to extract more information about the nature of the dark matter distribution. The first thing to note is that the same general properties exist in the N-body spectra and the

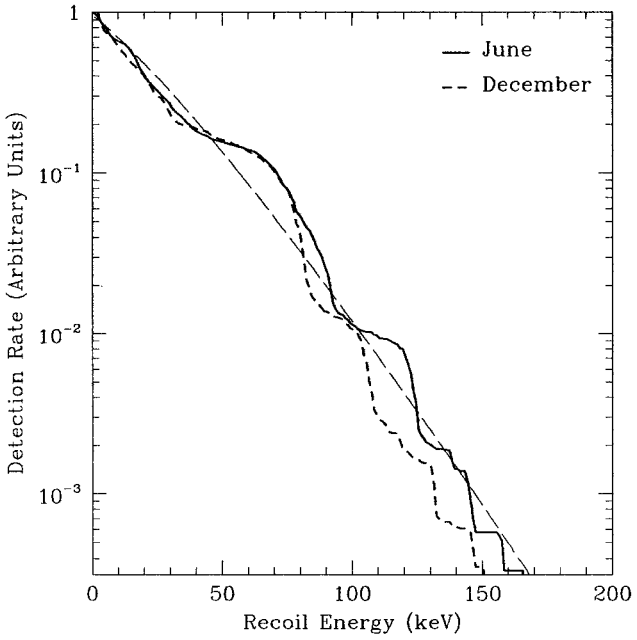

Figure 7.20: The June and December WIMP recoil spectrum from the N-body results. For comparison, the June detection rate for a Maxwellian halo is shown with the long dashed line.

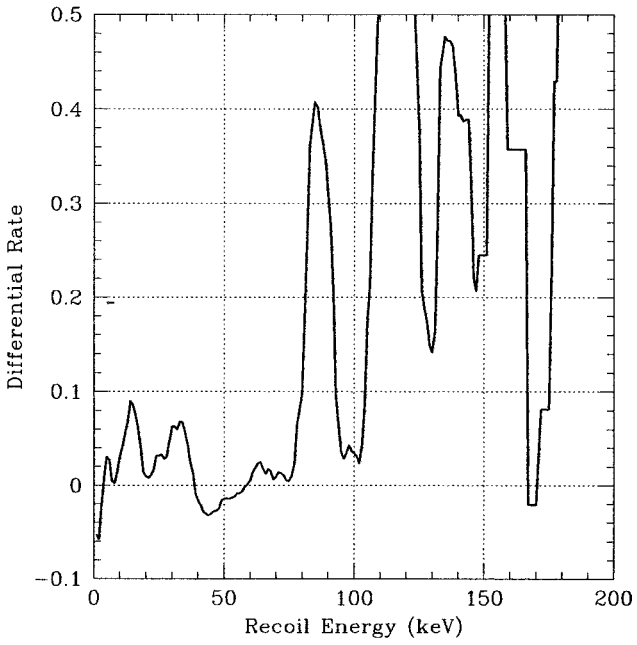

Figure 7.21: The seasonal modulation rate for WIMP detection experiments.

analytic spectra. In general, the higher event rates occur at low recoil energies and for WIMPs which have large angles between their motion and the Earth's. However, the highest detection rates do not occur at 180°, but instead in a variety of regions elongated in the speed direction spanning small ranges of angles. This is similar to most features in the figure which extend from $Q = 0$ to a maximum Q at almost constant θ. This is another signature of the stream-like nature of the dark matter distribution. If a stream exists at a given angle, θ_0, to the Earth's motion with an energy of Q_0, it would appear in the directional WIMP plot as a horizontal line at θ_0 extending up to Q_0. The several dominant streams found in the axion spectrum in Figure 7.17 and visible in the sky projection (Figure 7.18) are also visible in the directional WIMP recoil spectrum.

The streams in the directional WIMP spectra are emphasized in the seasonal modulation signal (lower half of Figure 7.22). As the relative speed and direction of the Earth changes slightly throughout the year, two effects arise. The first is that the

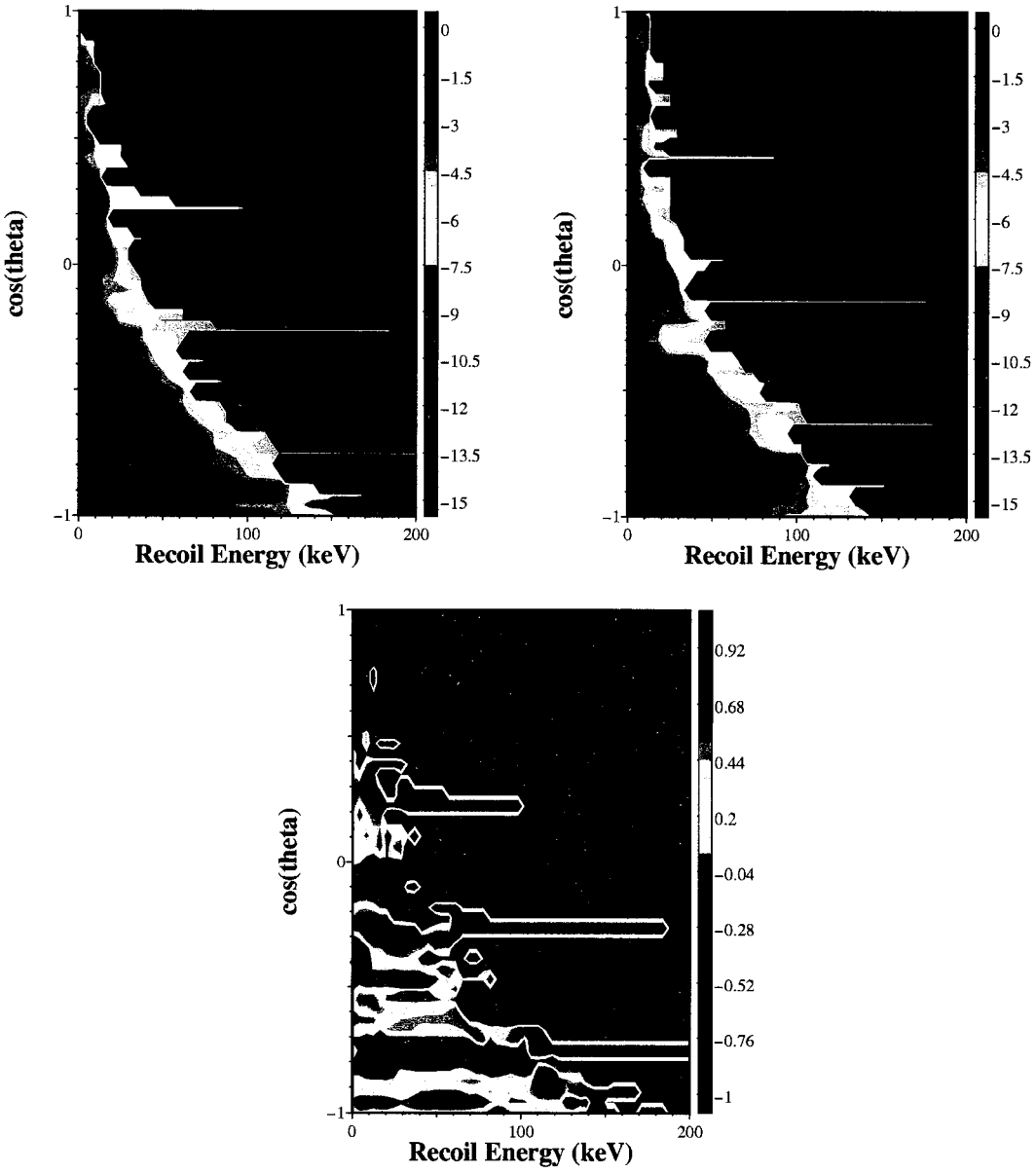

Figure 7.22: **Top**: Directional WIMP recoil spectra for June (right) and December (left). Note the contours are logarithmic and span 15 orders of magnitude. **Bottom**: The seasonal modulation factor for the above spectra. The contours are linear between ± 1.

length of the feature changes due to the dependence of Q_0 upon the relative speed between the Earth and the WIMP. This results in a large seasonal modulation at higher energies and very little change at lower energies for a given θ. A second effect arises if there is a change in angle between the direction of the Earth and the direction of the WIMPs throughout the year. If the change is large enough, it can result in the entire feature moving up or down in θ. In the seasonal modulation figure, this appears as a long horizontal line of enhanced variation.

Note that the current generation of directionally-sensitive WIMP detectors have very low angular resolution, and in fact, measure the direction of the nuclear recoil, not the direction of the incoming WIMPs. Therefore, due to the random scattering events in the detector and the uncertainty about properties of the incoming WIMPs, the direction of origin cannot be well determined. (However, Gondolo (2002) has shown that it is possible in principle to reconstruct the WIMP velocity distribution from only the nuclear recoils.) Nonetheless, directional sensitivity in detectors serves two important purposes. The first is background discrimination. In the directional spectrum of both the smooth Maxwellian distribution and the N-body results, very few WIMPs arrive from behind the Earth. Background events, such as neutron interactions and nuclear decays which should show no directional bias, would dominate the detection spectra for directions much less than 90°. This background would be random in direction and could be subtracted from the other half of the spectrum to yield the actual WIMP interaction rate. However, this technique implicitly assumes that the detection rate at higher angles is much greater than at lower angles. It is possible that a stream of dark matter could be arriving from behind. This illustrates the second advantage of a directional detector. If there are correlations in any direction of the recoiled nuclei, it could still be used distinguish to true WIMP recoils from background events.

8. CONCLUSIONS

The standard assumption that dark matter is thoroughly virialized in a smooth Maxwellian distribution does not withstand either of the investigation techniques presented. Both the semi-analytic modelling from Chapter 4 and the reverse-run technique from Chapters 5 and 6 indicated that the local component of dark matter will have at least a small streaming component due to recent merger events, and could in fact have a large amount of velocity-space substructure.

The semi-analytic model showed that a small portion of the local complement of dark matter likely arose from recent merger events. This dark matter would have a velocity significantly higher than the typical velocities in the solar neighbourhood giving rise to inhomogeneities in the measured velocity distribution. Since the dark matter stream arose from a relatively recent merger event, the speed of the dark matter as it passes through the solar neighbourhood is significantly above the typical circular or virialized velocities.

To further investigate the possibility of velocity-space substructure, the "reverse-run" technique was developed. One requirement for the reverse-run is that a traditional N-body simulation must be reversible. It was shown in Chapter 3 that reversibility and the integrity of phase-space structures are tightly linked. In order for the system to be reversible, the evolution of the phase-space distribution must be correctly followed. A simple solution to minimize the breaking of the phase-space sheet in CDM simulations is to use sufficient softening in the simulation. It was shown that one must use a softening length of approximately 1/4 the initial grid spacing of the particles in order to properly maintain the integrity of the phase-space sheet.

In order to implement the reverse-run method, a new numerical code was developed based upon the multipole expansion method of Dehnen (2000). The new code is reversible, allows test particles, and incorporates periodic boundary conditions for full cosmological simulations. A simulation which is similar to the Milky Way and M31 was designed and the velocity-space distribution at a point resembling the solar neighbourhood was analyzed using the reverse-run technique. The results showed that there is a significant amount of velocity-space substructure in the vicinity of the simulated Milky Way.

The effect of velocity-space substructure was shown to have significant impact on terrestrial dark matter detection experiments. Rather than the smooth continuous spectra expected from the smooth halo assumption, the substructure creates numerous features in both the axion and WIMP spectra. The axion speed distribution consisted of numerous peaks and it was shown that these are concentrated streams of dark matter originating from small locations in the sky. As the Earth orbits the Sun, the seasonal motion causes the intensity of the streams and their direction relative to the Earth to change, yielding strong seasonal variations in the spectra. Due to the random scattering angles involved in WIMP detection, substructure tends to become washed out in the simple bolometric detectors. There were signs of substructure in the non-directional spectra but not as prominent as in the axion spectra. However, directional WIMP detectors, with low backgrounds, would clearly see the substructure and significant seasonal modulation.

As dark matter detectors become more advanced, and possibly begin to detect unambiguous signals of dark matter particles, the issue of velocity-space substructure will become of vital importance. Even in the absence of any confirmed detections, the limits placed upon dark matter candidates may be overly restrictive without considering the existence of streams and clumps of dark matter. Incorrect assumptions about the local distribution of dark matter could lead one to completely misinterpret the signal (or lack thereof) and arrive at erroneous conclusions about

the nature of the predominant form of matter in the universe.

8.1 Future Work

While the studies undertaken here indicate that the velocity-space distribution of dark matter in the solar neighbourhood is not smooth, and this inhomogeniety would have significant impact upon dark matter experiments, there is still the possibility to extend this work. One important task to undertake is to perform a higher resolution cosmological simulation which better mimics the Local Group and has sufficient accuracy to probe closer to the Galactic centre.

An equally important extension of this work is to incorporate realistic detector models into the expected detection spectra. All spectra presented here, both non-directional and directional, assume ideal detectors with arbitrarily high resolution. In practice, detectors are non-ideal with experimental uncertainties and limited resolution. Such restrictions on the quality of the obtainable data may impede the ability to identify velocity-space substructure in the local dark matter distribution.

Finally, another interesting pursuit would be to examine one's ability to reconstruct the full dynamical properties of dark matter streams from observed detection spectra. If the streams can be completely quantified, it may be possible to associate them with local stellar streams or probe the exact details of the formation history of the Milky Way.

REFERENCES

Abrams, D., et al. Exclusion limits on the WIMP-nucleon cross section from the Cryogenic Dark Matter Search. *Phys. Rev. D*, **66**, 122003 (2002)

Afonso, C., et al. Bulge microlensing optical depth from EROS 2 observations. *Astr. & Astrophys.*, **404**, 145 (2003)

Ahmad, Q. R. and et al. Measurement of the Rate of $\nu_e + d \rightarrow p + p + e^-$ Interactions Produced by ^8B Solar Neutrinos at the Sudbury Neutrino Observatory. *Physical Review Letters*, **87**, 071301 (2001)

Alcock, C., et al. The MACHO Project: Microlensing Optical Depth toward the Galactic Bulge from Difference Image Analysis. *Astrophys. J.*, **541**, 734 (2000)

Alves, D. R., et al. MEGA: Microlensing and Variable Stars in M31. *American Astronomical Society Meeting*, **201** (2002)

Asztalos, S., et al. Large-scale microwave cavity search for dark-matter axions. *Phys. Rev. D*, **64**, 92003 (2001)

Asztalos, S. J., et al. Experimental Constraints on the Axion Dark Matter Halo Density. *Astrophys. J. Lett.*, **571**, L27 (2002)

Avignone, F. T., et al. Solar axion experiments using coherent Primakoff conversion in single crystals. *Nuclear Physics B Proceedings Supplements*, **72**, 176 (1999)

Bagemihl, F. On indecomposable polyhedra. *The American Mathematical Monthly*, **55**, 411 (1948)

Barnes, J. and Hut, P. A Hierarchical O(NlogN) Force-Calculation Algorithm. *Nature*, **324**, 446 (1986)

Begeman, K. G., Broeils, A. H., and Sanders, R. H. Extended rotation curves of spiral galaxies - Dark haloes and modified dynamics. *Mon. Not. R. Astr. Soc.*, **249**, 523 (1991)

Belli, P., Cerulli, R., Fornengo, N., and Scopel, S. Effect of the galactic halo modeling on the DAMA-NaI annual modulation result: An extended analysis of the data for weakly interacting massive particles with a purely spin-independent coupling. *Phys. Rev. D*, **66**, 43503 (2002)

Bergstroem, L. Non-baryonic dark matter: observational evidence and detection methods. *Reports of Progress in Physics*, **63**, 793 (2000)

Bernabei, R., et al. Results with the DAMA/NaI(Tl) experiment at LNGS. *Nuclear Physics B Proceedings Supplements*, **110**, 61 (2002)

Bershady, M. A., Ressell, M. T., and Turner, M. S. Telescope search for a 3-eV to 8-eV axion. *Physical Review Letters*, **66**, 1398 (1991)

Bildhauer, S., Buchert, T., and Kasai, M. Solutions in Newtonian cosmology - The pancake theory with cosmological constant. *Astr. & Astrophys.*, **263**, 23 (1992)

Binney, J. and Tremaine, S. *Galactic dynamics*. Princeton, NJ, Princeton University Press, 1987, 747 p. (1987)

Bond, J. R., Cole, S., Efstathiou, G., and Kaiser, N. Excursion set mass functions for hierarchical Gaussian fluctuations. *Astrophys. J.*, **379**, 440 (1991)

Bonn, J., et al. The Mainz Neutrino Mass Experiment. *Nuclear Physics B Proceedings Supplements*, **91**, 273 (2001)

Bower, R. G. The evolution of groups of galaxies in the Press-Schechter formalism. *Mon. Not. R. Astr. Soc.*, **248**, 332 (1991)

Bunn, E. F. and White, M. The 4 Year COBE Normalization and Large-Scale Structure. *Astrophys. J.*, **480**, 6 (1997)

Côté, P., Mateo, M., Sargent, W. L. W., and Olszewski, E. W. An Improved Mass Determination for M31 from Its Satellite Galaxies. *Astrophys. J. Lett.*, **537**, L91 (2000)

Cantatore, G., et al. First Run of the PVLAS Experiment: Dark Matter Candidates Production and Detection. In *Identification of Dark Matter*, page 481 (2001)

Cole, S. and Lacey, C. The structure of dark matter haloes in hierarchical clustering models. *Mon. Not. R. Astr. Soc.*, **281**, 716 (1996)

Copi, C. J. and Krauss, L. M. Comparing interaction rate detectors for weakly interacting massive particles with annual modulation detectors. *Phys. Rev. D*, **67**, 103507 (2003)

Daw, E. J. Status Report on the Large-Scale U. S. Search for Halo Axions. In *Identification of Dark Matter*, page 487 (2001)

Dehnen, W. A Very Fast and Momentum-conserving Tree Code. *Astrophys. J. Lett.*, **536**, L39 (2000)

Dehnen, W. Towards optimal softening in three-dimensional N-body codes - I. Minimizing the force error. *Mon. Not. R. Astr. Soc.*, **324**, 273 (2001)

Dehnen, W. A Hierarchical O(N) Force Calculation Algorithm. *Journal of Computational Physics*, **179**, 27 (2002)

Dubinski, J. and Carlberg, R. G. The structure of cold dark matter halos. *Astrophys. J.*, **378**, 496 (1991)

EDELWEISS Collaboration, et al. Improved exclusion limits from the EDELWEISS WIMP search. *Physics Letters B*, **545**, 43 (2002)

Eisenstein, D. J. and Hu, W. Baryonic Features in the Matter Transfer Function. *Astrophys. J.*, **496**, 605 (1998)

Evans, N. W. and Wilkinson, M. I. The mass of the Andromeda galaxy. *Mon. Not. R. Astr. Soc.*, **316**, 929 (2000)

Feast, M. and Whitelock, P. Galactic kinematics of Cepheids from HIPPARCOS proper motions. *Mon. Not. R. Astr. Soc.*, **291**, 683 (1997)

Freedman, W. L. and Madore, B. F. An empirical test for the metallicity sensitivity of the Cepheid period-luminosity relation. *Astrophys. J.*, **365**, 186 (1990)

Freese, K., Frieman, J., and Gould, A. Signal modulation in cold-dark-matter detection. *Phys. Rev. D*, **37**, 3388 (1988)

Gaitskell, R. J. Limits on the WIMP-Nucleon Cross-Section from the Cryogenic Dark Matter Search. In *Identification of Dark Matter*, page 349 (2001)

Gelmini, G. and Gondolo, P. Weakly interacting massive particle annual modulation with opposite phase in late-infall halo models. *Phys. Rev. D*, **64**, 23504 (2001)

Ghigna, S., et al. Density Profiles and Substructure of Dark Matter Halos: Converging Results at Ultra-High Numerical Resolution. *Astrophys. J.*, **544**, 616 (2000)

Gondolo, P. Recoil momentum spectrum in directional dark matter detectors. *Phys. Rev. D*, **66**, 103513 (2002)

Gottesman, S. T., Hunter, J. H., and Boonyasait, V. On the mass of M31. *Mon. Not. R. Astr. Soc.*, **337**, 34 (2002)

Grassberger, P. and Procaccia, I. Characterization of strange attractors. *Physical Review Letters*, **50**, 346 (1983)

Green, A. M. Effect of realistic astrophysical inputs on the phase and shape of the WIMP annual modulation signal. *ArXiv Astrophysics e-prints* (2003). `astro-ph/0304446`

Greenside, H. S., Wolf, A., Swift, J., and Pignataro, T. Impracticality of a box-counting algorithm for calculating the dimensionality of strange attractors. *Phys. Rev. A*, **25**, 3453 (1982)

Groom, D., et al. Review of Particle Physics. *The European Physical Journal*, **C15**, 1 (2000)

Helmi, A., White, S. D. M., and Springel, V. The phase-space structure of cold dark matter haloes: insights into the Galactic halo. *Mon. Not. R. Astr. Soc.*, **339**, 834 (2003)

Henriksen, R. N. and Widrow, L. M. Self-Similar Relaxation of Self-Gravitating Collisionless Particles. *Physical Review Letters*, **78**, 3426 (1997)

Hernquist, L. An analytical model for spherical galaxies and bulges. *Astrophys. J.*, **356**, 359 (1990)

Hernquist, L., Bouchet, F. R., and Suto, Y. Application of the Ewald method to cosmological N-body simulations. *Astrophys. J. Supp.*, **75**, 231 (1991)

Hockney, R. W. and Eastwood, J. W. *Computer simulation using particles*. Bristol: Hilger, 1988 (1988)

Hoffman, Y. and Zaroubi, S. Goodness-of-Fit Analysis of Radial Velocity Surveys. *Astrophys. J. Lett.*, **535**, L5 (2000)

Hut, P. and Heggie, D. C. Orbital Divergence and Relaxation in the Gravitational N-Body Problem. *ArXiv Astrophysics e-prints* (2001). `astro-ph/0111015`

Hut, P., Makino, J., and McMillan, S. Building a better leapfrog. *Astrophys. J. Lett.*, **443**, L93 (1995)

Ibata, R., Irwin, M., Lewis, G. F., and Stolte, A. Galactic Halo Substructure in the Sloan Digital Sky Survey: The Ancient Tidal Stream from the Sagittarius Dwarf Galaxy. *Astrophys. J. Lett.*, **547**, L133 (2001)

Ibata, R. A., Gilmore, G., and Irwin, M. J. Sagittarius: the nearest dwarf galaxy. *Mon. Not. R. Astr. Soc.*, **277**, 781 (1995)

Irvine, W. M. Local Irregularities in a Universe Satisfying the Cosmological Principle. *Ph.D. Thesis* (1961)

Ivanov, P., Naselsky, P., and Novikov, I. Inflation and primordial black holes as dark matter. *Phys. Rev. D*, **50**, 7173 (1994)

Jenkins, A., et al. The mass function of dark matter haloes. *Mon. Not. R. Astr. Soc.*, **321**, 372 (2001)

Johnston, K. V., Hernquist, L., and Bolte, M. Fossil Signatures of Ancient Accretion Events in the Halo. *Astrophys. J.*, **465**, 278 (1996)

Jungman, G., Kamionkowski, M., and Griest, K. Supersymmetric dark matter. *Phys. Rep.*, **267**, 195 (1996)

Katz, N. and Gunn, J. E. Dissipational galaxy formation. I - Effects of gasdynamics. *Astrophys. J.*, **377**, 365 (1991)

Kerr, F. J. and Lynden-Bell, D. Review of galactic constants. *Mon. Not. R. Astr. Soc.*, **221**, 1023 (1986)

Klypin, A., Hoffman, Y., Kravtsov, A., and Gottloeber, S. Constrained Simulations of the Real Universe: the Local Supercluster. *ArXiv Astrophysics e-prints* (2001). `astro-ph/0107104`

Lüscher, R., et al. The potential of liquid xenon for WIMP search: the ZEPLIN diagnostic array. *Nuclear Physics B Proceedings Supplements*, **95**, 233 (2001)

Lacey, C. and Cole, S. Merger rates in hierarchical models of galaxy formation. *Mon. Not. R. Astr. Soc.*, **262**, 627 (1993)

Lacey, C. and Cole, S. Merger Rates in Hierarchical Models of Galaxy Formation - Part Two - Comparison with N-Body Simulations. *Mon. Not. R. Astr. Soc.*, **271**, 676 (1994)

Lange, A. E., et al. Cosmological parameters from the first results of Boomerang. *Phys. Rev. D*, **63**, 042001 (2001)

Layzer, D. A Preface to Cosmogony. I. The Energy Equation and the Virial Theorem for Cosmic Distributions. *Astrophys. J.*, **138**, 174 (1963)

Lokas, E. L. and Mamon, G. A. Properties of spherical galaxies and clusters with an NFW density profile. *Mon. Not. R. Astr. Soc.*, **321**, 155 (2001)

Lynden-Bell, D. Statistical mechanics of violent relaxation in stellar systems. *Mon. Not. R. Astr. Soc.*, **136**, 101 (1967)

Mandelbrot, B. B. *The fractal geometry of nature*. San Francisco: W.H. Freeman, 1982, Revised edition of: Fractals (1977) (1977)

Martoff, C. J., Snowden-Ifft, D., Ohnuki, T., and Lehner, M. J. The DRIFT Concept-Sensitive WIMP Dark Matter Search with a Gas Detector. In *The Identification of Dark Matter*, page 389 (1999)

Mateo, M. L. Dwarf Galaxies of the Local Group. *Ann. Rev. Astr. & Astrophys.*, **36**, 435 (1998)

Merritt, D. and Valluri, M. Chaos and Mixing in Triaxial Stellar Systems. *Astrophys. J.*, **471**, 82 (1996)

Moore, B., Governato, F., Quinn, T., Stadel, J., and Lake, G. Resolving the Structure of Cold Dark Matter Halos. *Astrophys. J. Lett.*, **499**, L5 (1998)

Moore, B., et al. Dark matter in Draco and the Local Group: Implications for direct detection experiments. *Phys. Rev. D*, **64**, 063508 (2001)

Navarro, J. F., Frenk, C. S., and White, S. D. M. The Structure of Cold Dark Matter Halos. *Astrophys. J.*, **462**, 563 (1996)

Nusser, A. and Sheth, R. K. Mass growth and density profiles of dark matter haloes in hierarchical clustering. *Mon. Not. R. Astr. Soc.*, **303**, 685 (1999)

Pearce, F. R., Thomas, P. A., and Couchman, H. M. P. Head-On Mergers of Systems Containing Gas. *Mon. Not. R. Astr. Soc.*, **268**, 953 (1994)

Peccei, R. D. and Quinn, H. R. CP conservation in the presence of pseudoparticles. *Physical Review Letters*, **38**, 1440 (1977)

Peebles, P. J. E. *The large-scale structure of the universe.* Research supported by the National Science Foundation. Princeton, N.J., Princeton University Press, 1980. 435 p. (1980)

Peebles, P. J. E. Large-scale background temperature and mass fluctuations due to scale-invariant primeval perturbations. *Astrophys. J. Lett.*, **263**, L1 (1982)

Peebles, P. J. E. *Principles of physical cosmology.* Princeton Series in Physics, Princeton, NJ: Princeton University Press, —c1993 (1993)

Perlmutter, S., et al. Measurements of Omega and Lambda from 42 High-Redshift Supernovae. *Astrophys. J.*, **517**, 565 (1999)

Pfenniger, D., Combes, F., and Martinet, L. Is dark matter in spiral galaxies cold gas? I. Observational constraints and dynamical clues about galaxy evolution. *Astr. & Astrophys.*, **285**, 79 (1994)

Press, W. H. and Schechter, P. Formation of Galaxies and Clusters of Galaxies by Self-Similar Gravitational Condensation. *Astrophys. J.*, **187**, 425 (1974)

Primack, J. R. and Gross, M. A. K. Hot dark matter in cosmology. In *Current aspects of neutrino physics*, page 287 (2001)

Reines, F. and Cowan, C. L. Detection of the Free Neutrino . *Physical Review*, **92**, 830 (1953)

Ryden, B. S. and Gunn, J. E. Galaxy formation by gravitational collapse. *Astrophys. J.*, **318**, 15 (1987)

Sakamoto, T., Chiba, M., and Beers, T. C. The mass of the Milky Way: Limits from a newly assembled set of halo objects. *Astr. & Astrophys.*, **397**, 899 (2003)

Shibata, M. and Uryū, K. Gravitational Waves from Merger of Binary Neutron Stars in Fully General Relativistic Simulation. *Progress of Theoretical Physics*, **107**, 265 (2002)

Sikivie, P. Experimental tests of the 'invisible' axion. *Physical Review Letters*, **51**, 1415 (1983)

Somerville, R. S. and Kolatt, T. S. How to plant a merger tree. *Mon. Not. R. Astr. Soc.*, **305**, 1 (1999)

Spergel, D. N., et al. First Year Wilkinson Microwave Anisotropy Probe (WMAP) Observations: Determination of Cosmological Parameters. *ArXiv Astrophysics e-prints* (2003). `astro-ph/0302209`

Stiff, D. and Widrow, L. M. Fine Structure of Dark Matter Halos and its Effect on Terrestrial Detection Experiments. *Physical Review Letters*, **90**, 211301 (2003)

Stiff, D., Widrow, L. M., and Frieman, J. Signatures of hierarchical clustering in dark matter detection experiments. *Phys. Rev. D*, **64**, 083516 (2001)

Stompor, R., et al. Cosmological Implications of the MAXIMA-1 High-Resolution Cosmic Microwave Background Anisotropy Measurement. *Astrophys. J. Lett.*, **561**, L7 (2001)

Theis, C. Two-body relaxation in softened potentials. *Astr. & Astrophys.*, **330**, 1180 (1998)

Toshito, T. and The Super-Kamiokande Collaboration. Super-Kamiokande atmospheric neutrino results. *ArXiv Astrophysics e-prints* (2001). `hep-ex/0105023`

Toth, G. and Ostriker, J. P. Galactic disks, infall, and the global value of Omega. *Astrophys. J.*, **389**, 5 (1992)

Turner, M. S. Cosmic and local mass density of "invisible" axions. *Phys. Rev. D*, **33**, 889 (1986)

Unavane, M., Wyse, R. F. G., and Gilmore, G. The merging history of the Milky Way. *Mon. Not. R. Astr. Soc.*, **278**, 727 (1996)

Verde, L., et al. The 2dF Galaxy Redshift Survey: the bias of galaxies and the density of the Universe. *Mon. Not. R. Astr. Soc.*, **335**, 432 (2002)

White, M., Scott, D., and Silk, J. Anisotropies in the Cosmic Microwave Background. *Ann. Rev. Astr. & Astrophys.*, **32**, 319 (1994)

Widrow, L. M. Distribution Functions for Cuspy Dark Matter Density Profiles. *Astrophys. J. Supp.*, **131**, 39 (2000)

Wilkinson, M. I. and Evans, N. W. The present and future mass of the Milky Way halo. *Mon. Not. R. Astr. Soc.*, **310**, 645 (1999)

Wozniak, P. R. Difference Image Analysis of the OGLE-II Bulge Data. I. The Method. *Acta Astronomica*, **50**, 421 (2000)

Yo, H., Baumgarte, T. W., and Shapiro, S. L. Improved numerical stability of stationary black hole evolution calculations. *Phys. Rev. D*, **66**, 84026 (2002)

Zaldarriaga, M. and Seljak, U. CMBFAST for Spatially Closed Universes. *Astrophys. J. Supp.*, **129**, 431 (2000)

Zaroubi, S. Unbiased reconstruction of the large-scale structure. *Mon. Not. R. Astr. Soc.*, **331**, 901 (2002)

Zel'Dovich, Y. B. Gravitational instability: an approximate theory for large density perturbations. *Astr. & Astrophys.*, **5**, 84 (1970)

Zhao, H. Analytical dynamical models for double power-law galactic nuclei. *Mon. Not. R. Astr. Soc.*, **287**, 525 (1997)

Zioutas, K., et al. A decommissioned LHC model magnet as an axion telescope. *Nuclear Instruments and Methods in Physics Research A*, **425**, 480 (1999)

Zwicky, F. *Helv. Phys. Acta.*, **6**, 217 (1933)

A. COSMOLOGY

A.1 General Relativity

A complete introduction to general relativity is beyond the scope of this Appendix. However, for the purposes here, it is sufficient to say that the geometry of space-time, described by the metric

$$ds^2 = g_{\alpha\beta} dx^\alpha dx^\beta \tag{A.1}$$

is governed by the mass and energy distribution, T^β_α. They are related through Einstein's equation:

$$G^\beta_\alpha = \frac{8\pi G}{c^4} T^\beta_\alpha \tag{A.2}$$

where $G^\beta_\alpha = R^\beta_\alpha - 1/2 g^\beta_\alpha R$, R^β_α is the Ricci tensor and R is the Ricci scalar. Both R^β_α and R are related to the metric elements $g_{\alpha\beta}$.

A.2 Robertson-Walker Metric

According to the cosmological principle, the Earth should occupy no special spot in the universe. Since on sufficiently large scales, the universe appears homogeneous to terrestrial observers, it should appear the same to any other observer located elsewhere. This leads to the conclusion that the universe must be isotropic and homogenous. The only metric which satisfies both isotropy and homogeneity is the Robertson-Walker metric:

$$ds^2 = a(t)^2 \left[\frac{dr^2}{1 + r^2/R^2} + r^2(d\theta^2 + \sin^2\theta d\phi^2) \right] - c^2 dt^2 \tag{A.3}$$

where R is the radius of curvature. If R is real, the spacetime has negative curvature; if R is imaginary, the spacetime has a positive curvature. $R = \infty$ is flat space. Calculating the Einstein tensor[1] yields

$$G_r^r = -\frac{\dot{a}^2 + 2a\ddot{a} - c^2R^{-2}}{c^2a^2} \tag{A.4}$$

$$G_\theta^\theta = -\frac{\dot{a}^2 + 2a\ddot{a} - c^2R^{-2}}{c^2a^2} \tag{A.5}$$

$$G_\phi^\phi = -\frac{\dot{a}^2 + 2a\ddot{a} - c^2R^{-2}}{c^2a^2} \tag{A.6}$$

$$G_t^t = -3\frac{\dot{a}^2 - c^2R^{-2}}{c^2a^2} \tag{A.7}$$

The remaining terms are zero. For a perfect fluid with a cosmological constant the stress-energy tensor is

$$T_r^r = T_\theta^\theta = T_\phi^\phi = p - \frac{c^2}{8\pi G}\Lambda \tag{A.8}$$

$$T_t^t = -\rho c^2 - \frac{c^2}{8\pi G}\Lambda \tag{A.9}$$

with the remaining terms zero where p is the pressure, ρ is the density, and Λ is the cosmological constant. Therefore, from (A.2)

$$\frac{\dot{a}^2 + 2a\ddot{a} - c^2R^{-2}}{a^2} = -\frac{8\pi Gp}{c^2} + \Lambda \tag{A.10}$$

and

$$3\frac{\dot{a}^2 - c^2R^{-2}}{a^2} = 8\pi G\rho + \Lambda \tag{A.11}$$

Equations (A.10) and (A.11) are the Friedmann equations. Rearranging them into the more familiar form yields

$$\frac{\dot{a}}{a} = \left[\frac{8\pi G\rho}{3} + \frac{\Lambda}{3} + \frac{c^2}{R^2a^2}\right]^{1/2} \tag{A.12}$$

$$\frac{\ddot{a}}{a} = -\frac{4\pi G}{3}\left(\rho + 3\frac{p}{c^2}\right) + \frac{\Lambda}{3} \tag{A.13}$$

Several additional parameters are useful. The Hubble parameter,

$$H = \frac{\dot{a}}{a} \tag{A.14}$$

[1] GRTensorJ (http://grtensor.phy.queensu.ca) was used to perform the metric calcuations.

the redshift,

$$1 + z = \frac{a_0}{a(t)} \tag{A.15}$$

where the subscript 0 is used to indicate the present-day value of a parameter, and the deceleration parameter,

$$q = -\frac{\ddot{a}a}{\dot{a}^2} \tag{A.16}$$

Under the assumption that the pressure term, p, can be neglected (a good approximation when collisionless dark matter dominates the mass of the Universe), equations (A.12) and (A.13) can be reduced to

$$\frac{\dot{a}}{a} = H_0 \left[\frac{\Omega_M}{(a/a_0)^3} + \frac{\Omega_R}{(a/a_0)^2} + \Omega_\Lambda \right]^{1/2} \tag{A.17}$$

$$\frac{\ddot{a}a}{\dot{a}^2} = -\frac{H_0^2}{H^2} \left[\frac{\Omega_M}{2(a/a_0)^3} - \Omega_\Lambda \right] \tag{A.18}$$

where

$$\Omega_M = \frac{8\pi G\rho_0}{3H_0^2}, \quad \Omega_\Lambda = \frac{\Lambda}{3H_0^2}, \quad \Omega_R = \frac{c^2}{H_0^2 R^2 a_0^2} \tag{A.19}$$

Evaluating these expressions at the present day yields

$$\Omega_M + \Omega_\Lambda + \Omega_R = 1 \tag{A.20}$$

and

$$q_0 = \frac{\Omega_M}{2} - \Omega_\Lambda \tag{A.21}$$

A.3 Selected Solutions to the Friedmann Equations

A completely general solution to equations (A.12) and (A.13) is difficult to obtain. However, it is useful to examine various popular sets of parameters in order to understand how the universe evolves in likely cases.

A.3.1 $\Omega_m = 1, \Omega_\Lambda = 0, \Omega_R = 0$

The simplest solution for Friedmann's equations, known as a Einstein-DeSitter model, is for $\Omega_m = 1, \Omega_\Lambda = 0$, and $\Omega_R = 0$. This is a flat, matter-dominated

universe with no cosmological constant. In this case the solution is

$$a(t) = \left(\frac{3H_0}{2}t\right)^{2/3} \tag{A.22}$$

normalized such that at the present time, t_0, $a(t_0) = 1$. The age of the Universe, parameterized by the present value of the Hubble constant, is then

$$H_0 t_0 = \frac{2}{3} \tag{A.23}$$

A.3.2 $\Omega_m + \Omega_\Lambda = 1, \Omega_R = 0$

This case is motivated by the current observational constraints that indicate $\Omega_m \approx 0.27$ and $\Omega_\Lambda \approx 0.73$ (Spergel et al., 2003). In this case, the general solution to (A.12) and (A.13) has the form

$$a(t) = C \sinh^{2/3}(\alpha t) \tag{A.24}$$

where C and α are constants to be determined by substituting the general form into the Friedmann equations and requiring that $a(t_0) = 1$. Solving yields

$$C = \left(\frac{\Omega_M}{\Omega_\Lambda}\right)^{1/3}, \text{ and } \alpha = \frac{3}{2}H_0\sqrt{\Omega_\Lambda} \tag{A.25}$$

Therefore,

$$a(t) = \left(\frac{\Omega_M}{\Omega_\Lambda}\right)^{1/3} \sinh^{2/3}\left(\frac{3}{2}H_0\sqrt{\Omega_\Lambda}\, t\right) \tag{A.26}$$

In this case, the age of the Universe is

$$H_0 t_0 = \frac{2}{3}\frac{1}{\sqrt{\Omega_\Lambda}} \ln\left[\sqrt{\left(\frac{\Omega_\Lambda}{\Omega_M}\right)} + \sqrt{\left(\frac{\Omega_\Lambda}{\Omega_M}\right) + 1}\right] \tag{A.27}$$

Using $\Omega_\Lambda = 0.73$ and $\Omega_M = 0.27$ yields $H_0 t_0 \approx 1.04$ or roughly 1.5 times the age of the Einstein-DeSitter Universe. Note that it was assumed that $\Omega_\Lambda > 0$ to be consistent with observations.

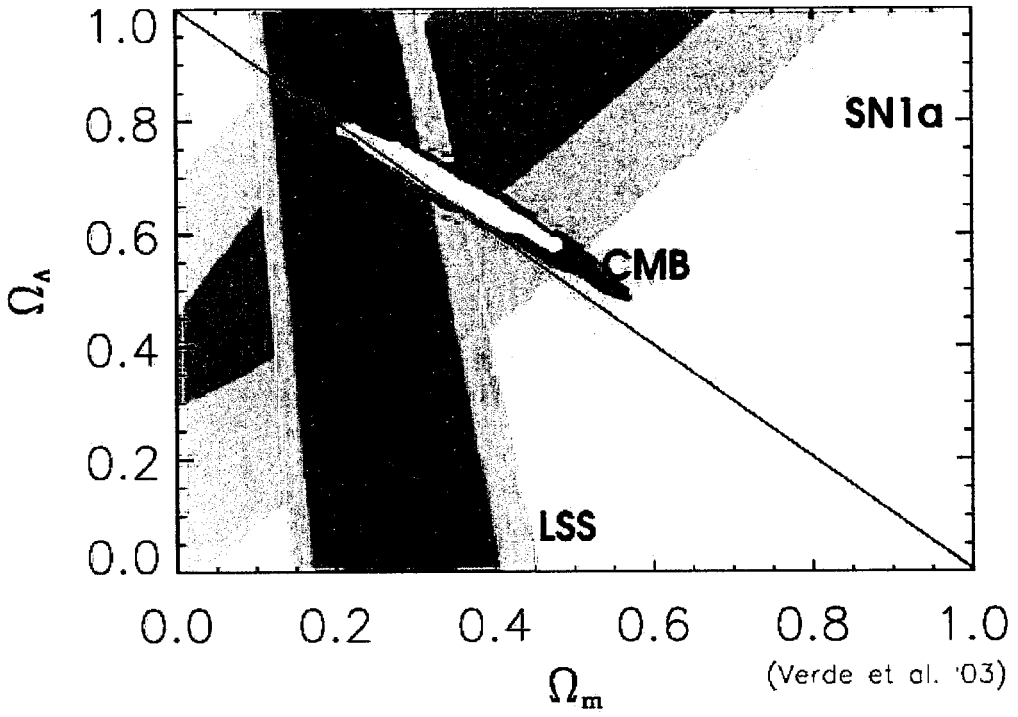

Figure A.1: Contraints on cosmological paramters from the cosmic microwave background (CMB) (Spergel et al., 2003), large scale structure surveys (LSS) (Verde et al., 2002) and supernova results (SN1a) (Perlmutter et al., 1999). Figure is an updated version of one from Verde et al. (2002) available at http://www.astro.princeton.edu/~lverde/

B. STRUCTURE FORMATION

B.1 The Evolution of Structure

In the early universe, matter can be modelled as a gravitating perfect fluid. When small perturbations are present in the fluid, they can grow under the influence of gravity. If the perturbations are sufficiently small, their evolution can be approximated through linear approximations.

B.1.1 Perfect Fluid

The standard fluid dynamic equations in a gravitating system are

$$\left(\frac{\partial \rho}{\partial t}\right)_{\vec{r}} + \nabla_{\vec{r}} \cdot \rho \vec{u} = 0, \tag{B.1}$$

$$\rho \left[\left(\frac{d\vec{u}}{dt}\right)_{\vec{r}} + (\vec{u} \cdot \nabla_{\vec{r}})\vec{u} \right] = -\nabla_{\vec{r}} p - \rho \nabla_{\vec{r}} \Phi \tag{B.2}$$

$$\nabla^2 \Phi = 4\pi G \rho \tag{B.3}$$

where $\vec{r}$ and $\vec{u}$ are the proper distance and velocity of a fluid element relative to a fixed origin. If the fluid is expanding, these can be related to comoving coordinates, $\vec{x}$ and $\vec{v}$ by

$$\vec{x} = \frac{\vec{r}}{a(t)} \tag{B.4}$$

$$\vec{v} = \vec{u} - \frac{\dot{a}}{a}\vec{r} \tag{B.5}$$

The fluid equations in expanding coordinates are then

$$\frac{\partial \rho}{\partial t} + 3\frac{\dot{a}}{a}\rho + \frac{1}{a}\nabla \cdot \rho \vec{v} = 0 \tag{B.6}$$

$$\frac{\partial \vec{v}}{\partial t} + \frac{1}{a}(\vec{v}\cdot\nabla)\vec{v} + \frac{\dot{a}}{a}\vec{v} = -\frac{1}{\rho a}\nabla p - \frac{1}{a}\nabla\phi \tag{B.7}$$

where the comoving potential, ϕ, is related to the fixed potential Φ via $\Phi = \phi - 1/2\,a\ddot{a}x^2$. Finally, it is useful to express the continuity equation (B.6) in terms of the density contrast δ defined by

$$\rho(\vec{x},t) \equiv \frac{\rho_0}{a^3}(1+\delta(\vec{x},t)) \tag{B.8}$$

where ρ_0 is the present-day mean density. Substituting (B.8) into (B.6) yields

$$\frac{\partial \delta}{\partial t} + \frac{1}{a}\nabla\cdot(1+\delta)\vec{v} = 0 \tag{B.9}$$

The above expressions can be combined to yield (Peebles, 1980):

$$\frac{\partial^2\delta}{\partial t^2} + 2\frac{\dot{a}}{a}\frac{\partial\delta}{\partial t} = \frac{a}{\rho_0}\nabla^2 p + \frac{1}{a^2}\nabla\cdot(1+\delta)\nabla\phi + \frac{1}{a^2}\frac{\partial^2}{\partial x^\alpha \partial x^\beta}[(1+\delta)v^\alpha v^\beta] \tag{B.10}$$

While equation (B.10) completely describes the growth the the density perturbations, it is very difficult to handle directly. However, if the density contrasts are small ($\delta \ll 1$) and the velocity distribution has no skewness (last term in (B.10) is ≈ 0) it is possible to linearize the expression.

$$\frac{\partial^2\delta}{\partial t^2} + 2\frac{\dot{a}}{a}\frac{\partial\delta}{\partial t} = \frac{4\pi G\rho_0}{a^3}\delta \tag{B.11}$$

From Peebles (1980) the solution to (B.11) is

$$\delta_1(\vec{x},t) = \frac{\dot{a}}{a}\int_0^t \frac{dt}{\dot{a}^2}\,\delta(\vec{x},t_0), \quad \delta_2(\vec{x},t) = \frac{\dot{a}}{a}\,\delta(\vec{x},t_0) \tag{B.12}$$

These solutions describe the growth of pertubations in a homogenous, isotropic universe when the matter is modelled by a pressureless, perfect fluid. Note that δ_1 corresponds to a growing mode, while δ_2 is a decaying mode.

B.1.2 $\Omega_m = 1, \Omega_\Lambda = 0, \Omega_R = 0$

For a flat, matter-dominated universe, the solution to (B.12) is

$$\delta_1(t) = \frac{2}{5}\frac{1}{H_0^2}a(t), \quad \delta_2(t) = H_0\,a^{-3/2}(t) \tag{B.13}$$

or, expressed in terms of redshift z,

$$\delta_1(z) = \frac{2}{5}\frac{1}{H_0^2}\frac{1}{1+z}, \quad \delta_2(z) = H_0\,(1+z)^{3/2} \tag{B.14}$$

and

$$\dot{\delta_1}(z) = \frac{2}{5}\frac{1}{H_0}\sqrt{1+z}, \quad \dot{\delta_2}(z) = -\frac{3}{2}H_0^2\,(1+z)^3 \tag{B.15}$$

B.1.3 $\Omega_m + \Omega_\Lambda = 1, \Omega_R = 0$

The solution to (B.12) is

$$\delta_1(t) = \frac{2}{3H_0^2\Omega_M}\coth\left(\frac{3}{2}H_0\sqrt{\Omega_\Lambda}\,t\right)\int_0^{3H_0\sqrt{\Omega_\Lambda}t/2}\frac{\sinh^{2/3}(x)}{\cosh^2(x)}dx \tag{B.16}$$

$$\delta_2(t) = H_0\sqrt{\Omega_\Lambda}\coth\left(\frac{3}{2}H_0\sqrt{\Omega_\Lambda}\,t\right) \tag{B.17}$$

This has been expressed more conveniently by Bildhauer et al. (1992) in terms of $a(t)$:

$$\delta_1 = \frac{5}{6}B_x(5/6, 2/3)\left(\frac{\Omega_m}{\Omega_\Lambda}\right)^{1/3}x^{-1/2} \tag{B.18}$$

$$\delta_2 = a^{-3/2}\sqrt{1+\frac{1-\Omega_m}{\Omega_m}a^3} \tag{B.19}$$

where

$$x^{-1} = 1 + \frac{\Omega_m}{1-\Omega_m}a^{-3} \tag{B.20}$$

and $B_x(a,b)$ is the incomplete beta function.

Note that the normalization of the two forms of the solution are different. However, since it is generally the ratio of the expansion factors at two times that is of interest, the absolute normalization is not important.

B.2 Zel'Dovich Approximation

Zel'Dovich (1970) proposed that the evolution of particles in the early universe could be modelled in comoving coordinates via the simple construct of:

$$\vec{x}(t) = \vec{q} + B(t)\vec{f}(\vec{q}) \tag{B.21}$$

where $\vec{q}$ is the initial position of the particle, $\vec{f}(\vec{q})$ is an unknown perturbation function and, $B(t)$ is some unknown growing term.

From the conservation of mass one finds that

$$\int \rho(\vec{x},t)d^3x = \int \bar{\rho}_0 d^3q \tag{B.22}$$

Therefore,

$$\rho(\vec{x},t) = \bar{\rho}_0 \left|\frac{\partial \vec{q}}{\partial \vec{x}}\right| \tag{B.23}$$

$$= \bar{\rho}(t)\left|\delta_{ij} + B(t)\frac{\partial f_j}{\partial q_i}\right|^{-1} \tag{B.24}$$

Expanding linearly in $B(t)\vec{f}(\vec{q})$ gives

$$\delta_{\text{zeldovich}} = \frac{\rho - \bar{\rho}_0}{\bar{\rho}_0} = -B(t)\vec{\nabla}_q \cdot \vec{f}(\vec{q}) \tag{B.25}$$

From linear thoery, one expects the growing modes to be given by (B.12)

$$\delta_{\text{linear}}(\vec{x},t) = \frac{\dot{a}}{a}\int_0^t \frac{dt}{\dot{a}^2}\,\delta(\vec{r},t_0) \tag{B.26}$$

$$= \delta_1(t)\sum_k \delta_k e^{i\vec{k}\cdot\vec{r}} \tag{B.27}$$

$$= \delta_1(t)\sum_k \delta_k e^{i\vec{k}\cdot[\vec{q}+B(t)\vec{f}(\vec{q})]} \tag{B.28}$$

where the Fourier expansion of $\delta(\vec{r},t_0)$ was used. However, since the Zeldovich perturbations are small, initially $B(t)\vec{f}(\vec{q}) \ll \vec{q}$. Therefore,

$$\delta_{\text{linear}} \approx \delta_1(t)\sum_k \delta_k e^{i\vec{k}\cdot\vec{q}} \tag{B.29}$$

In order for equations (B.25) and (B.29) to be consistent, it is required that $B(t) = \delta_1(t)$ and

$$\vec{f}(\vec{q}) = \sum_k \frac{i\vec{k}}{k^2}\delta_k e^{i\vec{k}\cdot\vec{q}} \tag{B.30}$$

The Zel'Dovich approximation has the advantage over standard linear theory in that it remains qualitatively correct even when the perturbations become large and the linear theory approximations can no longer be applied (Zel'Dovich, 1970). This

allows one to analytically follow the evolution of small perturbations much farther than one might expect. For numerical simulations, the ability to model the early stages of growth beyond the truly linear regime is of great benefit since it permits one to start the simulation at a much later time and reduce the total amount of computation.

B.2.1 Numerical Initial Conditions

To apply the Zel'Dovich approximation to numerical initial conditions, one must determine values for δ_k appropriate for the chosen power spectrum $P(k)$.

$$P(k) =< \delta_k >^2 \tag{B.31}$$

In general, δ_k could be a complex value. However, if one assumes that the initial density fluctuations are Gaussian, δ_k can be chosen by simply choosing δ_R (real part of δ_k) and δ_I (imaginary part of δ_k) from a Gaussian distribution with variance given by $P(k)$. The initial particles can then be perturbed according to:

$$\vec{x}_p(\vec{x_0}, t) = \vec{x}_0 + \delta_1(t) \sum_k \frac{\vec{k}}{k^2} \left(\delta_I \cos \vec{k} \cdot \vec{x}_0 + \delta_R \sin \vec{k} \cdot \vec{x}_0 \right) \tag{B.32}$$

where $\vec{x}_0$ is the particle's initial unperturbed position.

For the reverse-run technique, it is necessary to undo these perturbations. Unfortunately, equation (B.32) is not analytically invertible. However, the initial point, $\vec{x}_0$ which yields the perturbed point,$\vec{P}$, can be found by numerically solving for the roots of

$$\begin{aligned} \Delta_i &= P_i - x_{p_i}(\vec{x}) \\ &= P_i - x_i - \delta_1(t) \sum_k \frac{k_i}{k^2} \left(\delta_I \cos \vec{k} \cdot \vec{x} + \delta_R \sin \vec{k} \cdot \vec{x} \right) \end{aligned} \tag{B.33}$$

This is a set of three coupled equations which cannot be separated. However, a simple and efficient technique to find the roots is Newton's method. The basic idea

behind the algorithm is that if the value of a function and its derivative are known at a given point, it can be used to extrapolate an estimate for the x-intercept.

$$x_o = x - \frac{f(x)}{f'(x)} \tag{B.34}$$

The derivative of the function can then be calculated at this new point, x_o, and the procedure repeated until the root is found.

To apply this technique to undoing the Zel'Dovich perturbations requires the derivatives of Δ:

$$\frac{\partial \Delta_i}{\partial x_i} = -1 + \delta_1(t) \sum_k \frac{k_i^2}{k^2} \left(\delta_I \sin \vec{k} \cdot \vec{x} - \delta_R \cos \vec{k} \cdot \vec{x} \right) \tag{B.35}$$

Each new approximation for the initial position, $\vec{x}_0$, which yields the perturbed position, $\vec{P}$, is

$$x_i' = x_i - \frac{P_i - x_i - \delta_1(t) \sum_k \frac{k_i}{k^2} \left(\delta_I \cos \vec{k} \cdot \vec{x} + \delta_R \sin \vec{k} \cdot \vec{x} \right)}{-1 + \delta_1(t) \sum_k \frac{k_i^2}{k^2} \left(\delta_I \sin \vec{k} \cdot \vec{x} - \delta_R \cos \vec{k} \cdot \vec{x} \right)} \tag{B.36}$$

Since the Zel'Dovich perturbations are relatively small, an initial guess of $\vec{x} = \vec{P}$ is a good starting point.

Note that this is not a strictly complete implementation of Newton's method in three dimensions since the terms $\partial \Delta_i / \partial x_j$ where $i \neq j$ are ignored. Nonetheless, since the perturbations are small, the algorithm still converges quickly.

- Stiff, D.,Widrow, L. M., Frieman, J., *Dark Matter Detection in a Hierarchically Forming Halo*, 3rd International Workshop on the Identification of Dark Matter Conference Proceeding (2000)

Meetings and Presentations

- Stiff, D.,Widrow, L. M., *Dark Matter Detection in a Hierarchically Forming Halo*, Canadian Astronomical Society Annual General Meeting, May 2001 (Poster)
- Stiff, D.,Widrow, L. M., Frieman, J., *Dark Matter Detection in a Hierarchically Forming Halo*, 3rd International Workshop on the Identification of Dark Matter, Sep 18 - 23, 2000 (Oral Presentation)
- Stiff, D., Widrow, L. M., Frieman, J., *WIMP Detection in a Clumpy Halo*, Victoria Computational Cosmology Conference, Aug 21 - 25, 2000 (Poster)
- Stiff, D., Widrow, L. M., Frieman, J., *Probing the Local WIMP Density*, American Astronomical Society Meeting #196, June 4 - 8, 2000 (Poster)

Awards and Honours

2001 - 2003 NSERC Postgraduate Scholarship (PGS B), Queen's University

2002 Queen's Graduate Award

2001 Carl Reinhardt Fellowship

1998 - 2000 NSERC Postgraduate Scholarship (PGS A), Queen's University

2000 Ontario Graduate Scholarship, Queen's University

2000 Queen's Graduate Award, Queen's University

1999 Queen's Graduate Award, Queen's University

1998 University Prize for Special Achievement, McMaster University

1997 Summer Research Fellowship, McMaster University

1995, 1996, 1997 Senate Award, McMaster University

1995 Hamilton Institute Engineering Prize, McMaster University

1994 Dofasco Entrance Scholarship, McMaster University

1994 Canada Scholarship, McMaster University

1994 Governor-General Bronze Medal, Eastview Secondary School